

Kinetic Modeling in Positron Emission Tomography

EVAN D. MORRIS,* CHRISTOPHER J. ENDRES,† KATHLEEN C. SCHMIDT,‡ BRADLEY T. CHRISTIAN,§
RAYMOND F. MUZIC JR.,¶ RONALD E. FISHER||

*Departments of Radiology and Biomedical Engineering, Indiana University School of Medicine, Indianapolis, Indiana

†Department of Radiology, Johns Hopkins University, Baltimore, Maryland

‡Laboratory of Cerebral Metabolism, NIMH, Bethesda, Maryland

§Wright State University, Kettering Medical Center, Dayton, Ohio

¶Departments of Radiology, Oncology and Biomedical Engineering, Case Western Reserve University, Nuclear Medicine, University Hospitals Cleveland, Cleveland, Ohio

||The Methodist Hospital and Department of Radiology and Neuroscience, Baylor College of Medicine, Houston, Texas

- I. Introduction
- II. The One-Compartment Model: Blood Flow
- III. Positron Emission Tomography Measurements of Regional Cerebral Glucose Use
- IV. Receptor-Ligand Models
- V. Model Simplifications
- VI. Limitations to Absolute Quantification
- VII. Functional Imaging of Neurochemistry—Future Uses
- VIII. A Generalized Implementation of the Model
- Equations

I. INTRODUCTION

Positron emission tomography (PET) is a functional imaging technique that measures the local concentration of an exogenous tracer molecule in the target tissue. Thus, given a time sequence of PET images, one can quantify tracer kinetics *in vivo*. The power of PET lies in its molecular specificity. By using a particular radiotracer molecule, one can monitor the interaction of that molecule with the body's physiological processes. For example, blood flow can be measured by using radioactive water as a tracer; metabolism can be measured with radioactive glucose (FDG).

In this chapter we examine mathematical kinetic models used to analyze time sequences of PET images to gather quantitative information about the body. We include methods

used in the two most ubiquitous applications of PET: imaging of blood flow and glucose metabolism. We also examine the use of PET to image specific receptor molecules, which capitalizes on the unique specificity of PET.

Supplied with single (static) PET images and no kinetic model to aid in their interpretation, one is confined to asking questions that can be answered only on the basis of spatial information such as: Where is glucose being used? Where are particular receptor molecules located within the brain or the heart?

With the acquisition of dynamic (time-sequence) imaging data and the application of kinetic models, one can pose many additional quantitative questions based on temporal information such as: How many receptors are there in a volume of tissue? What is the rate of trapping or the rate of influx of a tracer to the tissue? More recently, PET researchers have also begun asking questions about changes in particular parameters such as: When an endogenous ligand is perturbed, how does its level change? In this application, the radiotracer is used to infer information about an endogenous molecule that is not radioactive, exploiting the predictable nature of the competition between endogenous and exogenous ligands for specific binding sites.

Creative users of PET have also begun to ask questions about gene transcription. By linking a molecule that can be imaged to a therapeutic gene, one may be able to monitor the transcription of therapeutic genes with PET. The models for this application have not been worked out at this writing;

however we speculate in this chapter about the modeling issues that will arise if the application of PET imaging to gene therapy monitoring is to succeed as a quantitative tool.

All these applications can benefit from analysis based on modeling; but they require that the modeler understand how the data are generated and what the inherent inaccuracies in the data are.

Why do we need a model? In PET, the images are a composite of various superimposed signals, only one of which is of interest. The desired signal may describe, for example, the amount of tracer trapped at the site of metabolism or tracer bound to a particular receptor. In order to isolate the desired component of the signal (think of an image composed of layers), we must use a mathematical model relating the dynamics of the tracer molecule and all its possible states to the resultant PET image. Each of these states is known in the language of kinetic modeling as a *compartment*. For example, in a receptor-imaging study, the set of molecules that are bound to the target receptor can constitute one compartment. Each compartment is characterized by the concentration of the tracer within it as a function of time. These concentrations are related through sets of ordinary differential equations, which express the balance between the mass entering and exiting each compartment. By solving these simultaneous equations, we are able to determine the quantities of interest.

Kinetic models for PET typically derive from the one-, two-, or three-compartment model in which a directly measured blood curve (concentration of radiotracer in the blood as a function of time) serves as the model's input function.¹ The coefficients of the differential equations in the model are taken to be constants that are reflective of inherent kinetic properties of the particular tracer molecule in the system. By formally comparing the output of the model to the experimentally obtained PET data, one can estimate values for these kinetic parameters and thus extract information about binding, delivery, or any hypothesized process, as distinct from all other processes contributing to the PET signal.

In general, the information content of the PET data is inadequate to support models of great sophistication, and so adoption of a particular model is by necessity a great simplification of the truth. The interpretation of parameters comes with associated assumptions and conditions that must be satisfied and periodically revisited. Sometimes the overriding limitations are experimental. The most common such limitation is the inconvenience of, or outright prohibition against, obtaining direct measurement of the plasma input function (or input function). This limitation has of necessity given rise to a whole class of model simplifications, which are developed and examined in this chapter. Other experimental consid-

erations are discussed with regard to possible future clinical and research uses of PET ligand studies. Finally, we conclude our treatment of PET kinetic modeling with a discussion of a generalized framework for the implementation and solution of the differential equations that constitute these models.

A. What's in a Compartment?

Compartmental modeling is used to describe systems that vary in time but not in space. Thus, one of the first assumptions of compartmental modeling is called the well-mixed assumption. We assume that there are no spatial concentration gradients (only gradients in time) within the area being sampled (e.g., a voxel in the case of a 3D image volume.) Within a voxel, we assume that whatever radioactive species contribute to the emanating radioactive signal are in uniform concentration and can be characterized as being in unique states. Each of these states is assigned a compartment, which in turn is described by a single ordinary differential equation.

Any system requires an input to drive it. We typically consider the input to the system to be the measured radioactivity concentration in the blood supply as a function of time. Although the blood supply is a compartment in the physical sense, it is not a compartment of the model in the mathematical sense because it is measured rather than solved for. However, the input concentration is often depicted as a box in graphical representations of kinetic models. We will adhere to this custom, but the reader should be aware that it is not strictly correct.

Compartmental models often arise in the course of describing the kinetics of a tracer injected into a physiological system. In tracer studies, we make certain assumptions about the behavior of the tracer molecule, often radioactive, but sometimes labeled with a fluorochrome or other detectable marker. The key assumptions that must be satisfied are as follows.

1. The amount of tracer injected is a trace amount; that is, it causes no change in the physiology of the organism. For example, tracers are often drugs, but when injected as tracers they must cause no drug effects. We sometimes violate this assumption when giving low-specific-activity (near-saturation) doses of a radioligand in PET.
2. The tracer is in steady state with the endogenous molecule that the tracer seeks to emulate (which we call the *tracee*). That is, the tracer goes everywhere that the tracee goes. In PET, we often talk about freely diffusible tracers, which are tracers that easily cross into and out of the vasculature. Note that the tracee (e.g., glucose in the brain) can itself be in a non-steady-state condition with respect to the system if we perturb it, but the relationship between the tracer and tracee should be fixed.
3. There are no isotope effects. That is, the act of labeling the tracer molecule with a radionuclide does not alter its properties.

¹There are modifications of the model (i.e., reference region models) that do not use an independently measured blood curve as input. These models are addressed later in this chapter.

There are a few additional assumptions to keep in mind. Usually, one assumes that the parameters of our model are time-invariant, at least over the duration of our study. One can consider the kinetic parameters to be a reflection of the steady state of the system and the innate properties of the ligand. The kinetic parameters that one estimates from a PET study provide a snapshot of the average state of the system and the ligand at a given time or over a short time period (i.e., the length of a study). To solve our differential equations one needs an input function, which drives the model, and initial conditions, which are usually zero because there is usually no radioactivity in the system before a tracer experiment begins. This might not be the case if one were to do multiple repeated studies, one right after the other. As a practical matter, in PET one typically assumes that all tissues of the body see the same input function, which is assumed to be the measured radioactivity in the blood plasma during the experiment. With zero initial conditions and without an input function, the concentration of tracer in the compartments of the model would remain at zero indefinitely.

B. Constructing a Compartmental Model

Compartmental models are used to describe the dynamics of PET measurements. The data are generally not of sufficient spatial resolution to support more-complicated mathematical descriptions that include spatial gradients (i.e., distributed models). Nevertheless, compartmental models have good predictive power so we continue to use them. How do we get from a complex physiological system to a highly simplified compartmental model?

Consider PET images of the brain (see Figure 1a), which are the primary source of data discussed in this chapter. Referring to a sample (in our case, a voxel), consider the primary states that a radioactive tracer molecule (blue diamonds on Figure 1b) can assume. First, the tracer in the brain might be in the blood. After all, that is how it is delivered to the brain. If it is freely diffusible, some tracer will eventually be in the extravascular state. If there are receptors in the brain specific for our tracer, some tracer may become bound to these receptors, at which time we consider it to be in the bound state. We use the term *state* because these

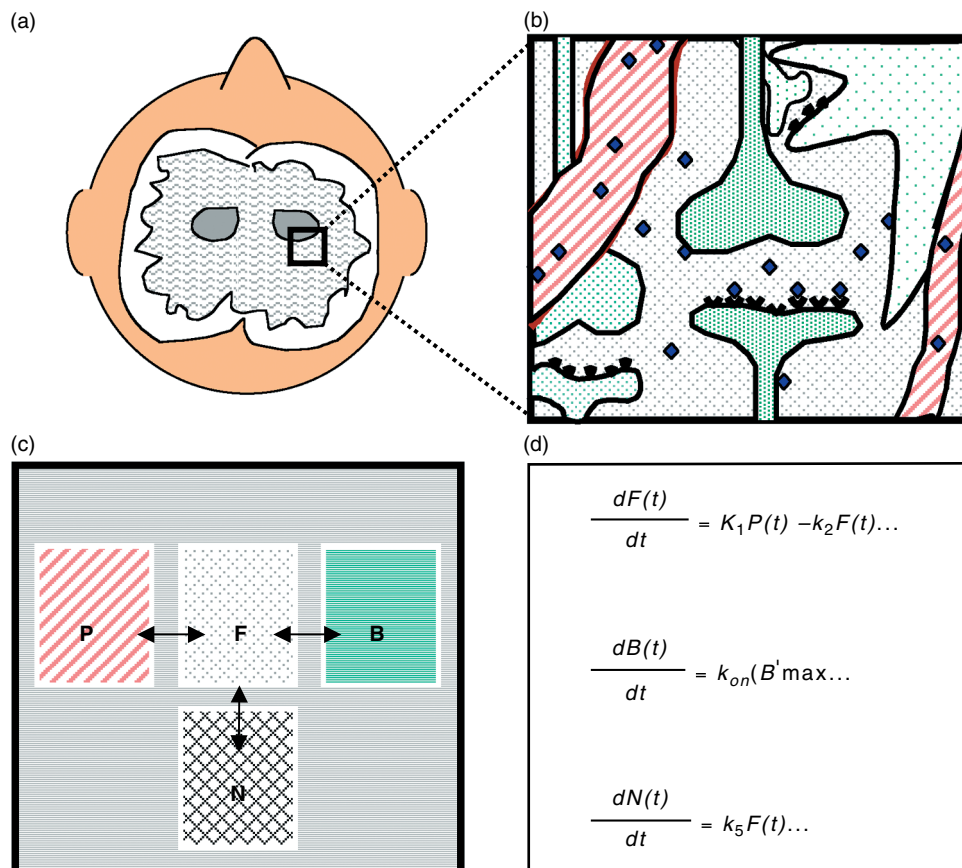


FIGURE 1 Schematic of the compartmental modeling process as applied to PET images. Steps: (a) identify a region of interest in an image, (b) conceptualize the contents of the region and the possible states of the tracer in the region, (c) further abstract the ligand states to compartments with a particular topology or connectedness, and (d) write the mass balances on each of the unknown compartments as ordinary differential equations.

compartments do not necessarily occupy distinct locations on the macroscopic scale. Figure 1b is our conception of the major possible states of the tracer molecule. In Figure 1c, we indicate a further abstraction of the schematic in Fig. 1b by identifying what we believe to be the primary states of the molecule and the connections between them.

Once the connections or paths that the tracer can take between compartments have been specified, the mass balances on each compartment can be written in the form of ordinary differential equations. One differential equation must be specified for each unknown quantity. If the concentration of tracer in the plasma is known, it is not a compartment but its (time-varying) concentration does factor into the mass balances of the compartments. The differential equations of the model (Figure 1d) are written to describe influx to, and efflux from, each compartment. They are functions of the rate constants for these processes and, in the case of saturable processes, the derivatives will also be a function of the number of available binding sites.

For more detailed treatments of compartmental modeling in physiology and in PET specifically, please consult E. Carson *et al.* (1983), Jacquez (1985), Berman *et al.* (1982), R. Carson (1996), and Huang and Phelps (1986).

We begin our discussion of specific models with an examination of the simplest model used in PET, the blood flow model, which is described by only one compartment.

II. THE ONE-COMPARTMENT MODEL: BLOOD FLOW

A. One-Tissue Compartmental Model

A simple compartmental model that frequently arises in PET applications is the one-tissue model (Figure 2), which describes the bidirectional flux of tracer between blood and tissue. Note that in kinetic modeling flow is generally not measured in terms of volume per time, as one might expect, but rather in terms of perfusion of tissue, which is described as volume per unit time per unit volume of tissue. Thus, the words *flow* and *perfusion* are used interchangeably in PET.

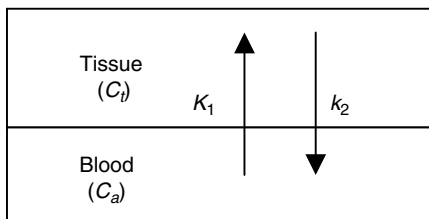


FIGURE 2 This one-tissue compartment model describes the bidirectional flux of tracer between blood (C_a) and tissue (C_t). The net tracer flux into tissue equals the flux entering the tissue ($K_1 C_a$) minus the flux leaving the tissue ($k_2 C_t$).

The model is characterized by the time-varying tracer concentration in tissue, $C_t(t)$, and arterial blood, $C_a(t)$ and two first-order kinetic rate constants (K_1 , k_2). The tracer concentrations are measured in nanocuries per milliliter (nCi/ml). Throughout the remainder of this chapter, we suppress the explicit time dependence of the concentration functions for notational simplicity. For example, $C_a(t)$ and $C_t(t)$ will be written simply as C_a and C_t .

It is assumed that within each compartment (blood and tissue) the tracer is homogeneously distributed. The unidirectional tracer flux from blood to tissue is $K_1 C_a$, and the flux from tissue to blood is $k_2 C_t$; therefore, the net tracer flux into tissue is:

$$\frac{dC_t}{dt} = K_1 C_a - k_2 C_t \quad (1)$$

Eq. (1) can be solved (see Appendix at the end of this chapter) for C_t to obtain:

$$C_t = K_1 C_a \otimes \exp(-k_2 t) \quad (2)$$

where the symbol \otimes denotes one-dimensional convolution.² If C_a and C_t are radioactivity concentrations, then k_2 (implicitly) includes a component for radioactive decay (see Section IVA). For a PET scan, C_t is the radioactivity concentration that is measured in a given tissue region. Blood samples may be drawn during a PET scan in order to measure C_a . If the tracer distribution in a tissue region is adequately described by the one-tissue model, then with serial measurements of C_t and C_a , Eq. (2) can be applied using standard nonlinear regression techniques to estimate the values of K_1 and k_2 for that region. We next develop an interpretation of these parameters in terms of the underlying physiology.

B. One-Compartment Model in Terms of Flow

The exchange of tracer between blood and tissue occurs either via diffusion or active transport across the capillary wall. Blood-flow tracers including $H_2^{15}\text{O}$ (also called ^{15}O -water) and ^{15}O -butanol pass via diffusion. In order to gain a better physiological understanding of the kinetic rate constants, it is instructive to first consider the passage of tracer within capillaries. For this purpose we can apply the model in Figure 2 on its smallest scale, such that the blood compartment represents a single capillary and the tissue compartment is the tissue in the immediate vicinity. Because some tracer is removed from the blood via extraction into tissue, the tracer blood concentration diminishes as it

²Elsewhere in this book, the symbol $*$ is used to denote convolution. The symbols \otimes and $*$ have the same meaning. The symbol \otimes is more customary in the kinetic modeling literature, whereas $*$ is more commonly used in the signal-processing literature. Equation (2) can be written explicitly as $C_t(t) = K_1 \int_0^t C_a(t') \exp[-k_2(t-t')] dt'$. The limits of integration are confined to 0 to t because the system is causal, and C_a is 0 for $t < 0$.

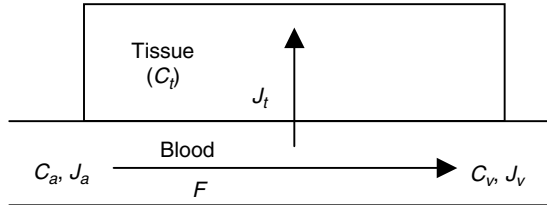


FIGURE 3 Tracer flow through a capillary. The values C_a and C_v are the tracer concentrations in arterial blood and venous blood, respectively, and C_t is the concentration in tissue. The tracer enters the capillary with flux J_a and leaves via tissue extraction (J_t) and the venous circulation (J_v). If tracer does not accumulate in the capillary, then the tracer flux into the capillary J_a equals the flux out of the capillary ($J_v + J_t$).

passes through the capillary. To include this effect in the one-tissue model, the blood compartment is extended as shown in Figure 3. The tracer enters the capillary from the arterial side with concentration C_a and exits the venous side with concentration C_v ; blood flows through the capillary with flow rate F . To derive a relation between these quantities we apply the Fick principle that states that when a compartment is at steady state, the flux of material that enters the compartment equals the flux that exits the compartment. In steady state, the concentration of material in the compartment does not change. According to the Fick principle, a steady state exists in the capillary as long as the tracer does not accumulate in the capillary itself. This condition is usually well satisfied because a tracer molecule that enters the capillary will rapidly leave by tissue extraction or via the venous circulation. From the Fick principle we get $J_a = J_t + J_v$, where J_a and J_v are the arterial and venous tracer fluxes, respectively. The arterial tracer flux equals the product of blood flow and the arterial tracer concentration, that is, $J_a = FC_a$. Similarly, the venous tracer flux is $J_v = FC_v$. The net tracer flux into tissue is the difference between the arterial and venous fluxes:

$$J_t = \frac{dC_t}{dt} = J_a - J_v = F(C_a - C_v) \quad (3)$$

The net fraction of the incoming tracer that is extracted into tissue during one capillary pass is called the net extraction fraction (E_n), and is equal to:

$$E_n = \frac{C_a - C_v}{C_a} \quad (4)$$

The unidirectional extraction fraction (E_u) refers only to tracer that is extracted from blood to tissue. During the first pass of a tracer through a tissue site, the tracer flux from tissue to blood is effectively zero because $C_t = 0$. In this case E_n is equal to E_u , which is often referred to as the first-pass extraction fraction. By setting $C_t = 0$ in Eq. (1), Eqs. (1), (3), and (4) can be arranged to give the net flux into tissue during the first pass

$$\frac{dC_t}{dt} = (FE_u)C_a = K_1 C_a \quad (5)$$

Thus, the delivery rate constant K_1 equals the product of blood flow and the unidirectional (first-pass) extraction fraction. The interpretation of E_u has been further developed from the Renkin-Crone capillary model, which considers the capillary to be a rigid cylindrical tube (Renkin, 1959; Crone, 1964). Based on the Renkin-Crone model a theoretical expression for the unidirectional extraction fraction has been derived

$$E_u = 1 - \exp(-PS/F) \quad (6)$$

where P is the permeability of the tracer across the capillary membrane, and S is the capillary surface area per unit mass of tissue. The product of permeability and surface area (PS) has the same units as blood flow (e.g., ml/min/ml). PS for water has been estimated at 133 ml/(min·100 g) (Berridge *et al.*, 1991) whereas the PS for butanol has been estimated to be 400 ml/(min·100 g) (Martin *et al.*, 1999). From Eq. (6) we see that, when PS is large relative to F , E_u approaches a maximum value of 1 and $K_1 \approx F$. At the other extreme, when F is large relative to PS , then $E_u \approx PS/F$, and $K_1 \approx PS$. Although these formulas are derived from simplified arguments (Sorenson and Phelps, 1987), they provide useful rules of thumb that give physiological meaning to K_1 . Figure 4a displays the relationship between extraction fraction as a function of flow for moderate and high PS products. Figure 4b plots extraction fraction times flow ($= K_1$) versus true flow.

To summarize, K_1 is closely related to blood flow when the extraction fraction is large, but is more related to permeability when the extraction fraction is small. Accordingly, the best tracers for studying blood flow have large extraction fractions (corresponding to $PS \gg F$). When blood flow is expected to be higher than normal, there is an added burden on the PS product to be high. Thus, Figure 5 shows a case of normal and high flow measured with two different tracers, ^{15}O -water and ^{15}O -butanol (Berridge *et al.*, 1991). When flow is high (provoked by the breathing of carbon dioxide), the measured K_1 of the tracer with the higher capillary permeability is better able to reflect the true flow value. PS for water has been estimated at 133 ml/(min·100 g) (Berridge *et al.*, 1991), whereas the PS for butanol has been estimated to be 400 ml/(min·100 g) (Martin *et al.*, 1999). Hence, even at high flow induced by carbon dioxide, we would expect extraction E_u of butanol to be unity and the flow estimate under that condition to be faithful to its true value.

C. Volume of Distribution/Partition Coefficient

Consider an experiment in which the tracer blood concentration is maintained at a constant level over time. In the tissue, tracer will accumulate with a time course

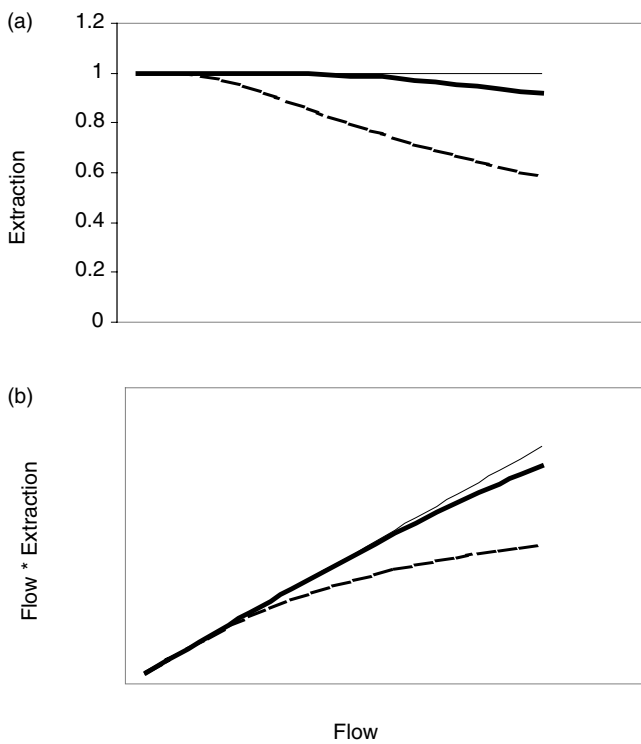


FIGURE 4 (a) Extraction fraction (E) versus flow (F). Solid curve is a highly extracted tracer. Dashed curve is a moderately extracted tracer. PS (permeability-surface area product) is higher for the former. Thin horizontal line is $E = 1$. (b) Flow times extraction fraction (i.e., apparent K_1 for blood flow model; see Eq. (5)) versus true flow. Dashed curve is for moderately extracted ligand; thick solid curve is for a highly extracted ligand. Notice the increasing deviation at large flow values. Thin diagonal line is line of identity.

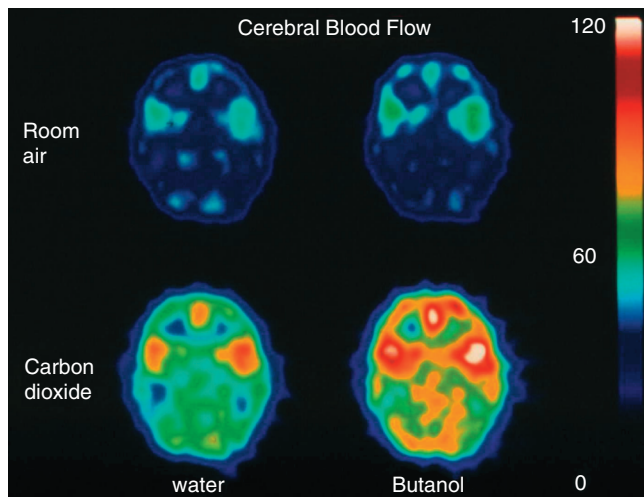


FIGURE 5 Blood flow scans using either ^{15}O -water or ^{15}O -butanol. At low flow rates (i.e., when subject breathes room air) the measured flow, K_1 , is very similar across ligands, whereas at high flow rates (i.e., induced by subject breathing carbon monoxide) the measured flow using ^{15}O -water is lower than that using ^{15}O -butanol because of the lower permeability of the blood-brain barrier to water. See Figure 4 for an explanation. (Figure supplied courtesy of Dr. Marc Berridge, Case Western Reserve University.)

described by Eq. (2). After sufficient time the net tracer flux between compartments is zero, and the system is said to be in equilibrium. At this point the blood and tissue concentrations are constant and the ratio of these concentrations C_t/C_a is called the equilibrium volume of distribution V_D (alternatively called the distribution volume, or partition coefficient). Although V_D is a ratio of concentrations (and hence dimensionless), it is called a volume because it equals the volume of blood that contains the same activity as 1 ml of tissue (Carson, 1996). For example, $V_D = 2$ means that at equilibrium the tracer in tissue is twice as concentrated as that in blood. That is, 2 ml of blood has the same quantity of radioactivity as 1 ml of tissue. Because the net tissue flux (Eq. 1) at equilibrium is zero, V_D can be expressed as:

$$V_D = \frac{C_t}{C_a} = \frac{K_1}{k_2} \quad (7)$$

For the one-tissue model, the volume of distribution is a macroparameter equal to K_1/k_2 . In general, the precise formulation of V_D in terms of the kinetic rate constants (K_1 , k_2 , ...) depends on the particular compartmental model employed (see further discussions in Sections IV and V). From the physiological interpretations of K_1 (the product of blood flow and extraction) and V_D (the ratio of C_t/C_a at equilibrium), k_2 can be defined as the ratio of K_1 to V_D . In most experimental paradigms, it is easier to measure V_D than its constituent parameters, and this is often just as useful for interpreting results. A common experimental technique used to measure V_D is to deliver tracer via continuous infusion in order to maintain C_a at a constant level. Once tissue equilibrium is achieved, V_D is easily obtained from blood and tissue measurements using Eq. (7).

D. Blood Flow

An important application of the one-tissue model is the measurement of regional blood flow. Blood flow can be described as the volume of blood that passes through a blood vessel per unit time (e.g., ml/min). However, the regional measurement of blood flow is typically expressed as the blood flow per unit mass of tissue (e.g. ml/min/mg), which is also called *perfusion*. When referring to PET studies, perfusion or blood flow per unit mass is simply called *blood flow*. The tracer that is most commonly used to measure blood flow with PET is ^{15}O -water (Herscovitch *et al.*, 1983; Raichle *et al.*, 1983). Because ^{15}O -water is rapidly diffusible, the tissue concentration equilibrates with the venous outflow, such that these concentrations are related by $V_D = C_t/C_v$. Substitution of this expression into Eq. (3) gives:

$$\frac{dC_t}{dt} = F \left(C_a - \frac{C_t}{V_D} \right) \quad (8)$$

Equation (8) can be solved for C_t as a function of F and V_D :

$$C_t(t) = FC_a(t) \otimes \exp\left(-\frac{F}{V_D}t\right) \quad (9)$$

For the practical application of Eq. (9), the distribution volume is generally fixed to some predetermined value (Iida *et al.*, 1989), leaving F as the only unknown parameter. To estimate blood flow with Eq. (9), C_t is computed over a range of F values that encompass the expected range of blood-flow values. This procedure generates a lookup table that can be used to convert the tissue measurements to flow values. In the case of PET, which measures the integral of the tissue curve, Eq. (9) is integrated over the same time range as the PET acquisition to produce a lookup table that relates $\int C_t dt$ to F (Muzic *et al.*, 1990). This technique is readily adaptable to parametric (pixel-by-pixel) calculations.

E. Dispersion, Delay Corrections

The measurement of blood flow with Eq. (9) is highly sensitive to the measurement accuracy of the arterial input function. To improve the accuracy, we need to account for subtle differences between the *measured* arterial input function (C_{am}), and the arterial concentration at the site of tissue measurement (C_a , considered the true input function). The discrepancies between the true and measured input functions are largely due to delay and dispersion. A time delay (Δt) occurs because the tracer generally requires different amounts of time to reach the sites of tissue measurement versus the sites of arterial sampling, due to differences in circulation distance. For example, ^{15}O -water usually reaches the brain before it is detected at the contralateral arterial sampling site. In addition, dispersion of the tracer will cause different degrees of smoothing of the input function, which results in C_{am} and C_a having different shapes. Dispersion (D) can be described as a monoexponential function of time:

$$D = \frac{1}{\tau} \exp\left(-\frac{t}{\tau}\right) \quad (10)$$

where τ is the dispersion time constant (Iida *et al.*, 1986). Accounting for delay and dispersion, the true and measured input functions are related according to:

$$C_{am}(t) = C_a(t + \Delta t) \otimes \frac{1}{\tau} \exp\left(-\frac{t}{\tau}\right) \quad (11)$$

In order to determine the true input function C_a , two more parameters (τ and Δt) must be estimated. Several procedures have been developed to determine these values (Raichle *et al.*, 1983; Meyer, 1989; Ohta *et al.*, 1996; Muzic *et al.*, 1993; Nelson *et al.*, 1990). The delay and dispersion corrections must be applied before Eq. (9) is used to generate a lookup table. The discrepancy between C_a and C_{am} due to

delay and dispersion is negligible after a few minutes. As a result, their effects are most evident in blood-flow studies, which are usually just a few minutes in duration. For most other applications (e.g., studies with receptor binding tracers), the study duration is 60 minutes or more and differences between C_a and C_{am} are generally ignored.

F. Noninvasive Methods

A method has been introduced to measure blood flow without an arterial input function. Instead, the method of Watabe *et al.* (1996) relies on measuring two independent tissue curves: one the whole brain curve and the other a gray-matter curve. The curves are assumed to have identical arterial inputs but different flows and volumes of distribution. Volume of distribution, V_D , in the grey matter is assumed to be known. Three remaining parameters are estimated: flow in whole brain, flow in grey matter, and V_D in whole brain. Unfortunately, if the two curves are not sufficiently independent, the method was found in practice to be highly sensitive to noise (H. Watabe, personal communication). Noninvasive methods (i.e., not requiring an arterial curve) have been used more successfully in receptor-ligand studies and are examined in detail in Section V.

G. Tissue Heterogeneity

As stated in Section II A, the one-compartment model includes the assumption that tracer in the tissue compartment is homogeneously distributed. The spatial resolution of the current generation of PET scanners, however, is on the order of 4–6 mm full width at half maximum (FWHM) (see, e.g., Pajevic *et al.*, 1998), whereas gray matter in human cortex forms a winding band only 2–3 mm wide. Most brain regions measured with PET, especially cortical regions, therefore contain mixtures of gray and white matter that have different concentrations of tracer due to their differing rates of blood flow. Analysis of data on a pixel-by-pixel basis, even though the pixels may be reconstructed to be ~2 mm on a side, does not eliminate the heterogeneity problem because the minimum object size for accurate quantification is $2 \times \text{FWHM}$ (Hoffman *et al.*, 1979). Because blood flow is higher in gray matter than in white matter, the partial-volume effect leads to underestimation of flow in gray matter when blood flow in the region as a whole is determined. Weighted average blood flow is underestimated as well and falls with increasing experimental duration if the kinetic model used in the analysis fails to account for the tissue heterogeneity (Schmidt *et al.*, 1989). In simulations of PET H_2^{15}O studies, errors in weighted average flow due to heterogeneity have been estimated to range from < 5% in short-duration studies (Herscovitch *et al.*, 1983; Koeppe *et al.*, 1985) to approximately 20% in longer-duration studies (Koeppe *et al.*, 1985).

Due to the unavoidable inclusion of white matter in each region of measurement, weighted average flow in a nominally gray matter region depends on the amount of white matter included. In order to determine gray matter flow, corrections for the partial-volume effect have been developed that are based on the use of a high-resolution magnetic resonance image of the subject coregistered to the PET image. More recently, methods to determine gray matter flow based on the PET data alone have been proposed (Iida *et al.*, 2000; Law *et al.*, 2000; Schmidt and Sokoloff, 2001).

III. POSITRON EMISSION TOMOGRAPHY MEASUREMENT OF REGIONAL CEREBRAL GLUCOSE USE

The $[^{18}\text{F}]$ fluorodeoxyglucose ($[^{18}\text{F}]$ FDG) method is used for the quantitative measurement of regional cerebral glucose use ($r\text{CMR}_{\text{glc}}$) in man and in animals. Because a close relationship has been established between functional activity and cerebral glucose use in discrete brain regions (Sokoloff, 1977), the method can be used to investigate regional changes in functional activity in various physiological and pathological states. The $[^{18}\text{F}]$ FDG method was first developed for use with single-photon emission computerized tomography (SPECT) (Reivich *et al.*, 1979) and shortly thereafter adapted for use with PET (Phelps *et al.*, 1979). The $[^{18}\text{F}]$ FDG method was derived from the autoradiographic $[^{14}\text{C}]$ deoxyglucose ($[^{14}\text{C}]$ DG) method for measuring local cerebral glucose use in animals (Sokoloff *et al.*, 1977). $[^{14}\text{C}]$ DG was specifically chosen as the tracer because its already well-known biochemical properties facilitated the design and analysis of a kinetic model that described the brain–plasma exchange of $[^{14}\text{C}]$ DG and its phosphorylation by hexokinase in relation to those of glucose.

A. The Basic Compartmental Model

The model for the measurement of cerebral glucose use with $[^{18}\text{F}]$ FDG in a homogeneous tissue in brain is based on that of $[^{14}\text{C}]$ DG (Sokoloff *et al.*, 1977) and includes two tissue compartments (Figure 6). $[^{18}\text{F}]$ FDG and glucose in the plasma cross the blood–brain barrier by a saturable carrier-mediated transport process. Because $[^{18}\text{F}]$ FDG and glucose compete for the same carrier, the rate of inward transport of $[^{18}\text{F}]$ FDG can be described by the classical Michaelis-Menten equation modified to include the influence of the competitive substrate, that is,

$$v_i^*(t) = \frac{V_t^* C_p^*(t)}{K_t^* [1 + C_p(t)/K_t] + C_p^*(t)} \quad (12)$$

where v_i^* is the velocity of inward transport; C_p^* and C_p are the concentrations of $[^{18}\text{F}]$ FDG and glucose,

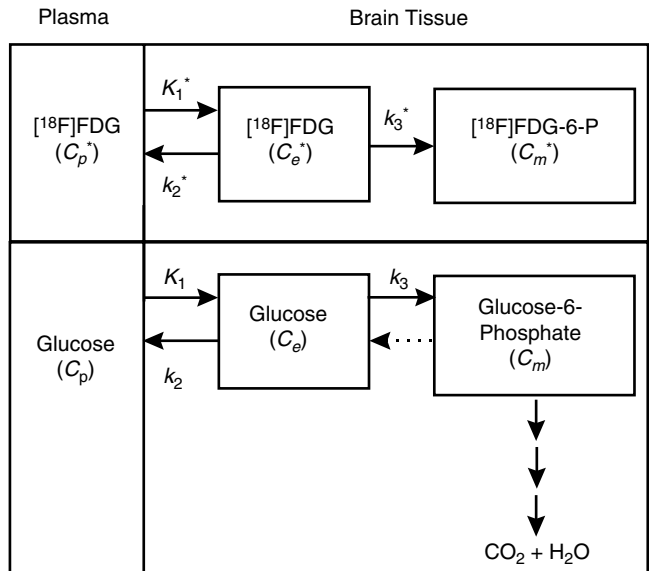


FIGURE 6 Model for measurement of cerebral glucose use with $[^{18}\text{F}]$ fluorodeoxyglucose ($[^{18}\text{F}]$ FDG) in a homogeneous tissue. C_p^* and C_p represent the concentrations of $[^{18}\text{F}]$ FDG and glucose in the arterial plasma, respectively; C_e^* and C_e are the concentrations of $[^{18}\text{F}]$ FDG and glucose in the exchangeable pool in the tissue; C_m is the concentration of metabolites of $[^{18}\text{F}]$ FDG in the tissue, predominately $[^{18}\text{F}]$ fluorodeoxyglucose-6-phosphate; and C_m is the concentration of metabolites of glucose in the tissue. The PET signal includes the sum of C_e^* , C_m , and the concentration of $[^{18}\text{F}]$ FDG in the blood in the brain. The constants K_1^* and K_2^* represent the first-order rate constants for carrier-mediated transport of $[^{18}\text{F}]$ FDG from plasma to tissue and back from tissue to plasma, respectively. k_3^* represents the first-order rate constant for phosphorylation of $[^{18}\text{F}]$ FDG by hexokinase. The respective rate constants for glucose are K_1 , k_2 , and k_3 . The model allows for the possibility that some of the phosphorylated glucose may return to the precursor pool (dashed arrow). (Adapted from Sokoloff *et al.*, 1977.)

respectively, in the plasma; V_t^* is the maximal velocity of $[^{18}\text{F}]$ FDG transport; K_t^* and K_t are the apparent Michaelis-Menten constants of the carrier for $[^{18}\text{F}]$ FDG and glucose, respectively; and t is the variable time. Because $[^{18}\text{F}]$ FDG is administered in tracer amounts, $C_p(t)$ can be considered negligible compared to $K_t^* [1 + C_p(t)/K_t]$. If the glucose concentration in the plasma is constant, then the velocity of inward transport can be expressed as $K_1^* C_p^*(t)$, where $K_1^* = V_t^*/[K_t^* (1 + C_p/K_t)]$ is a first-order rate constant. Once $[^{18}\text{F}]$ FDG is in the tissue, it can either be transported back to the plasma or phosphorylated to $[^{18}\text{F}]$ fluorodeoxyglucose-6-phosphate ($[^{18}\text{F}]$ FDG-6-P), processes that follow Michaelis-Menten equations analogous to Eq. (12). When cerebral glucose use is in steady state, the concentration of glucose in brain (C_p) is constant and both outward transport and phosphorylation of $[^{18}\text{F}]$ FDG can be considered first-order processes. Thus the rate of change of the $[^{18}\text{F}]$ FDG concentration in the exchangeable pool in the tissue can be described by the equation:

$$\frac{dC_e^*}{dt} = K_1^* C_p^*(t) - (k_2^* + k_3^*) C_e^*(t) \quad (13)$$

where $C_p^*(t)$ (in nCi/ml plasma) represents the concentration of [¹⁸F]FDG measured in the arterial plasma t minutes after its injection into the venous blood; $C_e^*(t)$ (in nCi/g brain tissue) is the concentration of unmetabolized tracer in the exchangeable pool in the tissue; K_1^* (in ml plasma/g brain/min) and k_2^* (in min⁻¹) represent the first-order rate constants for transport of [¹⁸F]FDG from plasma to tissue and back from tissue to plasma, respectively; and k_3^* (in min⁻¹) represents the first-order rate constant for phosphorylation of [¹⁸F]FDG by hexokinase. K_1^* , k_2^* , and k_3^* are constant with respect to time, but vary regionally and with different plasma and brain concentrations of glucose.

The advantage of using [¹⁸F]FDG rather than labeled glucose as the tracer is that the primary and secondary products of its phosphorylation, unlike those of glucose, are trapped in the tissue and accumulate where they are formed for reasonably prolonged periods of time.³ Therefore, the rate of change in the concentration of products of [¹⁸F]FDG metabolism in the tissue, $C_m^*(t)$, is

$$dC_m^*/dt = k_3^* C_e^*(t) \quad (14)$$

and the total concentration of activity in the tissue, $C_i^*(t)$, is the sum of the concentrations in the precursor and product tissue pools:

$$C_i^*(t) = C_e^*(t) + C_m^*(t) \quad (15)$$

The PET scanner measures all activity in the field of view, both intra- and extravascular. Thus the total concentration of activity measured by the scanner, $C_t^*(t)$, is

$$C_t^*(t) = (1 - V_B)C_i^*(t) + V_B C_B^*(t), \quad (16)$$

where V_B is the fraction of the measured volume occupied by blood ($0 \leq V_B \leq 1$) and $C_B^*(t)$ is the concentration of label in whole blood. In the human, brain–blood volumes in gray and white matter are about 4 and 2%, respectively (Phelps *et al.*, 1979).

The kinetic model for glucose uptake and metabolism in the tissue is equivalent to that of [¹⁸F]FDG, except that glucose-6-phosphate is not trapped in the tissue but continues down the glycolytic pathway eventually to CO₂ and H₂O (Figure 6). The model allows for the possibility that some of the phosphorylated glucose may return to the precursor pool. In steady state, the constant fraction of the glucose that, once phosphorylated, continues down the glycolytic pathway is designated by Φ ; in brain $\Phi \approx 1$ (Sokoloff *et al.*, 1977).

B. Protocol for Measurement of Regional Cerebral Glucose Use

Because the model describing the kinetics of [¹⁸F]FDG and glucose *in vivo*, like all models representing biological events, is necessarily a simplified description that cannot fully account for all potentially relevant factors, the experimental procedure of the [¹⁸F]FDG method, like that of the autoradiographic [¹⁴C]DG method, was designed to minimize possible errors arising from limitations and/or imperfections of the kinetic model. The rationale for the procedure is made clear by the examination of the originally reported operational equation that applies to both methods (Sokoloff *et al.*, 1977). Regional cerebral glucose use is calculated as:

$$rCMR_{glc} = \frac{C_t^*(t) T - K_1^* \int_0^T C_p^*(t) e^{-(k_2^* + k_3^*)(T-t)} dt}{\left(\frac{V_m^* K_m}{V_m K_m^*} \right) \left(\frac{\lambda}{\Phi} \right) \left(\int_0^T \frac{C_p^*(t)}{C_p} dt - \int_0^T \frac{C_p^*(t)}{C_p} e^{-(k_2^* + k_3^*)(T-t)} dt \right)} \quad (17)$$

where C_t^* , C_p^* , K_1^* , k_2^* , k_3^* , and C_p are as defined in Section IIIA. The first bracketed term in the denominator relates the relative preference of hexokinase for glucose over that for FDG; its components are V_m and K_m , the maximal velocity and Michaelis-Menten constant of hexokinase for glucose; and V_m^* and K_m^* , the equivalent kinetic constants of hexokinase for FDG. In the second term in the denominator λ represents the ratio of the distribution spaces of FDG and glucose, and Φ converts the rate of glucose phosphorylation into the net rate of glucose use. The first two terms together comprise the lumped constant of the method, so called because the six constants Φ , V_m , K_m , V_m^* , K_m^* , and λ have been lumped together. The lumped constant is discussed in Section IIIE.

In Eq. (17), the least reliable terms, those that depend on the kinetic model and rate constants, can be minimized by use of an optimally chosen experimental protocol. The numerator of Eq. (17) approximates the concentration of labeled products of [¹⁸F]FDG phosphorylation formed in the tissue during the experimental period; this is determined as the difference between total radioactivity measured by PET (C_t^*) and a term that represents the estimated C_e^* , the free unmetabolized [¹⁸F]FDG still remaining in the exchangeable pool in the tissue at the end of the experimental period. In order to minimize the free [¹⁸F]FDG in the tissue, a long period of tracer circulation after a pulse of [¹⁸F]FDG is used; C_t^* then represents mainly labeled products of [¹⁸F]FDG phosphorylation. C_t^* should also be corrected for blood volume and residual blood activity, but these correction factors are negligible and usually omitted. In the denominator of the operational equation, a term that corrects for the lag in equilibration of the tissue precursor pool behind the plasma is subtracted from the integrated specific activity measured

³When the [¹⁸F]FDG method was first adapted for use with PET, only relatively slow scanners were available. In some studies, tissue activity was measured as long as 14 hours after injection of [¹⁸F]FDG when product loss was clearly observable, and a term for product loss was added to the kinetic model (Phelps *et al.*, 1979; Huang *et al.*, 1980). In studies of 2 h or less in duration there is no evidence for loss of metabolic products (Schmidt *et al.*, 1992; Lucignani *et al.*, 1993).

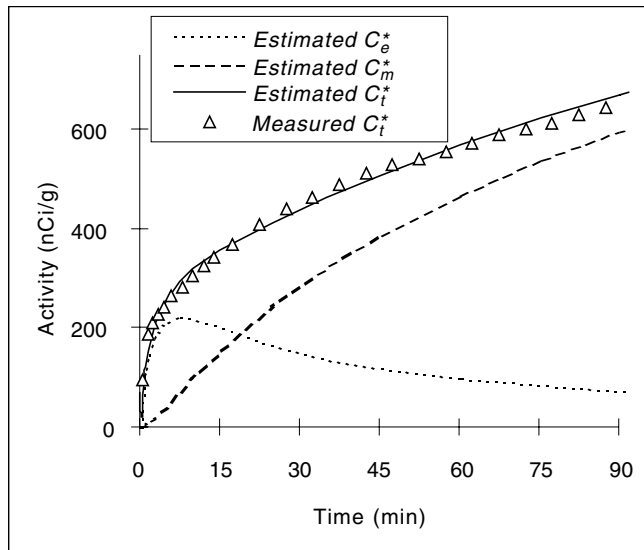


FIGURE 7 Time course of measured activity in visual cortex of a normal subject (open triangles), and model-estimated concentrations of total $[^{18}\text{F}]$ FDG (C_t^* , solid line), and $[^{18}\text{F}]$ FDG (C_e^* , dotted line), and $[^{18}\text{F}]$ FDG-6-P (C_m^* , dashed line). Activity in the blood pool is not shown. Note that application of the homogeneous tissue $[^{18}\text{F}]$ FDG model to the heterogeneous region results in systematic errors in the model-estimated total activity. All data are decay-corrected. (Data from Lucignani *et al.*, 1993.)

in the plasma. The magnitude and, therefore, impact of this correction term is also minimized by the use of the long period of tracer circulation after the pulse. Because the total $[^{18}\text{F}]$ concentration in the tissue and the integrated plasma specific activity are increasing while the correction terms that are subtracted from them are decreasing with time after a pulse, the effects of errors in the estimates of these correction terms diminish with time. The experimental period cannot be extended indefinitely, however, because the loss of products of $[^{18}\text{F}]$ FDG phosphorylation eventually becomes significant.

Estimated time courses of the activity in the various tissue components are shown in Figure 7.

C. Estimation of Rate Constants

When only single-ring (relatively inefficient and slow) PET scanners were available, several hours were required to scan the entire brain, and the strategy for determination of the rate constants was the same as that for the $[^{14}\text{C}]$ DG method; they were estimated in a separate group of subjects by nonlinear least squares fitting of the model equation to the measured time courses of total $[^{18}\text{F}]$ activity in various brain regions. The rate constants estimated from several individuals were averaged, and the population average rate constants were subsequently used with each new subject's measured final $[^{18}\text{F}]$ concentration in brain regions of interest and the time course of arterial plasma specific activity to calculate $rCMR_{\text{glc}}$ by means of Eq. (17). More recent

generations of scanners contain multiple rings that allow the entire brain to be scanned simultaneously; their increased efficiency also allows more rapid acquisition of multiple time frames of data. This has made it technically possible to obtain statistically reliable time courses of total radioactivity and to estimate rate constants in each region for each individual subject. It was expected that obtaining rate constants for each individual would lead to improvements in accuracy in the rate-constant-dependent terms of Eq. (17), which, in turn, would allow studies to be completed in shorter total scanning times. Problems arising from tissue heterogeneity, however, have limited the extent to which studies can be shortened, as discussed in Section IIIE.

D. The Lumped Constant

The lumped constant is a unitless physical constant used to convert rates of $[^{18}\text{F}]$ FDG uptake and phosphorylation into rates of glucose use. The directly measured value of the lumped constant for $[^{18}\text{F}]$ FDG in whole brain in humans under normal physiological conditions is 0.52 (Reivich *et al.*, 1985). Although it is difficult to measure the lumped constant under nonphysiological conditions in humans, it is expected that the lumped constant for $[^{18}\text{F}]$ FDG in humans should have similar properties to the lumped constant for deoxyglucose that has been extensively studied in animals. The lumped constant for deoxyglucose has been shown to be relatively stable over a wide range of plasma glucose concentrations in normal brain (Sokoloff *et al.*, 1977). It is influenced mainly by plasma and tissue glucose levels, falling progressively but very gradually with increasing plasma glucose levels all the way to severe hyperglycemia (Schuier *et al.*, 1990). When glucose supply is limiting, such as in hypoxemia, ischemia, or extreme hypermetabolism, the lumped constant may increase considerably (Suda *et al.*, 1990). In such cases it is important to estimate the value of the lumped constant locally, possibly from measurements of the brain uptake of methylglucose (Gjedde *et al.*, 1985; Dienel, Cruz, *et al.*, 1991). Less than extreme changes in glucose metabolism have only small effects on the lumped constant (Dienel, Nakanishi, *et al.*, 1991).

E. Tissue Heterogeneity

The kinetic model of Figure 6 was specifically designed for a homogeneous tissue within which rates of blood flow, glucose metabolism, transport of glucose and $[^{18}\text{F}]$ FDG between tissue and blood, and so on are uniform. As described in Section II G, the limited spatial resolution of the PET scanner assures that most brain regions, especially cortical regions, contain mixtures of gray and white matter. Figure 8 shows total activity in one image plane following a pulse of $[^{18}\text{F}]$ FDG and a magnetic resonance image (MRI) of the same subject. A small region of interest $2 \times \text{FWHM}$

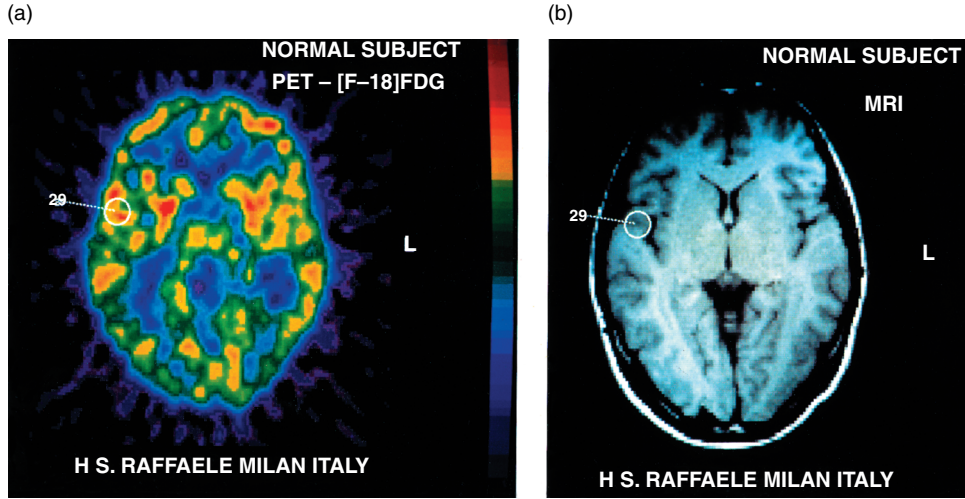


FIGURE 8 Total activity in one image plane obtained 115–120 min following (a) a pulse of $[^{18}\text{F}]$ FDG and (b) a magnetic resonance image (MRI) of the same normal subject. PET image was obtained with a Siemens/CPS whole-body positron emission tomograph (model 931/04-12) with spatial resolution in the image plane of 8 mm FWHM. A small region of interest 2 FWHM in diameter in the superior temporal gyrus is shown; both gray and white matter are included. (Reproduced from Schmidt *et al.*, 1992.)

in diameter, the minimum object size for accurate quantification (Hoffman *et al.*, 1979), is shown in the superior temporal gyrus; it includes both gray and white matter. Because gray and white matter are kinetically heterogeneous, their unavoidable admixture in PET data must be taken into account in the kinetic model (Figure 9).

Ideally, one would like to determine the rate of glucose use separately in the gray and white matter in each region of interest, and various methods to correct for partial volume effects⁴ have been proposed. These methods usually require a co-registered structural image (e.g., MRI) and may require some additional assumptions about the composition of the volume. An alternative is to determine the average value of the rate of glucose use or the average values of the kinetic parameters, properly weighted for the relative masses of the constituents in the mixed tissue. Use of the kinetic model designed for homogeneous tissues to analyze PET data results in errors in estimates of the rate constants and $rCMR_{\text{glc}}$; the magnitude of the errors depends on the total time over which the data are collected. Estimates of k_2^* and k_3^* initially decline with time and become constant and equal to their true mass-weighted average values only after the experimental periods have been extended long enough for the tissue pools of $[^{18}\text{F}]$ FDG to equilibrate with the arterial plasma (Kuwabara *et al.*, 1990; Schmidt *et al.*, 1991, 1992). Overestimation of the rate constants k_2^* and k_3^* , because it leads to underestimation in the amount of free $[^{18}\text{F}]$ FDG in

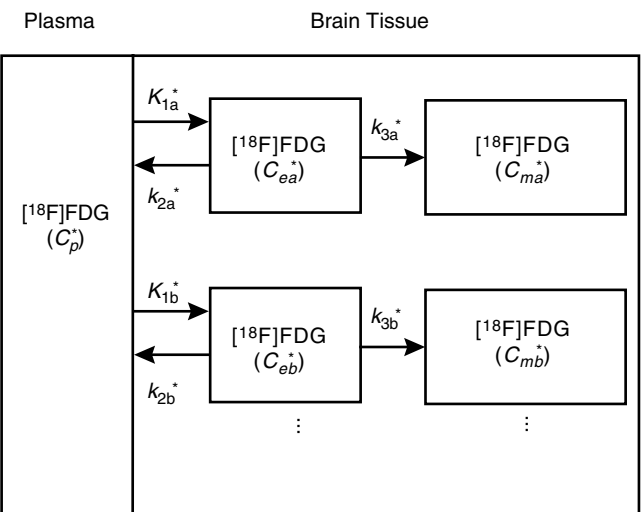


FIGURE 9 Schematic diagram of a heterogeneous tissue as a collection of multiple homogeneous subregions; the kinetic model of each homogeneous subregion is as presented in Figure 6. C_p^* represents the concentration of $[^{18}\text{F}]$ FDG in the arterial plasma; C_{ea}^* , C_{eb}^* , ... represent the concentrations of $[^{18}\text{F}]$ FDG in the exchangeable pool of each homogeneous subregion of the heterogeneous brain tissue; and C_{ma}^* , C_{mb}^* , ... represent the concentrations of metabolites of $[^{18}\text{F}]$ FDG in the corresponding homogeneous subregions. The PET signal includes the sum of the activities in all the subregions, each weighted by its relative mass, plus the concentration of $[^{18}\text{F}]$ FDG in the blood in the brain. Rate constants for each homogeneous subregion are as defined in Figure 6. (Adapted from Schmidt *et al.*, 1991.)

⁴The partial-volume effect is called this because only part of the total volume is occupied by the tissue of interest (e.g., gray matter); bias is introduced into its measurement by the presence of other tissues within the volume.

the exchangeable pool in the tissue (second term in the numerator of Eq. 17), results in overestimation of the rate of glucose use. In addition, if the homogeneous kinetic model is modified to include the possibility of loss of $[^{18}\text{F}]$ FDG-6-P and the resultant model is applied to

heterogeneous tissues, estimates of the rate constant for product loss are artificially high due to the tissue heterogeneity, even in the absence of any real product loss, at least up to 120 min following a pulse of [¹⁸F]FDG (Schmidt *et al.*, 1991, 1992; Lucignani *et al.*, 1993). Overcorrection for product loss results in further overestimation of $rCMR_{glc}$. The optimal period for obtaining the best estimates of the mass-weighted average kinetic model rate constants is the period beginning at the time of tracer injection and continuing for a minimum of 60 min, but not longer than 120 min (Lucignani *et al.*, 1993). Such prolonged dynamic scanning periods, however, are impractical on a routine basis, and population average rate constants must be used with Eq. (17) to determine $rCMR_{glc}$. In this case the scanning time to determine the final brain activity, $C_t^*(T)$, should be delayed as long as possible following the pulse of [¹⁸F]FDG (but not longer than 120 min) to minimize the effects of errors in the rate constants. Alternatively, tissue heterogeneity can be modeled explicitly, or methods that do not depend on tissue homogeneity can be employed.

1. Compartmental Model of Tissue Heterogeneity

A compartmental model that explicitly takes tissue heterogeneity into account has been developed (Schmidt *et al.*, 1991, 1992). In the first 120 min following the pulse of [¹⁸F]FDG, the model can be used to describe accurately the time course of radioactivity in a heterogeneous tissue without any assumption of loss of metabolic product. Determination of the parameters of the model, however, requires dynamic scanning from the time of tracer injection until after all tissue precursor pools have equilibrated with the arterial plasma, a scanning period of not less than 60 min (Schmidt *et al.*, 1992). For this reason, the model is of less practical use for determination of $rCMR_{glc}$ than the methods described next.

2. Multiple-Time Graphical Analysis Technique

An alternative to the use of specific compartmental models is the multiple-time graphical analysis technique, the Patlak plot (Patlak *et al.*, 1983; Patlak and Blasberg, 1985), that applies equally well to heterogeneous as to homogeneous tissues. Application of the Patlak plot is restricted to an interval of time in which (1) the free [¹⁸F]FDG in all tissue-exchangeable pools in the region of interest (e.g., in gray and white matter) has equilibrated with the [¹⁸F]FDG in the plasma, and (2) there is no product loss. During this interval, the apparent distribution space for total ¹⁸F in the tissue, $C_t^*(T)/C_p^*(T)$, when plotted against the normalized integrated tracer concentration in arterial plasma, $\int_0^T C_p^*(t)dt/C_p^*(T)$, increases linearly with slope K directly proportional to $rCMR_{glc}$ (Figure 10). The rate of glucose use can then be estimated as:

$$rCMR_{glc} = KC_p / LC \quad (18)$$

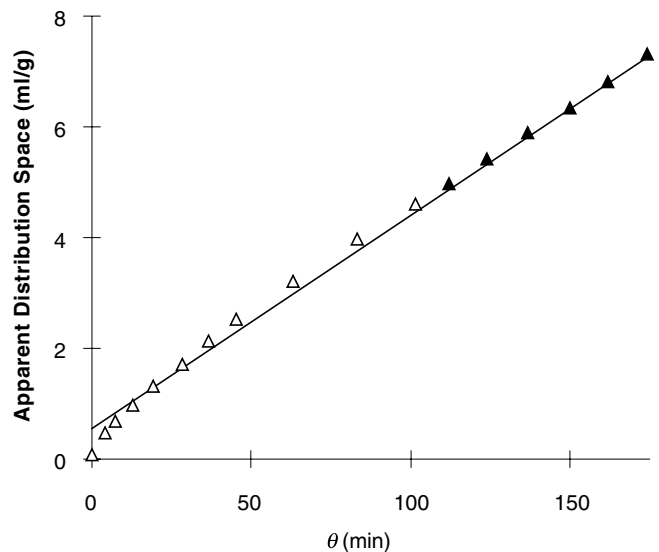


FIGURE 10 Patlak plot of data shown in Figure 7. Activity was measured in the visual cortex of a normal human subject. The normalized integrated tracer concentration in arterial plasma, $\theta(T) = \int_0^T C_p^*(t)dt/C_p^*(T)$, is plotted on the abscissa and the apparent distribution space for total ¹⁸F in the region, $C_t^*(T)/C_p^*(T)$, is plotted on the ordinate. Following equilibration of all precursor pools in the tissue with the arterial plasma, the plot becomes linear as long as there is no product loss; the slope of the linear portion of the graph is directly proportional to $rCMR_{glc}$. The unbroken line is the best fit to the data measured 60–90 min following a pulse of [¹⁸F]FDG (solid triangles). Open triangles represent measurements not included in the fit. (Data from Lucignani *et al.*, 1993.)

where LC is the lumped constant of the method and C_p is the arterial plasma glucose concentration. Because either lack of equilibration with the plasma of any precursor pool in the region of interest or loss of metabolic products may cause nonlinearity of the graph, application of this technique requires identification of an appropriate linear segment of the curve. There is evidence that there are slowly equilibrating compartments until approximately 45 min after a pulse of [¹⁸F]FDG, but in most tissue regions the estimated slope K , and hence the estimated value of $rCMR_{glc}$, is relatively stable in the interval between ~45 and ~105–120 min following the pulse of [¹⁸F]FDG (Lucignani *et al.*, 1993).

3. Spectral Analysis

A second alternative to the use of a fixed kinetic model is the spectral analysis technique that is based on a more general linear compartmental system (Cunningham and Jones, 1993; Cunningham *et al.*, 1993; Turkheimer *et al.*, 1994, 1998). The technique provides an estimate of the minimum number of compartments necessary to describe the kinetics of the system and hence does not require the number of compartments to be fixed *a priori*. It also provides estimates of the rate constant of trapping of tracer in the tissue, and the amplitudes and decay constants of the reversible components. This information can be used for subsequent specification of a kinetic model, or it can be used to estimate

selected parameters of the system that do not depend on the specific model configuration, for example, the rate of trapping of tracer, the unidirectional clearance of tracer from blood to tissue, the total volume of distribution of the tracer, or mean transit times (Cunningham *et al.*, 1993). Spectral analysis does not require that the system be in steady state.

The spectral analysis technique assumes that the total concentration of tracer in the field of view can be described by the equation:

$$C_t^*(T) = \alpha_0 \int_0^T C_p^*(t) dt + \sum_{j=1}^n \alpha_j \int_0^T C_p^*(t) e^{B_j(T-t)} dt + V_B C_B^*(T) \quad (19)$$

where C_t^* , C_p^* , C_B^* , and V_B are as defined in Section IIIA; n is the number of detectable compartments in the tissue; and α_j and B_j are scalar parameters that depend on exchange of tracer among the compartments. For radiotracers other than [¹⁸F]FDG C_p^* in Eq. (19) may represent arterial blood concentration, arterial plasma concentration, or metabolite-corrected, nonprotein-bound plasma concentration of activity depending on which fraction of radioactivity in the blood is exchangeable with the tissue. C_B^* , on the other hand, always relates to the total radioactivity in the blood pool. The exponents B_j are assumed to be nonpositive real numbers and the coefficients α_j to be nonnegative real numbers. When the spectral analysis technique is applied to the analysis of [¹⁸F]FDG data, the rate of glucose use is directly proportional to the coefficient α_0 :

$$rCMR_{\text{glc}} = \alpha_0 C_p / LC \quad (20)$$

where C_p and LC are as previously defined. It is often necessary to apply a noise filter in order to obtain an accurate estimate of α_0 (Turkheimer *et al.*, 1994).

Spectral analysis does not apply to all linear compartmental systems, but a class of systems to which it does apply has been identified (Schmidt, 1999). These include noncyclic⁵ strongly connected⁶ systems that have an exchange of material with the environment confined to a single compartment, as well as certain noncyclic systems with traps. Furthermore, a noninterconnected collection of compartmental systems meets the conditions for application of spectral analysis when the individual subsystems making up the collection individually meet the spectral analytic conditions. This property renders the spectral analysis technique particularly useful for tracer kinetics studies in brain with PET where the limited spatial resolution leads to inclusion of kinetically dissimilar gray and white matter tissues in the field of view (See Figure 11). Spectral analysis is applicable to the one-compartment kinetic model used for the measurement of

⁵A cyclic compartmental system is one in which it is possible for material to pass from a given compartment through two or more other compartments and back to the starting compartment.

⁶In strongly connected systems it is possible for material to reach every compartment from every other compartment.

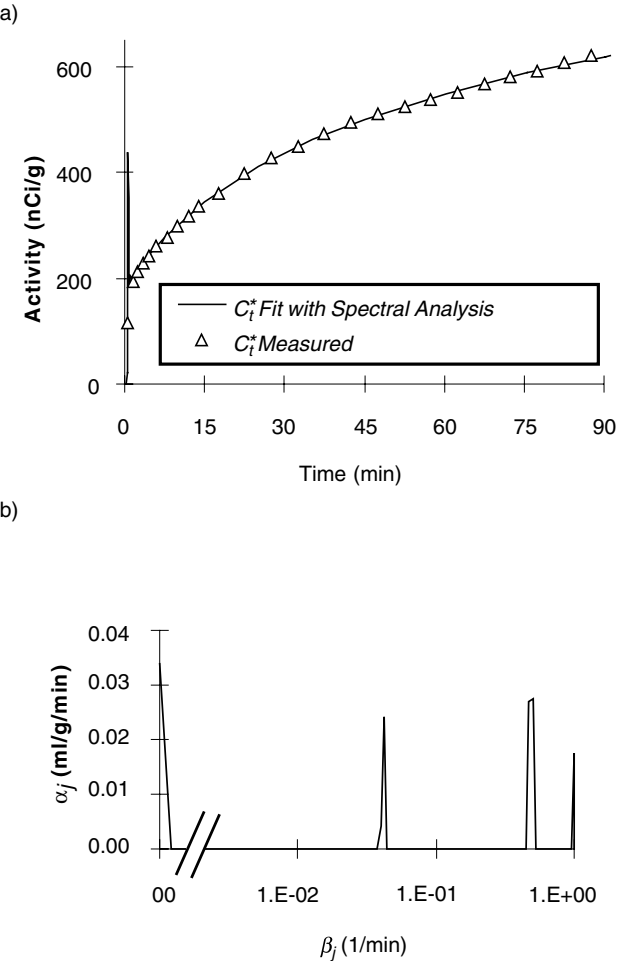


FIGURE 11 Spectral analysis of data shown in Figure 7. Activity was measured 0–90 min following a pulse of [¹⁸F]FDG in the visual cortex of a normal human subject. (a) Total activity in the region, measured (open triangles) and estimated (line). Early spike is due to radioactivity in the blood pool. (b) Components detected by the analysis. The exponent β_j is plotted on the abscissa and the coefficient α_j on the ordinate. In addition to a blood component (not shown), a component corresponding to trapped tracer ($\beta_j = 0$) and three equilibrating components were found. The equilibrating components have been associated with gray matter ($\beta_j = 0.5/\text{min}$), white matter ($\beta_j = 0.04/\text{min}$), and noise in the input function ($\beta_j = 1.0/\text{min}$) (Data from Turkheimer *et al.*, 1994.)

cerebral blood flow with H₂¹⁵O and PET (Huang *et al.*, 1983; Herscovitch *et al.*, 1983), the two-compartment model for measurement of glucose metabolism with [¹⁸F]FDG, and some three-compartment models used in receptor-ligand binding studies, such as those designed to assess muscarinic cholinergic receptor binding by use of [¹¹C]scopolamine (Frey *et al.*, 1985) or to assess benzodiazepine receptor density by use of [¹¹C]flumazenil (Koeppe *et al.*, 1991). The heterogeneous counterparts of each of these models can also be analyzed with spectral analysis due to the additivity of the components in Eq. (19) and the observation that the activity in a heterogeneous mixture of tissues is simply the weighted

sum of the activity in the constituent tissues making up the mixture.

IV. RECEPTOR-LIGAND MODELS

A. Three-Compartment Model

The simplest of compartmental models applied to receptor-ligand studies postulates two tissue compartments. These two tissue compartments along with a plasma compartment⁷ are arranged in series. The tracer is delivered—typically by intravenous (iv) injection—into the blood, and it traverses the free compartment on its way to interacting with the receptor. If these three states of the radioligand are inadequate to describe the data, sometimes a third tissue compartment is introduced (Figure 12), which is termed the nonspecifically bound compartment. The bound and nonspecific compartments are distinguished as follows. Specifically, a bound ligand (unlike a nonspecifically bound one) is both saturable and displaceable by nonradioactive molecules of the same tracer. The rate of change in radioactivity concentration in each tissue compartment in Figure 12 is given by the ordinary differential equations that describe the flux of ligand into (and out of) the respective compartments:

$$\frac{dF}{dt} = K_1 P - (k_2 + k_3)F + k_4 B - \lambda F - k_5 F + k_6 N \quad (21)$$

$$\frac{dB}{dt} = k_3 F - k_4 B - \lambda B \quad (22)$$

$$\frac{dN}{dt} = -\lambda N + k_5 F - k_6 N \quad (23)$$

where F , B , and N are the time-varying concentrations of tracer in the free, bound, and nonspecific tissue compartments, respectively. That is, $F = F(t)$, $B = B(t)$, and $N = N(t)$. K_1, k_2, \dots, k_6 are the apparent first-order rate constants relating the transfer of ligand between the various compartments. These k s are the model parameters to be estimated from experimental data. The parameters, k_3 and k_4 , are apparent first-order rate constants that characterize the binding and dissociation of the ligand to and from the receptor, respectively. The rate constant, λ , for radioactive decay, refers to the rate constant of conversion of the isotope labeling the ligand. As the isotope decays (with half-life = $\ln(2)/\lambda$) to a nonradioactive species, the labeled molecule is effectively lost from the system. P is the (measured) concentration of radioactive ligand in the plasma. P refers only to the concentration of native ligand molecules and not to any radioactive metabolites. The preceding model, in a

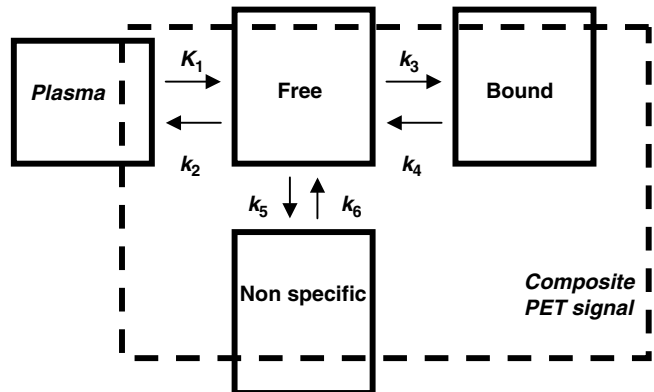


FIGURE 12 General three-compartment model. Some fraction of the radioactivity in each of the plasma, free, bound (and nonspecific) compartments sum to give the radioactivity in a PET image. Hence, the composite PET signal in a region or pixel includes a small fraction of the plasma signal and a large fraction of the tissue compartments, respectively. The model parameters K_1, \dots, k_6 reflect exchange rates for a labeled ligand moving between the various compartments.

slightly different form, was introduced into the PET literature by Mintun *et al.* (1984).

One of the innovations of the original Mintun formulation was to collapse the nonspecific compartment into the free compartment. Mathematically, this can be justified if the rate constants for nonspecific binding, k_5 and k_6 , are fast relative to the other rate constants of the system. In this case, ligand in the nonspecific compartment is defined as being in rapid equilibrium with the free compartment. If this condition is satisfied, then at any time a fixed fraction of the free plus nonspecific compartment is the effective free pool available for receptor binding. This fraction, f_2 ($= k_6/[k_5 + k_6]$), may not be strictly identifiable (see later discussion) in a receptor-rich region alone, although it may be estimatable from data in a receptor-free region where only two other parameters (K_1 and k_2 , in addition to k_5 and k_6) are needed to describe the data.

1. Output Equation

Because it takes a finite frame time to acquire enough scintillation events to be able to reconstruct a PET image, the measured PET data comprise average numbers of counts over discrete intervals. These intervals need not be (and generally are not) constant. Counts are converted to concentration by way of a calibration. Once the model has been solved for the instantaneous activity in each compartment (F , B , and N), these concentration curves are summed and integrated to generate a theoretical output that is compatible with the measured PET activity over each acquisition time frame, $[t_i, t_{i+1}]$, as follows:

$$\text{PET}[t_i, t_{i+1}] = \frac{1}{\Delta t_i} \int_{t_i}^{t_{i+1}} (\varepsilon_v V + \varepsilon_f F + \varepsilon_b B + \varepsilon_n N) dt \quad (24)$$

⁷Strictly speaking, the plasma is not a compartment of the model. The concentration of tracer in the plasma is measured independently and thus applied to the tissue model as a known input function.

The weights, ε_i , that premultiply each compartment concentration in Eq. (24) are the respective volume fractions. Usually the vascular volume fraction, ε_v is small, and the tissue volume fractions are set at unity or $(1-\varepsilon_v)$. This is indicated schematically in Figure 12: The composite PET signal (enclosed by a dashed-line rectangle) includes a small fraction of the radioactivity in the plasma compartment but a large fraction of the activities in the three tissue compartments. A further subtlety of Eq. (24) is that V refers to the vascular (i.e., whole-blood) contribution to the PET activity. Whereas the plasma concentration is the concentration that must be considered, and modeled as $P(t)$, when considering the driving force for a ligand crossing the blood-brain barrier, the whole-blood activity (a subset of P) is what determines the vascular contribution to the PET signal. We can use numerical methods to solve Eqs. (21)–(23) over time.

A group of simulations of the dynamics in the free, bound, and nonspecific compartments following bolus injection of a generic [^{11}C]-labeled ligand, is shown in the panels of Figure

13. As indicated by the icons at the top of each column, the simulations represent, respectively: two tissue compartments (free and bound) with reversible binding, three tissue compartments (free, bound, nonspecific), and two tissue compartments (free and bound) with irreversible binding. The middle row of simulated data is not decay corrected. Therefore, these represent the type of signal that is actually measured by the PET scanner. The bottom row of simulations certains the decay-corrected concentrations in the compartments for the corresponding uncorrected simulations. The half-life of [^{11}C] is 20.2 minutes, so by 60 minutes almost three half-lives have elapsed. All three simulations are generated from the same plasma input function. Despite the differences in the simulations and in the underlying compartment concentrations, the total radioactivity (not corrected for decay) directly related to what is observed by the PET scanner in each case is nearly the same. In the more realistic case where noise is present, the curves will be even less distinct. The similarity of the uncorrected data for all three model topologies is meant to indicate the potential

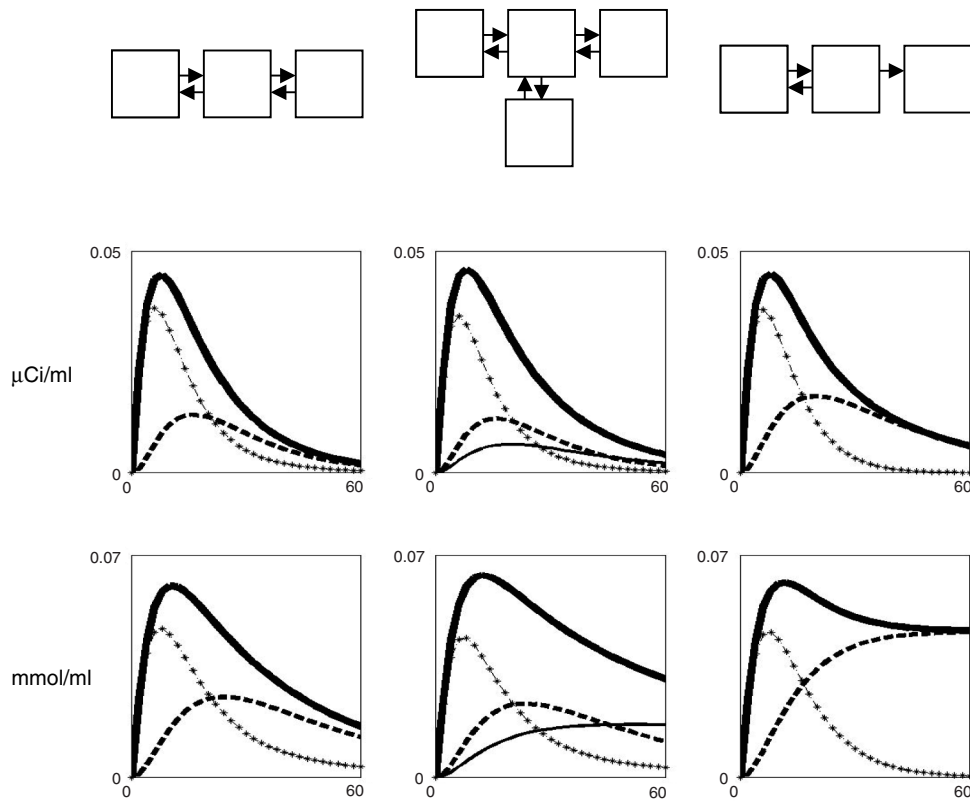


FIGURE 13 Simulations of two- and three-tissue compartment models commonly in use in PET. All simulations were generated with the same plasma input function, $P(t)$, not shown. Top row indicates model topology and number of parameters (indicated by arrows). Middle row shows simulations with radioactive decay (analogous to the signal measured by PET scanner). Bottom row shows respective simulations after correction for radioactive decay. Thin line with symbols (- + + -) is the free concentration; the heavy dashed line (---) is the bound concentration; thin solid line is the nonspecific binding; and heavy solid line is the weighted sum of all radioactivity (i.e., the continuous PET curve). Notice the similarity of the PET curves prior to decay correction despite differences in the simulations. Curves produced with COMKAT (Muzic and Cornelius, 2001).

difficulty of determining *a priori* the correct number of compartments or identifying the model parameters. In fact, the problem of parameter identifiability is seen to be even more difficult than suggested in Figure 13 when one considers that the part of the curve that indicates irreversibility of ligand binding is at the late end of the curve. Unfortunately, because the error in the PET data obeys Poisson statistics (the variance of the data is equal to the mean), these same late-time data with few counts are the least reliable. The issue of parameter identifiability is addressed further later.

2. Measuring the Blood Curve

The input or driving function P represents the amount of tracer ligand that is presented over time to the tissue of interest (i.e., the brain). It is often measured via the radioactivity counted in blood plasma samples drawn from the radial artery. The model given in Eqs. (21)–(24) and diagrammed in Figure 12 deals only with the behavior of a unique tracer molecule, such as [¹¹C]raclopride. The rate constants pertain, specifically, to this molecule. Therefore, if metabolism of the radioligand in the periphery leads to labeled metabolites in the plasma, we must invoke at least one correction and one assumption. First, the nonnative tracer species must be removed either physically from the blood samples or mathematically from the resulting radioactivity counts. Second, it must be assumed that the labeled metabolite(s) does/do not cross the blood–brain barrier (BBB). Thus, one consideration for choosing among candidate tracers may be the generation (or not) of labeled metabolites. In some cases, the production of labeled metabolites may be inevitable. In the case of [¹⁸F]fluorodopa, complicated models have been introduced to account for reentrance of blood-borne metabolite species to the tissue of interest (e.g., the brain) and, in doing so, their contributions to the PET signal (Huang *et al.*, 1991).

B. Modeling Saturability

To this point, we have not introduced any term into the model that reflects the saturable nature of the bound-ligand compartment. That is, we have imposed no explicit upper bound on B . And yet, a unique characteristic of receptor–ligand interactions is that, like enzyme–substrate reactions, they are saturable. The inclusion of an explicit receptor density term, B'_{\max} , requires an elaboration of Eqs. (21) and (22). In Eqs. (25)–(27), we expand k_3 as $k_{\text{on}}(B'_{\max} - B/\text{SA})$:

$$\frac{dF}{dt} = K_1 P - (k_2 + k_5)F - k_{\text{on}}(B'_{\max} - B/\text{SA})F + k_{\text{off}}B + k_6N - \lambda F \quad (25)$$

$$\frac{dB}{dt} = k_{\text{on}}(B'_{\max} - B/\text{SA})F - k_{\text{off}}B - \lambda B \quad (26)$$

$$\frac{dN}{dt} = k_5F - k_6N - \lambda N \quad (27)$$

where k_{off} is equivalent to our previous k_4 ; SA is the specific activity, which declines in time according to the radioactive decay rate, λ ; and k_{on} is the rate constant for a bimolecular association of free ligand and available receptors. Thus, the binding rate is equal to the product of the concentrations of free ligand, F , available receptor sites, $(B'_{\max} - B/\text{SA})$, and rate constant, k_{on} . At the time of injection ($t = 0$), the bound ligand B is zero, therefore B'_{\max} represents the concentration of available receptors in the absence of exogenous ligand. As additional receptors become bound to ligand molecules, the availability of free receptors drops and saturation is approached asymptotically. Because availability can be affected by either labeled or unlabeled ligand, normalization by SA converts B to the concentration of total ligand (i.e., Radioactivity concentration/Radioactivity per moles = Molar concentration). This form of the receptor–ligand model, which was first proposed explicitly by Huang and colleagues (Bahn *et al.*, 1989; Huang and Phelps, 1986; Huang *et al.*, 1989) is analogous to the bimolecular interaction between substrate and available binding sites on an enzyme.

C. Parameter Identifiability: Binding Potential or Other Compound Parameters

Despite the inclusion of an explicit B'_{\max} term in the model representing the baseline level of available receptor sites, this value may not be discernible from the acquired data. In other words, it may not be estimated reliably. Consider that for a single bolus injection of sufficiently high SA ligand, the bimolecular binding term in Eqs. (25) and (26), $k_{\text{on}}(B'_{\max} - B/\text{SA})F$, reduces to $k_{\text{on}}(B'_{\max})F$. That is, $B'_{\max} \gg B/\text{SA}$. Because k_{on} and B'_{\max} always appear as a product, never separately, they are said not to be identifiable and the model defaults to Eqs. (21)–(23). Attempting to estimate both k_{on} and B'_{\max} in this case would be akin to trying to estimate m and n from data with the overparameterized model of a line $y = mnx + b$. Mintun and co-authors make this point in their 1984 paper, saying that k_{on} and B'_{\max} are not separable from a single bolus experiment under tracer (i.e., high SA) conditions. For that reason, they choose to estimate the compound term, B'_{\max}/K_D , which they refer to as *binding potential*; Koeppen *et al.* (1991) recommend further model simplifications when it is not possible even to identify B'_{\max}/K_D , explicitly. Sometimes the data from a receptor–ligand study can be fit to a two-compartment (one-tissue) model (i.e., plasma and free) and inclusion of an explicit bound compartment is not justified. This will be true if the binding and dissociation rate constants for the ligand, k_3 and k_4 , are much faster than the influx and efflux constants, K_1 and k_2 . When this is true, the estimated k_2 will represent an apparent

efflux rate constant, $[k''_2 = k_2/(1 + k_5/k_6 + B'_{\max}/K_D)]$. This parameter, may still reflect the binding potential, as indicated by the B'_{\max}/K_D term, and may be the only reliably estimatable index of binding. Koeppe and colleagues (1991, 1994) have done much work to characterize the kinetics of flumazenil and other muscarinic cholinergic ligands. They point out that quantification is difficult (as with these ligands) if the dissociation rate constant k_{off} is slow and cannot be reliably distinguished from zero. Conversely, quantification of these ligands' binding rate constants is difficult and highly sensitive to changes in blood flow when binding is very rapid relative to the rates of transport across the BBB (i.e., K_1 and k_2) (Zubieta *et al.*, 1998).

There are many instances in research when binding potential (BP) is a satisfactory indicator of (available) receptor level. In these cases, BP, reported in table form by brain region or as a parametric map, is a reasonable end point for a functional imaging study. There have been a number of studies that monitor change in apparent BP as an indicator of change in the level of an endogenous competitor to the injected ligand (see discussion of neurotransmitter activation studies in Sections IV D and VII). A number of easy and robust methods for calculating this parameter are discussed here. However, implicit in the adoption of BP as a surrogate B'_{\max} is the assumption that the affinity, K_D , of the ligand for the receptor is constant across subjects or treatments. For those cases in which changes in affinity cannot be ruled out or where some other mechanistic question is at stake, more than a single bolus injection is indicated. Delforge *et al.* (1989, 1990) proposed an experimental protocol involving three sequential bolus injections of varying specific activities. At least one of those injections also contains a nontrace amount of cold (i.e., unlabeled) ligand. In such a protocol, the number of available receptors is significantly perturbed, and it is this process of modulating availability over a broad range of values that serves to decorrelate k_{on} from B'_{\max} . Delforge and co-authors show via experiments and simulations that it was possible to estimate unambiguously seven model parameters (including k_{on} , B'_{\max} , and k_{off}) using a three-injection protocol. Thus, the individual parameters are said to be identifiable. An example of the data from a multiple-injection protocol, in which $[^{11}\text{C}]\text{-CFT}$ (a dopamine transporter ligand) was administered to a rhesus monkey, is given in Figure 14. The authors of the study (Morris, Babich, *et al.*, 1996) were able to estimate five parameters simultaneously (nonspecific binding parameters k_5 and k_6 had to be fixed based on cerebellum data). In designing experiments, one must beware that protocols that rely on nontrace doses of ligand may not be feasible in psychiatric patients—particularly children—because the large mass doses of ligand are likely to have pharmacological effects.

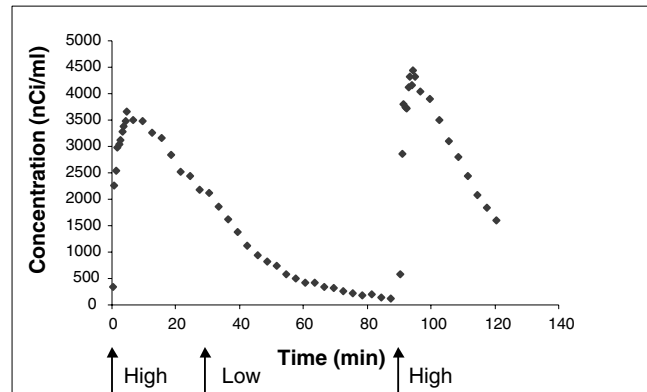


FIGURE 14 Dynamic PET activity from region drawn on striatum of rhesus monkey. Three-injection protocol used is described in Morris, Babich, *et al.* (1996a). Injections of $[^{11}\text{C}]\text{-CFT}$ were made at 0, 30, and 90 minutes (indicated by arrows). Second injection was low specific activity causing net displacement of labeled ligand from receptor by unlabeled ligand. Notice the difference in responses after the first and second high-specific-activity injections because of the presence of residual cold ligand on board. Data are not decay-corrected.

1. Modeling Multiple-Injection Data—Two Parallel Models

To analyze data from their multiple-injection experiments, Delforge and colleagues (1989, 1990) proposed a further modification of the three-compartment model. Because these protocols depend on at least one nontrace⁸ injection of ligand, the researchers propose parallel models for the labeled and unlabeled species. The model can be described as follows.

$$\frac{dF^j}{dt} = K_1 P^j - (k_2 + k_5) F^j - (k_{\text{on}}/V_R)(B'_{\max} - B^h - B^c) F^j + k_{\text{off}} B^j + k_6 N^j - \lambda^j F^j \quad (28)$$

$$\frac{dB^j}{dt} = (k_{\text{on}}/V_R)(B'_{\max} - B^h - B^c) F^j - k_{\text{off}} B^j - \lambda^j B^j \quad (29)$$

$$\frac{dN^j}{dt} = k_5 F^j - k_6 N^j - \lambda^j N^j \quad (30)$$

where the superscript j refers to either hot ($j = h$) or cold ($j = c$) ligand, and λ^j is the radioactive decay constant for the isotope when j refers to the hot ligand and 0 when j refers to cold (i.e., there is no radiodecay of cold ligand.)

The Delforge nomenclature employs the compound term k_{on}/V_R as the apparent association rate constant. V_R is the volume of reaction of the receptor but k_{on}/V_R is treated as one indivisible parameter. If the microenvironment surrounding the receptor is unusually inaccessible to the ligand, the apparent binding rate will differ from the true binding rate (see Delforge *et al.*, 1996 for a thorough discussion of the reaction-volume concept). In practice, the number of estimable

⁸Nontrace here means an amount great enough to have visible biological or pharmacological effects, that is, not insignificant, biologically.

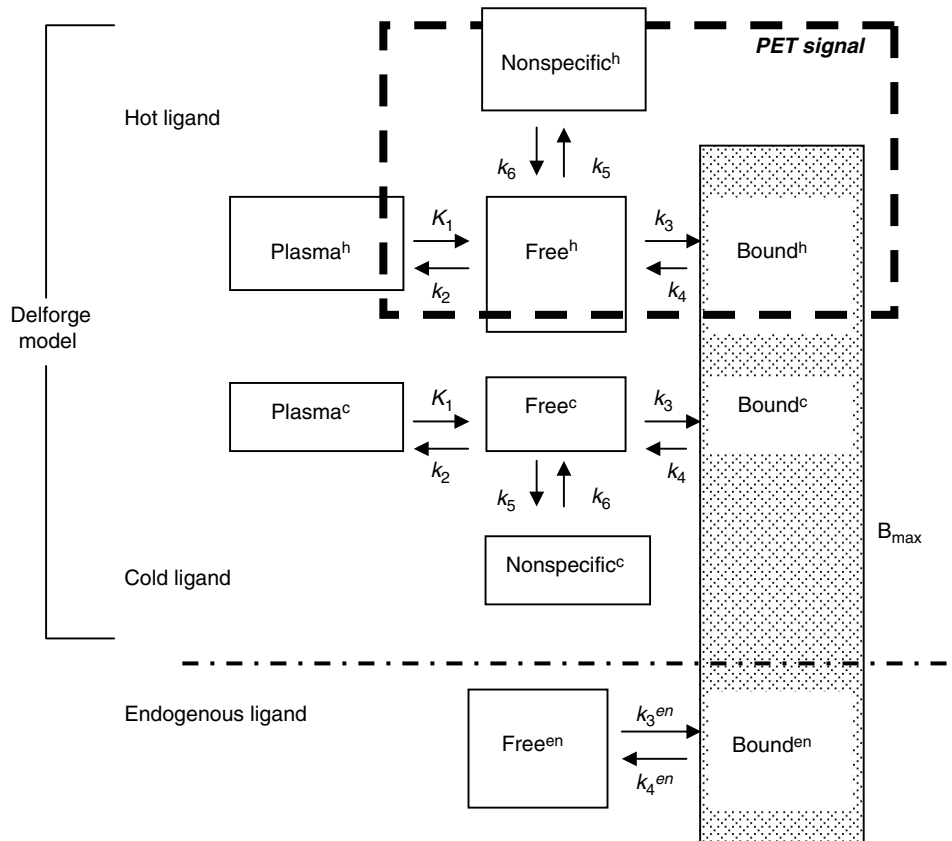


FIGURE 15 Schematic corresponding to model Eqs. (28)–(31). Notice that the fixed number B_{\max} , the total population of possible ligand binding sites available to hot, cold, or endogenous ligand, is the vehicle by which the three parallel models are coupled. That is, the term B_{\max} , more specifically $(B_{\max} - B - B^{\text{en}} - B^{\text{c}})$, appears in the mass balances for each of the Free and Bound compartments.

parameters in the model is seven. (From a parameter estimation standpoint, k_{on}/V_R is no different from the k_{on} term introduced in earlier equations.) No new parameters have been added to the model given earlier (Eqs. 24–26) because the hot and cold ligands are identical, biologically. In essence, the Delforge model is two models joined at the hip. One model is for the cold species and one is for the hot (i.e., labeled). The two models are coupled by the bimolecular binding term that occurs in both. The model of Eqs. (28–30) is diagrammed as the top two-thirds of Figure 15 (i.e., everything associated with hot and cold ligand.)

There is an additional experimental burden in performing multiple-injection experiments. Two plasma input functions must be measured. The first, P^h , is the standard curve of radioactivity in the plasma, P , that has been mentioned previously. The other, P^c , is the concentration (in pmol/ml) of cold ligand in the plasma. Because this is not readily measurable during the experiment, it must be reconstructed from the available plasma radioactivity measurements and knowledge of the specific activities of each injection. (See Morris, Babich, et al., 1996, App.). Despite its greater complexity, the Delforge approach maximizes the number

of model parameters that can be properly identified (Morris, Alpert, et al, 1996). The identifiability of parameters is closely tied to the concept of sensitivity coefficients. For a parameter from a given model to be identifiable from experimental data, the derivatives of the objective function (which is being minimized when fitting data) with respect to the different parameters must be linearly independent, that is, distinct. In other words, each parameter must contribute something distinct to the model curve. If a change in one parameter can be confused as a change in another parameter (as could be the case in the simulations of Figure 13) then it will not be possible to uniquely identify all the parameters. The strength of the Delforge approach, on a theoretical level, is that it perturbs the system so that we observe it at multiple set points. Figure 16 is a simulation of the Delforge model shown schematically as the top two-thirds of Figure 15. Notice that the (hot) bound compartment concentration reaches a peak after the first high-specific-activity injection at time 0, but cannot reach the same peak after the second injection of low SA material has caused a significant number of receptor sites to be bound to cold exogenous ligand.

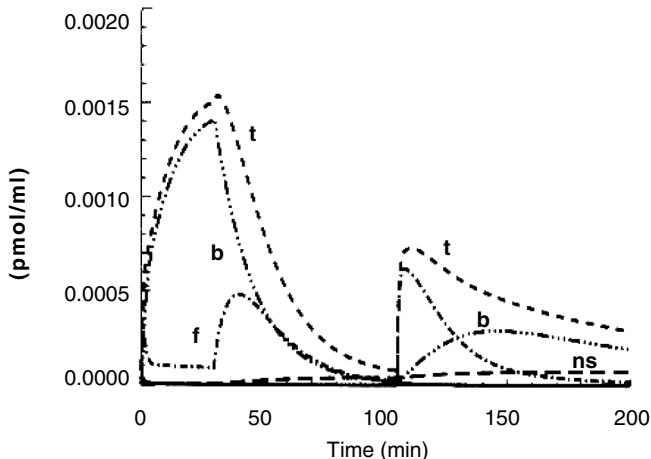


FIGURE 16 Simulation using the model shown in Figure 15 of the compartmental (*f* = free, *b* = bound, *ns* = nonspecific, and *t* = total tissue) concentrations of radioligand during a three-injection experiment. Such simulations are able to fit the type of data shown in Figure 15 with an identifiable set of model parameters. In this simulation, the injections are at 0, 30, and 100 minutes. The response to high-specific-activity injections at 0 and 100 min are different because of the presence of residual cold ligand from the injection of low-specific-activity ligand at 30 minutes. See Morris, Alpert, *et al.* (1996).

In fitting this data, which is more information-rich than those from a single-injection experiment, the different influences of each parameter on the model become apparent. For a discussion of the multiple-injection approach, sensitivity coefficients and why the multiple-injection approach works in some cases (See Morris, Bonab *et al.*, 1999). Unfortunately, the multiple-injection approach is experimentally and logically much more complicated than a single-bolus study. Nevertheless, this complexity might be justified in the preliminary development and exploration of a new ligand when precise estimates of all parameters are needed. The parameter estimates resulting from such a multiple-injection study would then be used to develop and analyze a simpler clinical protocol.

D. Neurotransmitter Changes—Nonconstant Coefficients

Each of the foregoing models, regardless of complexity, is founded on some common assumptions. One is that the model parameters are constant over the duration of the experiment. This is a reasonable assumption if the system itself is at steady state. Whereas [¹¹C]-raclopride levels may rise and fall as it is taken up and eliminated from the tissue following a bolus injection, dopamine levels remain unchanged over the time scale of interest. The rate constants that are determined by the overall state of the system remain unchanged. Anything that violates these assumptions may invalidate the use of the constant-coefficient models given earlier and must be investigated. For example,

the consequences of unwanted changes in blood flow and their impact on the estimation of raclopride binding have been investigated using both simulations (Frost *et al.*, 1989; Logan *et al.*, 1994; Laruelle *et al.*, 1994) and an experimental perturbation—hyperventilation (Logan *et al.*, 1994). In the hyperventilation study, Logan *et al.* (1994) find that the compound parameter, distribution volume ratio (see Section VC), was insensitive to absolute flow level and thus was perhaps a more robust parameter than individual rate constants (e.g., *k*₃, *k*₄, or *k*_{on}). In 1991, Logan and colleagues explored the consequences of changes in dopamine on the measurement of binding parameters of a D2 receptor ligand, methylspiroperidol.

There has been growing interest in detecting and quantifying transient changes in neurotransmitter concentrations that may be useful for understanding the etiology of neuropsychiatric diseases (see Laruelle *et al.*, 1996; Breier *et al.*, 1997 for evidence that schizophrenia is associated with abnormal amphetamine-induced dopamine release). The potential for such a measurement exists because the endogenous ligand (e.g., dopamine) competes with the exogenous ligand for binding to available receptor sites. Any alteration in the steady-state level of this ever-present competition could alter the PET signal. To model a system in which the neurotransmitter concentration is not constant, we must again extend the models developed here. Just as the Delforge model (Eqs. 28–30) extended its antecedents by adding terms for labeled and unlabeled exogenous ligand species, the changing neurotransmitter model must add terms for the endogenous ligand species. Morris and co-workers (1995) introduce a differential equation into the receptor-ligand model to describe the binding and release of endogenous species from the receptor:

$$\frac{dB^{\text{en}}}{dt} = \left(k_{\text{on}}^{\text{en}} / V_R^{\text{en}} \right) (B_{\max} - B^{\text{h}} - B^{\text{c}} - B^{\text{en}}) F^{\text{en}} - k_{\text{off}}^{\text{en}} B^{\text{en}} \quad (31)$$

where the superscript en refers to the endogenous species. Note that *B*_{max} is the concentration of *all* the receptor sites (available and not) and the bimolecular binding terms for the other species (hot and cold tracer ligand) must be modified accordingly. *F*^{en} is a time-varying concentration of endogenous chemical available for binding to the receptor. *k*_{on}^{en}/*V*_R^{en} is the apparent binding rate constant for the endogenous ligand. Equation (31) can be solved simultaneously with the multiple-species system of Eqs. (28)–(30). A similar approach is taken by Endres and colleagues (1997), who retain the format of Eqs. (21)–(23) but introduce a time-varying binding rate parameter:

$$k_3 = k_{\text{on}} B_{\text{free}}(t)$$

where *B*_{free}(*t*) is *B*_{max} − *B*^h − *B*^c − *B*^{en}. *B*_{max} is still constant, but *B*^h, *B*^c, and *B*^{en} can all vary with time. This enhanced model (as described by Eqs. 28–31) is diagrammed by the entire network of compartments in Figure 15.

There have been two experimental approaches to the problem of quantifying neurotransmitter changes.⁹ The first is a natural extension of the studies already mentioned. It is based on the comparison of PET signals from two bolus injections of radiotracer. One bolus study is performed while neurotransmitter is at steady state; a second bolus study is carried out while endogenous neurotransmitter is undergoing an induced change. The alternative experimental approach also involves a perturbation of the neurotransmitter but it is done only after the radiotracer has been brought to a steady state in the tissue by a combination of bolus plus infusion administrations. Let us look briefly at this steady-state method.

1. Steady-State Technique

The bolus-plus-infusion method was developed for receptor-ligand characterization studies by Carson and colleagues at the National Institutes of Health (Kawai *et al.*, 1991; Carson *et al.*, 1993). The beauty of this method is that by properly combining a bolus with a constant infusion of radiotracer, the radiotracer level in the brain can be brought to a constant level in a minimum of time. With ligand levels in the tissue no longer varying in time, the derivatives on the left-hand sides of Eqs. (21)–(23) disappear and the models reduce to a set of algebraic equations. In fact, no modeling is required. For many ligands this technique is ideal for reliably estimating distribution volume (which is a linear function of binding potential). The steady-state method has been used quite extensively in SPECT studies (Laruelle *et al.*, 1994), which, because of long-lived isotopes, can be applied to data acquired the day following a bolus injection (no infusion needed). The bolus-plus-infusion method is easily extended to neurotransmitter change experiments by perturbing the endogenous neurotransmitter pharmacologically once the steady state level of radiotracer has been achieved. The measured parameter that has been used to indicate neurotransmitter alteration is the change in binding potential, ΔBP . Figure 17 shows a change in steady-state level of raclopride activity in the striatum of a monkey before and after amphetamine perturbation. The activity in the cerebellum (devoid of D2 receptors) is unaffected (Endres *et al.*, 1997).

2. Experimental Considerations

Whether one chooses the two-bolus or the constant infusion approach, there are two important questions to be answered: (1) Can the change in PET signal be reliably detected given the inherent variability in the method? (2) Can

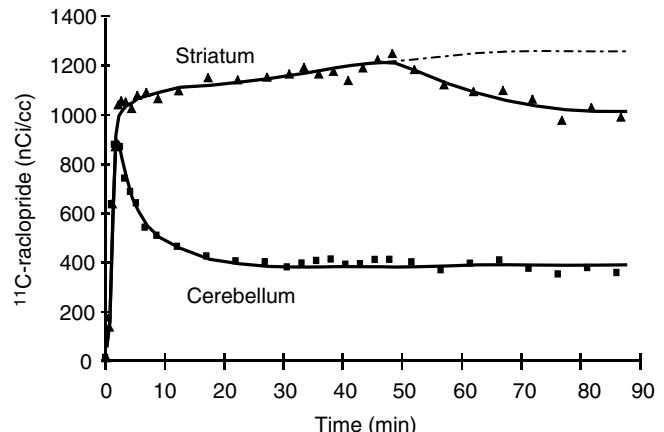


FIGURE 17 Bolus-plus-infusion method for detecting changes in neurotransmitter level. Amphetamine-induced perturbation of raclopride binding at 45 min. Top curve shows depression in [11C]-raclopride signal in striatum following heightened competition between raclopride and dopamine for binding at D2 receptors. Perturbation was 0.4 mg/kg injection of amphetamine given to rhesus monkey. Bottom curve shows no effect of dopamine modulation on cerebellum. Dotted continuation of top curve shows model-predicted continuation of curve absent amphetamine injection. Data are decay-corrected. (Data from Endres *et al.*, 1997.)

the apparent change in some parameter of interest be unambiguously linked to changes in neurotransmitter, given the inherent variability and covariability of the parameters? With regard to question 1, Endres *et al.* (1997) use simulations to show that in the case of the bolus-plus-infusion technique, ΔBP is proportional to the integral of the endogenous neurotransmitter curve (i.e., the additional amount of neurotransmitter, released transiently, above the steady-state level). Morris and Fisher and colleagues at Massachusetts General Hospital (Morris *et al.*, 1995; Fisher *et al.*, 1995) show that with the two-bolus method the sum of squares difference (X^2) between the two dynamic PET curves (with and without perturbation) increases with duration of perturbation. More recently, Aston *et al.* (2000) adopted a hybrid approach of modeling and statistical tests to analyze the two-bolus data to arrive at pixel-by-pixel maps of BP for each of the two dynamic studies. They then used paired *t*-tests to make a neurotransmitter activation map of those pixels whose BP was statistically different in rest and activated conditions. More important, the effect of transient neurotransmitter release is distinct from a transient increase in blood flow, and the precise timing of the perturbation relative to the tracer bolus can greatly affect the magnitude of the signal change. Endres *et al.* (1998) provide a mathematical formalism for understanding the importance of perturbation timing and its relation to the kinetics of the labeled ligand. The bolus-plus-infusion method depends on measuring BP at steady state in two conditions. If steady state is not reached in the pre- or postperturbation phase, the reliability of the measurements will be affected. The striatal (top) curve in Figure 17 may not

⁹An approach intermediate between those discussed here has been proposed by Friston *et al.* (1997). A single-bolus study is performed and any statistically significant deviation in time from the predicted dynamic curve is a measure of activation, in effect detecting a change in k_2 . A pharmacological challenge was used as a test case.

have quite come to equilibrium when the amphetamine was administered. The time required to reach steady state can be minimized by shifting the fraction of tracer delivered in the bolus versus that delivered via infusion (Carson *et al.*, 1993). Along the same lines, one can optimize the precision of the measured parameter, ΔBP , by appropriately choosing the best range of times for calculating BP_{pre} and BP_{post} with the least amounts of noise. When a uniform optimal protocol used for measuring ΔBP was applied retrospectively to data acquired by Breier *et al.* (1997), the significance of the difference between the dopamine responses of schizophrenics and controls to amphetamine was improved ($p < 0.038$ to $p < 0.012$) (see Watabe *et al.*, 2000). The implications of the various techniques for imaging neurotransmitter change and some applications are examined in Section VII of this chapter.

E. Neurotransmitter Levels

Delforge *et al.* (2001) have proposed a possible scheme for measuring the steady-state level of endogenous neurotransmitter. They first observe that in many analyses of receptor-ligand data there is an unwanted correlation between receptor density B'_{max} and affinity K_D/V_R (in their terminology). The researchers interpret this correlation (or bias in K_D/V_R) as a deficiency in the compartmental model. The deficiency, they claim, is an ignored effect of endogenous neurotransmitter. They then model the bias in estimated K_D/V_R as first order in endogenous neurotransmitter concentration (K_D/V_R measured = K_D/V_r , true + [Endogenous ligand concentration]*Correlation). This putative linear relationship involving the concentration of endogenous ligand can then be expressed in terms of its effect on occupied receptor sites through the *a priori* knowledge (i.e., a guess) of the K_D of endogenous ligand and the assumption that the endogenous ligand is in fast equilibrium between the free and receptor-bound states. The upshot is an equation for the steady-state occupancy of receptors by endogenous ligand:

$$\frac{B^{\text{en}}}{B_{\text{max}}} = \frac{\text{const} \times B'_{\text{max}}}{1 + \text{const} \times B'_{\text{max}}} \quad (32)$$

The paper is commended to the reader for further study with the following caveat: Equation (32) predicts that in the limit as the density of receptors goes to a very large number, the fraction occupied at steady state will be 1.

V. MODEL SIMPLIFICATIONS

A. Reference Region Methods

The arterial plasma time activity curve serves as the input function to the compartmental model that is used for parameter estimation (see Eq. 21). Often represented as a

compartment in itself, $P(t)$ is multiplied by the rate constant K_1 , and represents the delivery of the radiotracer from the arterial plasma to the tissue space. The radioconcentration of the plasma is typically sampled from the radial artery and assumed to be representative of the plasma concentration presented to the brain tissue.

Although $P(t)$ is often needed to drive a particular kinetic model, there are many burdens that accompany the acquisition of an arterial plasma input function. These include discomfort to the patient, increased risk of transferring a blood-borne disease (particularly with animal studies), and the need for additional personnel and equipment in withdrawing and assaying the plasma samples. For these reasons, there is considerable motivation for developing an analysis scheme that does not require sampling arterial plasma. This can frequently be accomplished through the use of radioactivity concentration measurements in a region of tissue that has negligible specific binding, called a reference region. Reference region models rely on two key devices: (1) the model of a receptor-rich region can be expressed in terms of the model of a reference region, and (2) the values for distribution volume (DV) in different regions can be constrained.

As shown in the standard compartmental model configuration (Eqs. 21–24), the movement of the radiotracer to and from the tissue is described by the rate constants K_1 and k_2 . The ratio of these two parameters, K_1/k_2 , represents the distribution volume, DV. By assuming DV to be constant across the regions of the brain, several simplifications can be made to the functional equations introduced in Section IV. The $P(t)$ term can be replaced in the model equations by using the radiotracer kinetics from an alternate region. This section presents several reference region models that have been validated against the standard compartmental analysis (i.e., including an arterial input function).

B. Compartmental Model Simplifications

Cunningham and co-workers (1991) proposed solving for the arterial input function in terms of the derivatives of a reference region and substituting this value into the equations for the regions with specific binding. They start with the state equation for a reference region (Eq. 21 for a region with no explicit B or N term) and solve for the plasma function:

$$P(t) = \frac{1}{K_1^R} \left(\frac{dF_R}{dt} + k_2^R F_R \right) \quad (33)$$

Assume that $P(t)$ is the same in reference region as in the receptor-rich regions and substitute:

$$\frac{dF}{dt} = \frac{K_1}{K_1^R} \left(\frac{dF_R}{dt} + k_2^R F_R \right) - (k_2 + k_3) F + k_4 B \quad (34)$$

$$\frac{dB}{dt} = k_3 F - k_4 B \quad (35)$$

where F_R , F , and B represent the radioligand concentrations in the reference, free, and specifically bound regions, respectively. Although Eqs. (34) and (35) may look formidable, they are easily solved. Recall that once measurements have been taken in the designated reference region over time, F_R is merely a measured array of values and dF_R/dt can be calculated directly. A constraint is placed on this system that requires the free space distribution of the radioligand be equal in the reference and receptor-rich regions, that is, $K_1^R/k_2^R = K_1/k_2$. This model still allows for blood flow differences between regions by constraining only the ratio of K_1 to k_2 and not the individual parameters. With these substitutions, four parameters, $R_I (= K_1/K_1^R)$, k_2 , k_3 , and k_4 , can be estimated iteratively. This model was originally applied to [³H]-diprenorphine (Cunningham et al., 1991) and later modified for use with PET and [¹¹C]-raclopride in rats (Hume et al., 1992) and humans (Lammertsma et al., 1996).

Not all reference regions are ideal; that is, they may contain some receptor sites of interest. In such cases modifications can also be made to the reference region model to account for specific binding in the reference region (Cunningham et al., 1991). By assuming that the specific binding rate constants k_{on} and k_{off} are uniform across regions and by having prior knowledge of B'_{max} in the reference region, it is possible to calculate the binding constants for a region of interest. A summary of assumptions and other requirements inherent in each reference region model are summarized in Table 1.

The work of Gunn et al. (1997) extends the Cunningham model in an effort to further simplify the experimental analysis and generate voxel-by-voxel parametric images of several select rate constants. Gunn and colleagues define a set of basis functions that are linear in the parameter estimates in order to calculate a linear least squares solution. With this method, the time-dependent tissue concentration is described by:

$$C_t(t) = \theta_1 F_R(t) + \theta_2 B_i(t),$$

where $B_i(t) = F_R(t) \otimes e^{-\theta_3(BP)t}$ and θ_i are linear combinations of the parameter estimates. For this case, the number of estimated parameters is reduced to three: R_I , k_2 , and BP ($= k_3/k_4$).

C. Logan Analysis

The method of Logan (1990) was initially developed to provide a technique for rapid data analysis. It implements an analytic solution that can be solved noniteratively to generate a parametric image of binding potentials. The original formulation was based on the multiple-time graphical method of Patlak et al. (1983). Like the Patlak technique (discussed in Section III), it does not assume a particular kinetic model in the calculation of the distribution volume. Using matrix notation, the kinetics of radiotracers in a reversible compartment can be formulated as (Hearon 1963):

$$\frac{d\mathbf{A}}{dt} = \mathbf{KA} + \mathbf{QP}(t), \quad (36)$$

where \mathbf{A} is a vector of the amount of radioactivity of radioligand in each reversible compartment, matrix \mathbf{K}

TABLE 1 Assumptions for Using a Reference Region^a

Method/Author	Model Dependence	DV _{F+NS}	A priori Information
Cunningham et al. (1991)	Assumes a two-tissue compartment model for the target region and either a one- or two-compartment model for the reference region	Assumes K_1/k_2' is constant across regions	
Logan et al. (1990, 1996) DV and DVR	Not dependent on a particular model structure	DVR in itself does not require DV _{F+NS} to be constant across regions; this assumption is enforced to translate it into BP	Requires <i>a priori</i> knowledge of a population average k_2 term for one of the methods and time of linearity for both.
Ichise et al. (1996)	Not dependent on particular model structure	Does not require constant ratio of target to reference activities to relate DVR to BP	Does not require mean k_2 .
Lammertsma et al. (1996); Gunn et al. (1997)	Assumes that the target region can be adequately fit to a single-tissue compartment (or assumes the exchange between free and specifically bound regions is sufficiently rapid, which is not really the case for raclopride)	Assumes K_1/k_2' is constant across regions	

^aAll models assume a region exists that has negligible specific binding.

contains the intercompartment rate constants, and \mathbf{Q} is a vector of the rate constants designating transport from the plasma to the exchangeable compartments. In applying this equation to PET data, it is assumed that the PET activity measured in a reconstructed volume consists of a sum of the three compartment states ($F + B + N$). Note that the contribution of the plasma radioactivity P is neglected. For this case, Eq. (36) can be expressed as:

$$\begin{bmatrix} \frac{dF}{dt} \\ \frac{dB}{dt} \\ \frac{dN}{dt} \end{bmatrix} = \begin{bmatrix} -(k_2 + k_3 + k_5) & k_4 & k_6 \\ k_3 & -k_4 & 0 \\ k_5 & 0 & -k_6 \end{bmatrix} \begin{bmatrix} F \\ B \\ N \end{bmatrix} + \begin{bmatrix} K_1 \\ 0 \\ 0 \end{bmatrix} P(t) \quad (37)$$

After integrating, premultiplying by the inverse of the \mathbf{K} matrix, and premultiplying by the summing vector $[1 \ 1 \ 1]$, the integral of the PET activity is given by:

$$\int_0^T PET(t) dt = \int_0^T (F + B + N) dt = -[1 \ 1 \ 1] \mathbf{K}^{-1} \mathbf{Q} \int_0^T P(t) dt + [1 \ 1 \ 1] \mathbf{K}^{-1} \mathbf{A} \quad (38)$$

Additional algebraic manipulation yields a linear equation with a slope and an intercept:

$$\frac{\int_0^T PET(t) dt}{PET(T)} = \text{Slope} \frac{\int_0^T P(t) dt}{PET(T)} + \text{Const} \quad (39)$$

where Slope = $-[1 \ 1 \ 1] \mathbf{K}^{-1} \mathbf{Q} = DV$, and DV is the distribution volume, $(K_1/k'_2)(1 + k'_3/k_4)$, for the case where nonspecific binding is not modeled explicitly.

Typically, the nonspecific binding (N) is assumed to be rapid with respect to the transport and specific binding, and its effect can be incorporated into apparent model parameters of a reduced model. Thus, the rate constants are now represented as composite parameters, $k'_2 = k_2(1 + k_5/k_6)^{-1}$ and $k'_3 = k_3(1 + k_5/k_6)^{-1}$ (Koepp et al., 1994). As a practical matter, the relative rapidity of nonspecific binding often renders k_5 and k_6 unidentifiable, and as a result k'_2 is the only accessible parameter. Unfortunately, it is often improperly referred to simply as k_2 in the literature.

1. Logan Analysis with Reference Regions

It is also possible to manipulate Eq. 36 to eliminate the plasma-dependent term and replace it with the kinetics of a reference region (Logan et al., 1996). This formulation leads nicely to images of DVR (= BP + 1) at each pixel, as can be seen in Figure 18. The functional equation then takes the form:

$$\frac{\int_0^T C_t(t) dt}{C_t(T)} = DVR \frac{\int_0^T F_R(t) dt + [F_R(T)/\bar{k}_2]}{C_t(T)} + b' \quad (40)$$

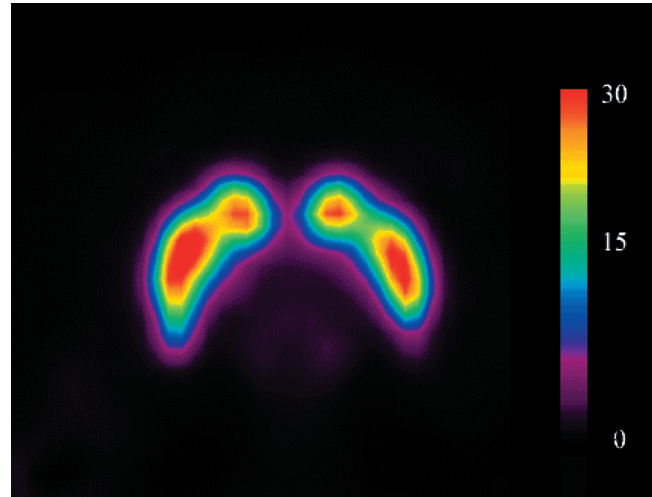


FIGURE 18 A DVR parametric image of [F-18]-fallypride binding in the brain of rhesus monkey. Each voxel in this image represents a calculation of DVR as given in Eq. 40. [F-18]-fallypride is a highly selective dopamine D2 antagonist that binds to the D2 receptor-rich regions of the brain, as seen by the high uptake in the striatal regions (caudate and putamen) and lower uptake in the thalamus (below the striatum). (For details see Christian et al., 2000.)

where $C_t(t)$ is the PET-measured concentration of the radioligand in the tissue, $F_R(t)$ has been defined as the PET concentration in the reference tissue, DVR is defined as the distribution volume ratio, \bar{k}_2 is the regional average of k_2 , and b' is a constant of integration. For reversible ligands, a time will be reached when the function becomes linear. This time is dependent on the individual rate constants of a radioligand. The slope of the resultant line represents the ratio of the distribution volumes of the target to reference region DVR. In the case of the three-compartment model (Eq. 37), DVR is equal to:

$$\frac{K_1}{\bar{k}'_2} \left(1 + \frac{k'_3}{k_4} \right) \frac{K^R}{k'^R}$$

If the free plus nonspecific distribution volumes ($DV_{F+NS} = K_1/k'_2$) are constant across regions, then the distribution volume ratio simplifies to:

$$DVR = 1 + \frac{k'_3}{k_4} = 1 + f_{NS} \frac{B'_{max}}{K_D}$$

where $f_{NS} = 1/(1 + k_5/k_6)$ (Logan et al., 1994). This simplification is noteworthy because it leads directly to the nearly ubiquitous use of Logan plots as a noniterative means of calculating some rather robust parameters that are proportional to B'_{max} . So we have what we wanted all along—a method of analysis that is easy to apply and apparently yields an estimate of something akin to B'_{max} . But are there drawbacks to this seemingly simple and popular method?

D. Limitations and Biases of the Reference Region Methods

The first step in applying a reference region method of analysis is to validate it against a gold standard. In general, the gold standard for PET radioligand studies is a two-tissue compartment kinetic model with measured arterial plasma as the input function. Knowledge of the individual parameter estimates can then be used to test the biases introduced by the simplifying assumptions of the reference region methods. For example, one of the assumptions of the simplified reference region method (Gunn *et al.*, 1997) is that the equilibration between the free and bound space be rapid, as is the case with many PET radioligands. However, for those radioligands with moderately nonstandard kinetics, a significant bias in the calculation of BP is seen if the rapid equilibration assumption is violated (Alpert *et al.*, 2000). For an example, see Figure 19.

Similarly, preliminary validation is needed when using the Logan DVR method (Eq. 40) to determine the mean k_2 parameter and to provide an estimate of when linearity is achieved. It is impractical to have an *a priori* estimate of the population average value for k_2 , so the second method introduced by Logan *et al.* (1996) is more common and is valid as long as the regrouped term on the right-hand side of Eq. (41) is a constant:

$$\frac{\int_0^T C_t(t)dt}{C_t(T)} = \text{DVR} \frac{\int_0^T F_R(t)dt}{C_t(T)} + \left[\frac{F_R(T)}{\bar{k}_2} + b' \right] \quad (41)$$

If $F_R(T)/C_t(T)$ is a constant, then Eq. (41) will be a line after some time, as previously discussed. In this case, an average k_2 is not required. Ichise *et al.* (1996, 2001) recognized

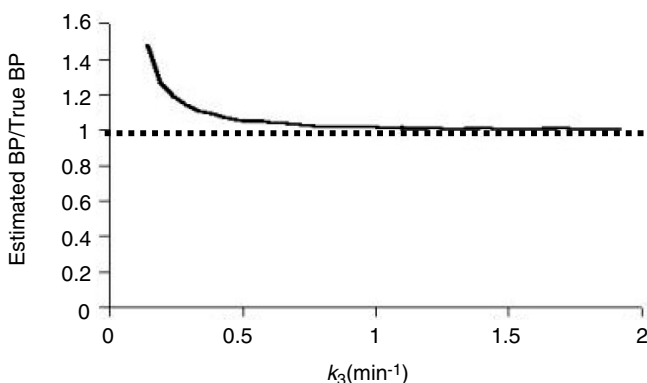


FIGURE 19 Bias in binding potential as estimated by simplified reference region technique. Estimates are based on simulated data. Ratio of estimated to true BP is plotted on y-axis versus true k_3 . As k_3 (1/min) becomes smaller, rapid equilibration between free and bound compartments—a necessary assumption of the method—is violated. (Figure supplied courtesy of Dr. N. M. Alpert. See Alpert *et al.* 2000).

that instead of requiring the term $F_R(T)/C_t(T)$ to become a constant, one could merely treat it as another independent variable in a multiple linear regression scheme. Doing so eliminates the need for an average k_2 and the requirement that $F_R(T)/C_t(T)$ be constant. This approach may eliminate some contributors to bias in the estimates of DVR that are introduced if the condition of constant ratio of tissue activities is never truly achieved.

An illustration of DVR for three D2 receptor antagonists with varying affinities is shown in Figure 20. It has also been demonstrated that the measurement of DVR is biased in the presence of statistical noise (Hsu *et al.*, 1997), which can be quite significant in PET imaging studies. This bias is in part a result of nonindependence of the observations used in the Logan plots. That is, integral quantities of the radioactivity in the target region are plotted on the y axis and integral quantities of the activity in the blood or reference tissue are plotted on the x axis. Each of the y values (and similarly, each of the x values) are thus correlated with each other. This correlation has a biased effect on the estimate of slope (DV or DVR) (see Slifstein and Laruelle, 2000). However, it has been shown that the bias in DVR can be minimized by using smoothing techniques (Logan 2000; Logan *et al.*, 2001).

E. Practical Use

The use of a reference region method of analysis is an intermediate step in the process of shepherding a newly developed radioligand from validation to application stage. When using PET for *in vivo* hypothesis testing, the absolutely simplest form of analysis is to compare radioactivity in different regions on a single static PET image. Obviously such a method eliminates the need for the invasive arterial input measurement and the time-consuming dynamic PET scan. Unfortunately, simple ratio methods can be fraught with bias and variability (Hoekstra *et al.*, 1999). Although the use of a reference region falls short of eliminating the need for dynamic data, it is often the optimal choice in the compromise between simplicity and accuracy.

VI. LIMITATIONS TO ABSOLUTE QUANTIFICATION

Model-based data analyses typically assume that tissue radioactivity is accurately measured in absolute units (i.e., $\mu\text{Ci}/\text{ml}$). In reality, it is not so simple. Attenuation of radiation by tissue, scatter, randoms, dead time, and spatial resolution effects all degrade the accuracy of PET. For the most part, image reconstruction software provided by the PET scanner manufacturer provides the means to correct for all

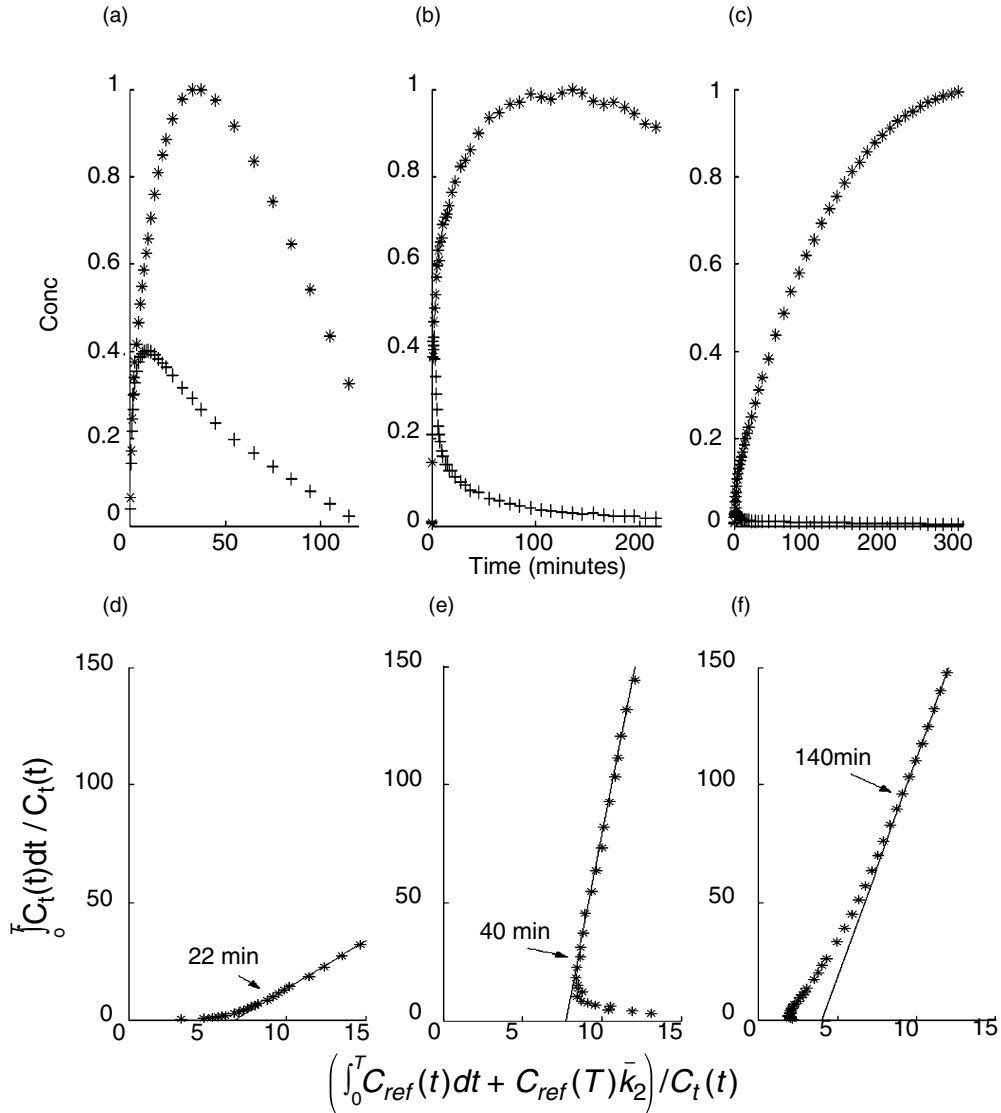


FIGURE 20 Simulated time activity curves and Logan DVR plots of three different D2 receptor antagonists with varying receptor affinities and kinetics in the striatum (*) and the cerebellum (+). **(a)** $[^{11}\text{C}]\text{-Raclopride}$, moderate D2 affinity (for simulation: $k_3 = 0.33 \text{ min}^{-1}$, $k_4 = 0.11 \text{ min}^{-1}$). **(b)** $[^{18}\text{F}]\text{-Fallypride}$, high affinity (for simulation: $k_3 = 1.16 \text{ min}^{-1}$, $k_4 = 0.04 \text{ min}^{-1}$). **(c)** $[^{76}\text{Br}]\text{-FLB 457}$, high affinity (for simulation: $k_3 = 2.91 \text{ min}^{-1}$, $k_4 = 0.02 \text{ min}^{-1}$) for the D2 site. **(d,e,f)** Logan DVR plots for the corresponding radioligands; $[^{11}\text{C}]\text{-Raclopride}$ with a rapid linearization occurring at approximately 22 minutes, $[^{18}\text{F}]\text{-allypride}$ with a moderate linearization time of 40 minutes, and $[^{76}\text{Br}]\text{-FLB 457}$ taking a long time for linearization of approximately 140 minutes.

but the spatial resolution effects. Consequently, we discuss only spatial resolution effects here.

Spatial resolution effects are sometimes also called partial-volume effects. In this chapter, we use term *spatial resolution effects* because it is more correct and descriptive. Indeed, partial-volume effect is often quantified as the ratio of the measured-to-true radioactivity concentration. The term *partial voluming* is more correctly applied to the problem of tissue heterogeneity within a pixel or region of interest (see discussion in Section III of this chapter).

A. Spatial Resolution Effects

PET images exhibit relatively poor spatial resolution. In fact, the PET image can be thought of as a blurred version of the true radioactivity distribution. Often one approximates the blurring as a low-pass filtering via convolution with a Gaussian kernel (the point-spread function) whose width is specified according to its FWHM. Thus, FWHM is a measure of spatial resolution. The consequence of this convolution is that radioactivity is blurred from one area to adjacent areas. Noting that convolution can be considered

to be a special case of matrix-vector multiplication, we can quantitatively express this relation as:

$$\mathbf{M} = \mathbf{CT} \quad (42)$$

where \mathbf{M} is a vector with values M_i that are the *measured* radioactivity concentrations in region or pixel i , and \mathbf{T} is a vector with values T_j that are the *true* radioactivities in region or pixel j . (Henceforth, we refer only to the case where i and j denote regions and think of the pixel-by-pixel case as a special case of a region containing a single pixel.) \mathbf{C} is the matrix:

$$\mathbf{C} = \begin{bmatrix} \text{HSRC}_1 & \text{CSRC}_{21} & \cdots & \text{CSRC}_{n1} \\ \text{CSRC}_{12} & \text{HSRC}_2 & \ddots & \vdots \\ \vdots & & \ddots & \text{HSRC}_n \\ \text{CSRC}_{1n} & \cdots & & \text{HSRC}_n \end{bmatrix} \quad (43)$$

where HSRC_i is the hot-spot recovery coefficient and reflects the fraction of the true radioactivity in region i that is actually *measured* in region i . On a pixel-wise basis, CSRC_{ij} is the cold-spot recovery coefficient and reflects the fraction of the true radioactivity in region i that is measured in region j . In an ideal system, all HSRC values are unity and all CSRC values are zero. In practice, this is not the case. Values of elements of \mathbf{C} are dependent on size and relative location of pixels or regions.

Components of spatial resolution effects are sometimes described as spill-out and spill-in (Strul and Bendriem, 1999). Spill-out occurs when not all of the radioactivity from the region of interest is measured within its region. Some of the activity is said to spill out into adjacent regions. The amount of spill-out present is dependent on HSRC. Conversely, spill-in is the amount of activity measured in the structure of interest that is, in fact, radioactivity that originates in adjacent structures. The amount of spill-in is dependent on the CSRCs.

Figure 21 provides an illustration of these concepts. Figure 21a represents the true radioactivity concentration distribution of two small hot objects on a warm field. Figure 21b shows the image that would be obtained by PET. Note that the measurable radioactivity distribution appears blurred compared with the true. Intensity profiles are shown in the line plot in Figure 21e and correspond to the true and measured radioactivity concentrations, respectively, along a horizontal line (indicated by hash marks) passing through the centers of images in Figures 21a and 21b. The angular curve represents the Intensity profile in the true activity image, whereas the smooth curve corresponds to the simulated PET image in Figure 21b. In this case, the PET image will underestimate activity in the center of a hot ellipse while overestimating the activity in a background area just outside the hot spot. The activity from the hot ellipses is said to have spilled out from the ellipses and to have spilled in to adjacent areas. The remaining panels of Figure 21 indicate the placement of ROIs on simulated (Figure 21c) and on real PET images of rhesus

monkey brains. Figure 21f shows a surface plot describing the complicated relationship between true activity, object size, and measurable activity for the specific ROI placements shown here. The simulation-generated plot in Figure 21f (the lookup table) was used to correct the PET activities observed in the study of age-related decline of D2 receptor function in monkeys by Morris, Chefer *et al.* (1999).¹⁰

B. Correcting for the Spatial Resolution Effect

In concept, the method for correcting for spatial resolution effects is straightforward. Given \mathbf{M} and \mathbf{C} , solve Eq. (42) for \mathbf{T} . The difficulty arises in determining \mathbf{C} . Different approaches have been used depending on the availability of anatomic data (usually in the form of computerized tomography, CT, or MRI images) and on any *a priori* assumptions that might be appropriate.

1. Corrections Requiring Anatomic Information

In the case that anatomic information is available, the values of C may be calculated as follows.

1. Use regions of interest to mark structures of presumed uniform radioactivity concentration in the tissues of interest, as well as to mark adjacent background areas. For each such region j , create a synthetic image setting pixel values to unity in the given region and zero elsewhere.
2. Blur the image by convolution with a Gaussian kernel with a FWHM that emulates the spatial resolution of the particular PET scanner.
3. Interpret these two pieces of synthetic data in the context of Eq. (42).

Specifically, Steps 1–3 have simulated the case in which T_j is unity and all other elements of \mathbf{T} are zero. Thus, the result of matrix-vector multiplication on the right-hand side of Eq. (42) yields a vector corresponding to column j of matrix \mathbf{C} . Equating this vector to the vector of measured radioactivity concentrations, one defines the HSRC and CSRC values on column j of \mathbf{C} .

4. Repeat this process for all regions to define values for all columns of \mathbf{C} .

With \mathbf{C} determined, the true distribution \mathbf{T} can be estimated for a given measured radioactivity distribution \mathbf{M} by solving $\mathbf{M} = \mathbf{CT}$ for \mathbf{T} . The precision of the result is dependent on the determinant of \mathbf{C} as well as the precision of \mathbf{M} . For details of the implementation, we refer the reader to Rousset *et al.* (1998).

In the case that the true radioactivity concentrations in all but one region are assumed to be uniform and known, an

¹⁰The primary finding of the Morris *et al.* (1999) study is that if spatial resolution effects are *not* corrected, the age-related decline of dopamine (D2) binding potential in monkeys will be overestimated by 50% of the true decline.

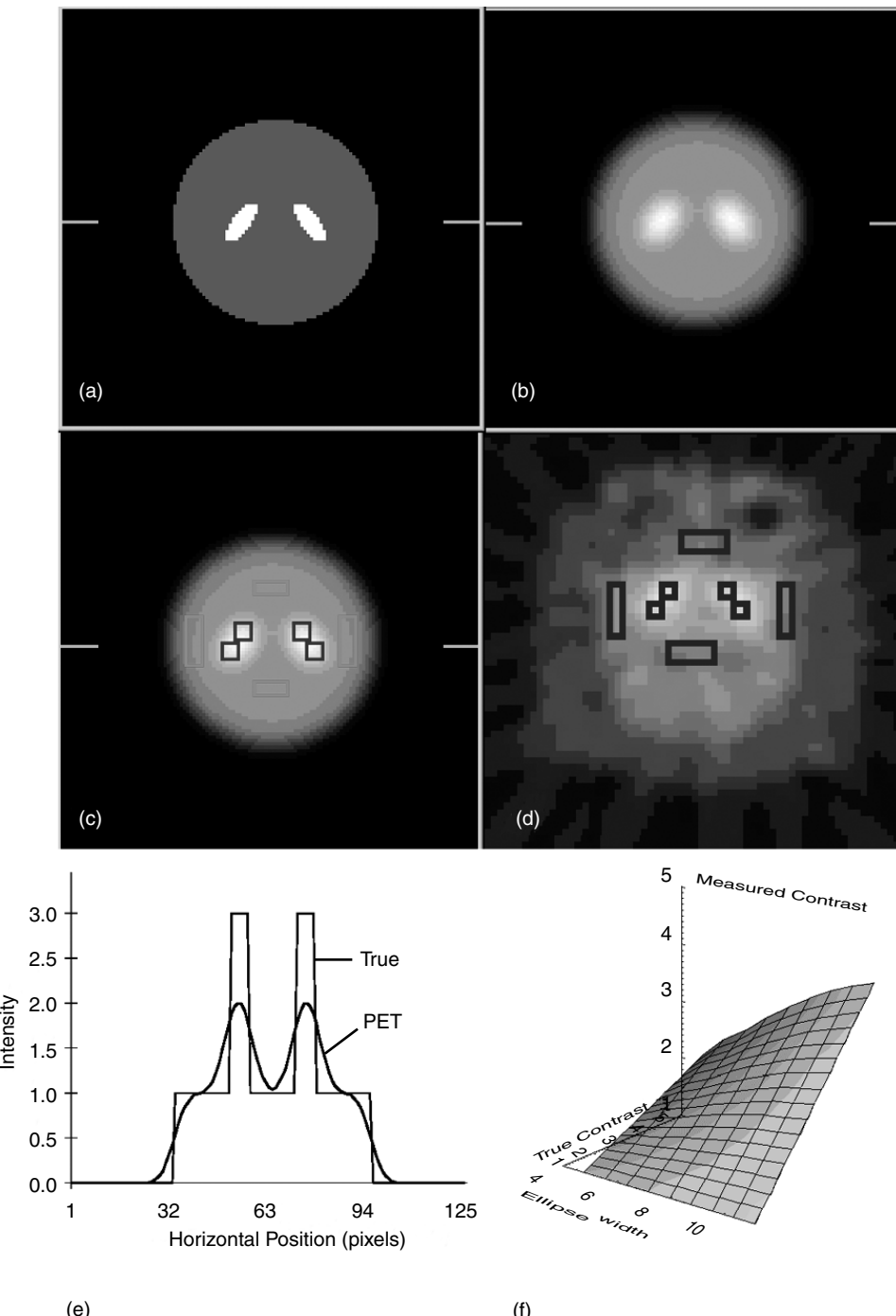


FIGURE 21 (a) Phantom image containing simulated striata. (b) Simulated PET image. Phantom image convolved with impulse response function of PC4096 PET scanner. (c) Placement of regions of interest (ROIs) on simulated PET image used to determine HSRC and CSRC. (d) Comparable placement ROIs on PET image of monkey brain containing striata. (e) Line profiles comparing intensity distributions across true image and simulated PET image. (f) Lookup table (presented as surface plot) relating measured to true activity for hot objects (such as those in image a) of different sizes. (See Morris, Chefer *et al.*, 1999 for details.)

alternative approach may be applied to correct for spatial resolution effects. Termed anatomically guided pixel-by-pixel algorithms (APAs) by Strul and Bendriem (1999), the techniques (Videen 1988; Meltzer *et al.*, 1990, 1996; Muller-Gartner 1992) differ in a few details, but the general principles are the same. In the anatomically guided methods, we confine ourselves to n number of different tissue types. n will be a number much less than the number of pixels in the image. Nevertheless, we treat each tissue type as we treated individual pixels. That is, the tissue types are distinct (masks) and do not overlap. We consider the area being imaged as being composed of a small number of different tissue types—for example, gray matter (GM), white matter (WM), and cerebral spinal fluid (CSF)—with all but one of the types being uniform with respect to radioactivity concentration. Next, the image is decomposed (i.e., segmented) into its constituent tissue types, and a mathematical model of the scanner resolution effects is applied to each in order to account for them so that the radioactivity concentration in the nonuniform tissue may be estimated.

Formally, let index $j = 0$ denote a tissue type with unknown concentration, whereas indices $j > 0$ denote tissue types whose concentrations are assumed to be known and uniform. For each tissue type j , use CT or MRI images to create its binary mask image \mathbf{X}_j containing ones in pixels corresponding to the selected tissue and zeros elsewhere. Thus, the true or ideal radioactivity distribution image \mathbf{I}_{true} can be described as a summation of its constituent parts:

$$\mathbf{I}_{true} = A_0 \mathbf{X}_0 + \sum_{j=1}^{N-1} \bar{A}_j \mathbf{X}_j \quad (44)$$

where A_0 is the radioactivity image of the tissue of nonuniform concentration, \mathbf{X}_0 is its mask image, \bar{A}_j is a scalar denoting the activity concentration in tissue type j , and \mathbf{X}_j is its mask image. The observed image \mathbf{I}_{obs} is related to the true image using convolution with a Gaussian point-spread function G to model spatial resolution effects:

$$\mathbf{I}_{obs} = \mathbf{I}_{true} \otimes G \quad (45)$$

Inserting \mathbf{I}_{true} from Eq. (44):

$$\mathbf{I}_{obs} = \left(A_0 \mathbf{X}_0 + \sum_{j=1}^{N-1} \bar{A}_j \mathbf{X}_j \right) \otimes G \quad (46)$$

Rearranging gives:

$$(A_0 \mathbf{X}_0) \otimes G = \mathbf{I}_{obs} - \left(\sum_{j=1}^{N-1} \bar{A}_j \mathbf{X}_j \right) \otimes G \quad (47)$$

In the case that region 0 is uniform, then A_0 is effectively a scalar, so that:

$$(A_0 \mathbf{X}_0) \otimes G = A_0 (\mathbf{X}_0 \otimes G) \quad (48)$$

in which case, we can solve the equation to determine the true radioactivity concentration in region 0:

$$A_0 = \frac{\mathbf{I}_{obs} - \left(\sum_{j=1}^{N-1} \bar{A}_j \mathbf{X}_j \right) \otimes G}{\mathbf{X}_0 \otimes G} \quad (49)$$

To the extent that region 0 is uniform, this relation can be used to approximate the concentration in region 0.

The two methods presented here for correction of spatial resolution effects, the APA methods (Eqs. 44–49) and the solution of a linear system of equations method ($\mathbf{M} = \mathbf{CT}$), are similar in a number of respects. First, consider the image \mathbf{I}_{obs} and \mathbf{I}_{true} as vectors whose elements correspond to pixel values. In this case the convolutions in Eq. (47) can be written as a matrix-vector multiplication:

$$\mathbf{C}(A_0 \mathbf{X}_0) = \mathbf{I}_{obs} - \mathbf{C} \left(\sum_{j=1}^{N-1} \bar{A}_j \mathbf{X}_j \right) \quad (50)$$

To the extent that tissue 0 is uniform, its activity distribution A_0 is a scalar and can be brought outside the matrix multiplication:

$$\mathbf{C}(A_0 \mathbf{X}_0) = A_0 (\mathbf{C} \mathbf{X}_0) \quad (51)$$

in which case:

$$A_0 (\mathbf{C} \mathbf{X}_0) = \left[\mathbf{I}_{obs} - \mathbf{C} \left(\sum_{j=1}^{N-1} \bar{A}_j \mathbf{X}_j \right) \right] \quad (52)$$

The (approximate) solution technique (used to arrive at Eq. 49) is equivalent to a pixel-by-pixel division of the image on the right-hand side of Eq. (52) by the blurred mask image, $\mathbf{C} \mathbf{X}_0$, in order to estimate A_0 . Clearly, the alternative approach of solving Eq. (50) as a linear system of equations to obtain A_0 is a more rigorous approach than Eq. (49). However, the number of computations needed for the rigorous approach is much greater than for the approximate solution.

A major limitation of the correction methods described thus far is that they require anatomic information. Often CT or MRI is not available to provide such information. Moreover, the methods require that the anatomic and functional images be spatially co-registered. Inaccuracies in registration affect the accuracy of subsequent corrections (Strul *et al.*, 1999).

2. Corrections Not Requiring Anatomical Information

Corrections that do not require anatomical data are loosely classified into those that are based on a pharmacokinetic model and those that are based on a model of the tissue boundary. Ones based on a pharmacokinetic model include parameters such as HSRC or CSRC in addition to the usual physiological parameters to be estimated. This

approach is most prevalent in cardiac data analysis in which radioactivity in the ventricular cavity spills out into the surrounding myocardium (Herrero *et al.*, 1989). The difficulty with this approach is that estimates of the physiological parameters of interest are often unreliable due to a strong correlation between them and the correction parameters (Feng *et al.*, 1996; Muzic *et al.*, 1998).

Correction methods based on a model for tissue boundaries try to estimate the size and location of tissue boundaries simultaneously with the radioactivity concentration. For example, a cancerous lesion might be modeled as a sphere of unknown radioactivity concentration superimposed on a region that is locally uniform in radioactivity (Chen *et al.*, 1999). An optimization is then performed to find the combination of sphere diameter and radioactivity concentration that best matches the measured data. One pitfall of this approach is that when the diameter of the lesion is much smaller than the scanner resolution FWHM, the lesion's apparent size in the image is largely unrelated to its true size and it cannot be estimated reliably. Because lesion size and radioactivity concentration are highly correlated, neither size nor concentration can be estimated reliably (Chen *et al.*, 1999).

3. Comparison of Methods

Methods that use anatomical data have both advantages and disadvantages compared to those that do not require such data. Methods that use anatomical data are better able to estimate tissue radioactivity of very small lesions because the lesion size is specified. Thus, the correlation between lesion size and radioactivity is not an issue. The disadvantage of the anatomically based methods is this same requirement for anatomical data. Such data may not always be available or may be expensive to obtain. Moreover, the analyses presume perfect registration of the anatomical images to the PET, as well as proper segmentation of the anatomic images. These requirements add significant burdens to the data processor, and the final results are heavily dependent on how well each of these steps is performed.

VII. FUNCTIONAL IMAGING OF NEUROCHEMISTRY—FUTURE USES

Neuroimagers must resist the temptation to view the brain as composed of functional units approximately 1 cubic centimeter in size, that is, on the order of the resolution of their imaging device. On one crude measure, the brain does work that way—general functions of the brain often are organized on that sort of spatial dimension. However, many brain functions are carried out by diffuse neurochemical pathways—systems of neurons whose axons and dendrites spread through much of the brain but compose only a small

portion of each brain region (Cooper *et al.*, 1996; Squire and Kandel, 1999). Some of these systems, those that use norepinephrine, acetylcholine, dopamine, or serotonin, are known to play critical roles in such varied functions as learning, memory, attention, pleasure, reward, and mood. These pathways are frequently activated independently of the surrounding brain tissue, and their activity therefore cannot be determined by conventional activation studies that rely on detecting gross changes in blood flow. Can brain imaging detect the activity of functional subpopulations of neuronal elements?

PET offers a possibility. It requires the combination of quantitative neurotransmitter receptor imaging, as described earlier, with techniques of conventional brain activation imaging. As has been mentioned, the premise is that competition occurs between an injected radioligand and a neurotransmitter for binding to a limited population of receptors. In practical terms, a patient is injected with a neurotransmitter receptor radioligand, such as a dopamine receptor ligand, while performing a brain activation task. If a task stimulates a particular neurotransmitter system under study (e.g., dopamine neurons), then we would expect more of the transmitter (dopamine) to be released into the synapse. Released intrasynaptic dopamine competes for receptor sites with an appropriately chosen radioligand. Hence, there should be a decrease in the amount of specific radioligand binding observed (Figure 22). By comparing the specific binding at rest with that during activation, we can demonstrate the activation of a subset of neurochemically distinct neurons—in this example, a dopaminergic pathway.

In principle, and given an appropriate ligand, our induced competition technique could be applied to any neurochemical pathway. Radioligands are currently being developed or are already available for imaging dopamine, serotonin, acetylcholine, GABA, histamine, norepinephrine, and other synapses. Thus, functional neurochemical maps of the brain could be created that complement the general activation maps being produced with conventional functional brain imaging (¹⁵O-water studies in PET or fMRI.).

The site of the neurochemical competition in question is the synapse. Synapses are specialized structures that allow one neuron to communicate with another chemically. The transfer of chemical information takes anywhere from 2 milliseconds for fast (e.g., glutamate) synapses to tens or hundreds of milliseconds (or occasionally many seconds) for slow (e.g., serotonin or muscarinic acetylcholine) synapses. The steps of information transfer are schematized in more detail in Figure 23.

A. Can Neurotransmitter Activation Imaging Really Work?

Although the concept of competition between endogenous neurotransmitter and injected radioligand makes sense

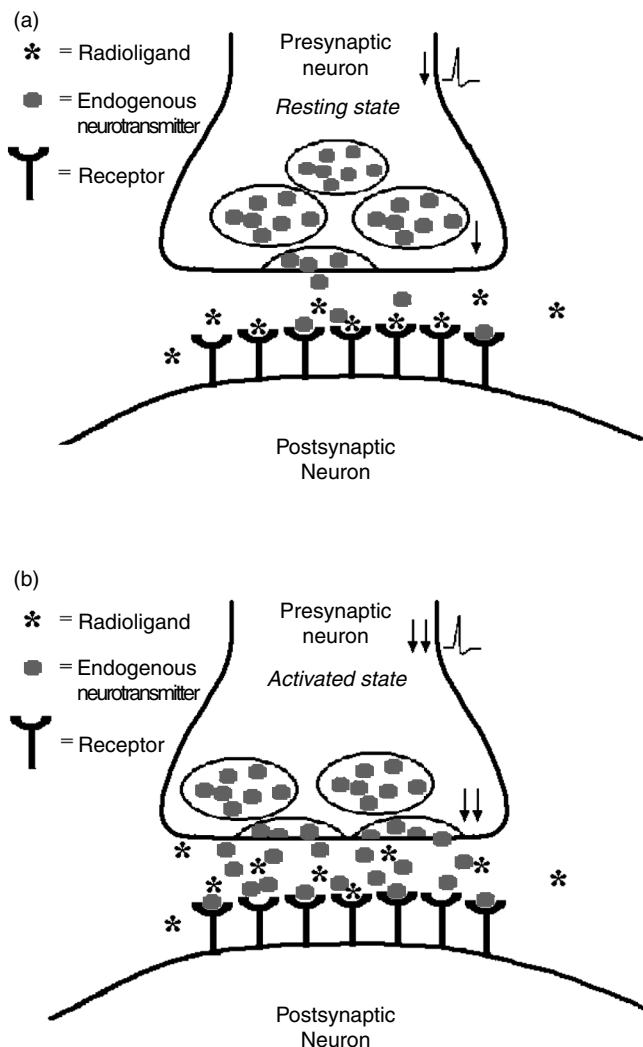


FIGURE 22 (a) Schematic of dopamine neuron at rest. Number of red circles sitting in receptor cups indicates the basal level of occupation of receptors by endogenous ligands. (b) Schematic of dopamine neuron during activation. Note increase in number of postsynaptic receptors occupied by endogenous ligands.

intuitively, rigorous scientific proof of the validity of this activation-imaging technique is required. The strongest evidence that PET can be used to image neurotransmitter release comes from experiments in nonhuman primates in which a microdialysis system is surgically implanted in the brain to measure extracellular concentrations of dopamine (DA) (Breier *et al.*, 1997; Endres *et al.*, 1997; see analogous experiments using SPECT in Laruelle *et al.*, 1997). While in a PET scanner, monkeys were injected with amphetamine, which causes increased release of DA into the synapse. The DA receptor binding is assessed with PET while the extracellular concentration of DA is simultaneously measured by microdialysis. Microdialysis experiments detected increased

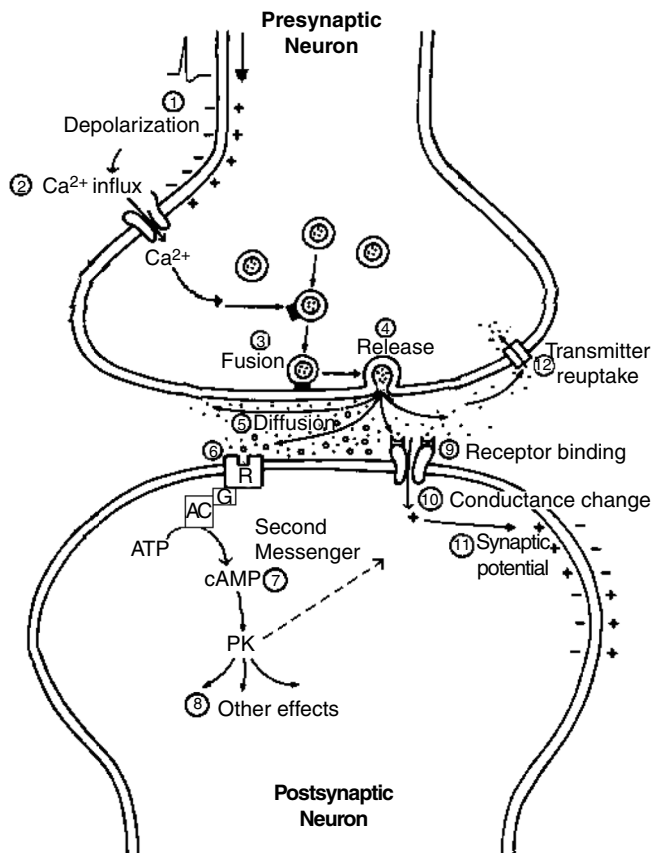


FIGURE 23 Detailed schematic of trans-synaptic chemical transmission of signal. (1) When an electrical signal, usually in the form of an action potential, reaches the presynaptic terminal, it depolarizes the membrane of the terminal, which normally rests at approximately -70 mV (inside compared to outside the cell). (2) This depolarization causes voltage-sensitive Ca²⁺ channels in the presynaptic membrane to open, allowing a brief influx of Ca²⁺ ions. (3) The Ca²⁺ ions interact with calcium-sensitive proteins to initiate a chain of events that causes the vesicles, which contain neurotransmitter molecules, to fuse with the presynaptic membrane. (4) This results in the release of the transmitter into the synaptic cleft. (5) The transmitter diffuses throughout the cleft. (Note that the schematic drawing does not properly indicate the extreme narrowness of the cleft—it is only 20 to 30 nm wide.) (6) Transmitter molecules bind to receptors on the postsynaptic membrane. In the left side of the figure, receptors coupled to intracellular second messenger systems are shown. These receptors are found in slow synapses, such as dopamine, norepinephrine, and muscarinic acetylcholine synapses. (7) In a slow synapse, binding of the transmitter to the receptor activates an enzyme, usually through a G-protein, which activates an enzyme that causes a change in concentration of a second messenger. The example shown here is adenylyl cyclase (AC) causing an increase in cAMP. (8) Many second-messenger systems work by activating a protein kinase (PK). The protein kinase then phosphorylates any of a large number of proteins. Transmitter receptors and membrane ionic channels are among the many possible targets of protein kinases. (9) At fast synapses, transmitter molecules bind to a different type of receptor. (10) This receptor itself is an ionic channel and when it binds transmitter it opens, allowing ions to flow in or out of the cell. (11) At fast excitatory synapses, as shown here, positively charged Na⁺ ions, and sometimes Ca²⁺ ions too, flow in, depolarizing the postsynaptic cell. At fast inhibitory synapses, the pore is usually a Cl⁻ channel. (12) The action of the neurotransmitter is terminated by diffusion out of the synaptic cleft and by active reuptake into the presynaptic terminal. The membrane molecule responsible for this reuptake is called a transporter. (Adapted from Shepherd, 1998.)

extracellular DA while PET detected decreased binding of [¹¹C]-raclopride. The degree of the increase in DA was shown to correlate with the degree of reduction of receptor-ligand binding. This is strong evidence that the DA is affecting the PET signal by competing with the radioligand for binding sites.

B. Activation of the Dopamine System by a Task Can Be Imaged

Initially, this approach to synaptic imaging was performed using drugs that produce enormous increases in neurotransmitter concentrations. However, it has also been suggested via simulations that mental or physical tasks might be sufficient to produce a detectable change in the PET signal (Fisher *et al.*, 1995; Morris *et al.*, 1995). In 1998 there was an experimental breakthrough. Koepp and colleagues (1998) performed PET imaging of dopamine D₂ receptors using [¹¹C]-raclopride. They first imaged subjects at rest and then again while subjects played a video game beginning just prior to injection and continuing throughout the PET imaging procedure. The video game required subjects to maneuver a tank through a battlefield by manipulating a joystick. To motivate the subjects, they were promised monetary rewards commensurate with their success at the game.

From their data, Koepp *et al.* (1998) estimated the BP of [¹¹C]-raclopride in the striatum at rest and compared it to the BP during the video game. The technique they used to calculating BP was developed by Gunn *et al.* (1997) and is discussed in Section VB. The researchers found that playing the game resulted in a decreased binding potential, which they interpreted as an increase in DA release. The task used by Koepp *et al.* included both motor and reward components, both of which have been implicated strongly in the function of the dopaminergic system (Schultz, 1997; Chase *et al.*, 1998). Unfortunately, it is not possible to say which aspect(s) of the task caused the DA release. In all likelihood, the motor and reward components were both involved, but this is a subject for future study.

More recently, a similar experiment has been reported using SPECT (Larisch *et al.*, 1999; Schomartz *et al.*, 2000). Subjects were injected with [¹²³I]-iodobenzamide, a D₂ receptor ligand. Starting just before injection and continuing for 30 minutes afterward, the subjects performed a constant task of writing with their right hand. Imaging was performed after completion of the task (90 minutes postinjection). Binding potential was approximated by calculating the ratio of the activity in an ROI (striatum) to that in a reference region (frontal cortex). A note to modelers: Because binding potential equals the ratio of ligand in the bound to free compartments at steady state, this direct measurement of binding potential may be justified under

certain conditions. If not, a model-based estimation of binding potential or some other relevant parameter is preferable.¹¹ Nonetheless, the analysis of Larisch and colleagues appeared to show a decrease in available D₂ receptors in the striatum compared to control subjects who did not perform the handwriting task. If the data are valid, they suggest that the handwriting task activated dopaminergic neurons, and the consequent increase in DA release in the striatum interfered with radioligand binding. These results, while interesting, are less convincing than those of Koepp *et al.* (1998), first, perhaps because of their inferior analysis methods and, second, because the decreased binding that they did find was statistically significant only in the right striatum. This is a bit curious because we expect the effect to be bilateral. The authors of the study conjecture that postural movements that accompany the handwriting task might explain the right-sided striatal dopamine release. If this SPECT study or others like it can withstand more rigorous analysis, then we may begin to see neurotransmitter activation studies being performed with SPECT as well as PET.

Two intriguing developments in the area of neurotransmitter activation imaging were published too late for discussion in this chapter, each of which offers methods for producing images of dopamine activation from single dynamic PET scans (see Alpert *et al.*, 2002; Pappata *et al.*, 2002). Both methods are related, in principle, to the method of Friston *et al.* (1997), which uses the generalized linear model to look for statistically significant excursions from the dynamic [¹¹C]-raclopride PET curve that one would expect were no DA activation present.

C. Clinical Uses of Neurotransmitter Activation Studies

The most significant clinical use of neurotransmitter imaging so far has been in the field of schizophrenia. Schizophrenia is a relatively common psychiatric disease, striking approximately 1% of the population, and is usually devastating to the victim. Patients commonly experience hallucinations (including hearing voices) and delusions (false beliefs). Most schizophrenics eventually withdraw from society and suffer frequent hospitalizations (Kaplan

¹¹Really, we must know that (a) a steady-state ratio of ligand in bound and free compartments has been reached. In addition, (b) the frontal cortex must be a valid reference region for this ligand, (c) there must not be any significant nonspecific binding of the ligand in either region, and (d) there must not be any significant plasma radioactivity at the time of scanning. If these four conditions are satisfied, then the activity in the reference region can be used as an approximation of the concentration of free ligand in the ROI. Further, the activity in the ROI minus the activity in the reference could be used as an approximation of the activity in the bound compartment alone in the ROI. Then the ratio of these two would be a fair approximation of the binding potential. For a good comparison of single-scan to more sophisticated modeling techniques see Koepp *et al.* (1994).

and Sadock, 1998). The cause of schizophrenia remains unknown. One of the first and most widely known hypotheses, called the dopamine hypothesis, postulates that the underlying defect is an abnormality in the dopaminergic system (Carlsson and Lindqvist, 1963; Soares and Innis, 1999). It was formulated decades ago and is based primarily on two observations. (1) The most effective treatments for schizophrenia are drugs that block dopamine receptors; the ability of these drugs to relieve the psychotic symptoms of schizophrenia correlates with the affinity of the drugs for the D2 receptor. (2) Certain drugs (e.g., amphetamine) that increase DA release can cause psychotic symptoms that resemble symptoms of schizophrenia.

Sadly, there has been no definitive identification of the abnormality in the dopamine system of schizophrenics. Powerful support for the hypothesis appeared when Wong *et al.* (1986) published data demonstrating an increased number of dopamine receptors in schizophrenics compared to controls. However, this was followed by a report from Farde *et al.* (1990) demonstrating no difference in receptor number between schizophrenics and controls. The resolution of these conflicting results is still subject to debate. Perhaps the strongest evidence for the dopamine hypothesis comes from recent pharmacological neurotransmitter activation studies. Using amphetamine to stimulate the release of DA and using either SPECT (Laruelle *et al.*, 1996) or PET (Breier *et al.*, 1997), researchers have shown that the stimulated release of DA is greater in schizophrenics than it is in controls. If it can be shown that schizophrenics similarly overrespond to ordinary sensory stimuli or to stress or social interactions, then the dopamine hypothesis will be strengthened. In a sort of deactivation study with SPECT, subjects were given alpha-methyl-para-tyrosine (α -MPT)—a drug that temporarily depletes dopamine stores from the presynaptic terminals. The result was an increase in the available D2 receptors, presumably secondary to reduced levels of endogenous dopamine (Abi-Dargham *et al.*, 2000). In this experiment, schizophrenics showed a significantly greater increase in B_{max} (19%) under α -MPT than did normal volunteers (9%), suggesting that schizophrenics have more baseline dopamine in their synapses than normals. The aforementioned experiments demonstrate how neurotransmitter activation studies can be used to test the dopamine hypothesis of schizophrenia.

D. Caution in the Interpretation of Neurotransmitter Activation Studies

The simplest interpretation of neurotransmitter activations studies, namely, that a task stimulates release of the transmitter that then competes with the radioligand for limited binding sites, has been challenged (Inoue *et al.*, 1999; Tsukada *et al.*, 1999; Laruelle, 2000). This competition-based hypothesis fails to account for three observations.

1. The degree of inhibition of radioligand binding does not always correspond to the degree of elevation of extracellular DA stimulated by certain pharmacological agents. In other words, there are examples of drugs producing greater DA release but apparently less inhibition.
2. The inhibition of radioligand binding often persists well beyond the time that extracellular DA is increased. The persistence of inhibition appears to be at variance with predictions of simulations using well-established kinetic parameters of raclopride.
3. The binding of some DA radioligands is not inhibited by DA release and might even increase as DA increases!

It may yet be possible to reconcile recent observations with the competition hypothesis, but other factors probably also contribute to the data. For example, it is likely that pharmacological stimulation often results in changes in the local microenvironment near the postsynaptic receptors (Inoue *et al.*, 1999). Such changes would include the charges on the external surface of cell membranes, affecting the ability of polar radioligands or neurotransmitters to diffuse to postsynaptic receptors. (Consider that DA, serotonin, and many other neurotransmitters are charged molecules at neutral pH.)

A second concern is that the number of functional postsynaptic receptors can change during pharmacological or synaptic activity (Nicoll and Malenka, 1999; Zhou *et al.*, 2001). This happens when available receptors can become internalized by the cell or, alternatively, new receptors can become inserted into the membrane. The functional properties of most receptors, including their binding affinities, can be altered by phosphorylation or other chemical modification, which can be a consequence of pharmacological or synaptic stimulation (Nicoll and Malenka, 1999). The postsynaptic membrane, in other words, is not a static structure but is always changing. Receptors are being added and taken away, and the properties of the receptors are changing as they become phosphorylated or dephosphorylated. The time course and magnitude of these fluctuations are not accurately known, but, if they are rapid relative to the time course of a PET study and large relative to the local receptor density, they could complicate the analysis of transmitter activation studies.

1. Cautions for Modelers of Neurotransmitter Activation Studies

Let us review the preceding discussion from the standpoint of a modeler who wants to explain a neurotransmitter activation experiment in three or fewer compartments. In the world of simplistic compartmental models, changes in the microenvironment of the synapse might mean that V_R , the volume of reaction (Delforge, 1996), is not a constant for the duration of the experiment. This is equivalent to saying that k_{on}/V_R (i.e., the effective association rate

constant) varies during the experiment. If the number of postsynaptic receptors (or their efficiency) changes while we are conducting our experiment, then B_{\max} is not a constant. If receptors are being phosphorylated while the image is being acquired, then their affinity for the ligand might be changing. Because affinity is $K_D = k_{off}/k_{on}$, then either k_{off} or k_{on} , or both, might be changing. Each of these possibilities contradicts one of our key model assumptions—that the model contains only time-invariant parameters. If any of our presumed time-invariant parameters changes during the image acquisition, then our model becomes decidedly more complicated—and our parameters become much more difficult to estimate—especially because some of our formerly constant parameters are now functions.

E. PET Imaging and Kinetic Modeling Issues in Gene Therapy

For several decades, gene therapy has been widely and eagerly anticipated as a potentially great advance in medicine. Gene therapy can be defined broadly as the introduction of functioning genes into patients in an effort to treat disease. It can be achieved in one of two general ways. One is by placement of a normal gene into the tissue of patients who, because of a mutation, lack a particular gene or possess a faulty one. An example of such a mutation is cystic fibrosis, which is caused by a defective gene for a protein that normally serves as both a chloride channel and a modulator of other ionic channels. The second strategy depends on introducing a deleterious gene directly into tumors. The expression of the gene by tumor cells leads directly to self-destruction or at least increased susceptibility to destruction by chemotherapeutic drugs or the immune system. In both cases, the therapeutic gene may be introduced into the tissue of interest by packaging the gene in a virus or liposome and then infecting the patient. Many clinical gene therapy trials are underway, although currently only a very moderate clinical success has been achieved. The introduction of the normal gene into the airways of patients with cystic fibrosis has yielded some therapeutic value, although the effect lasts only a few weeks (Albelda, *et al.*, 2000).

One of the main problems hindering gene therapy research and development is a difficulty in monitoring the actual expression of the therapeutic gene. Levels of gene expression (measured as amount of protein being produced by transcription and translation of the therapeutic gene) and the distribution throughout the body must be quantified *in vivo*, both in animals and, ultimately, in human subjects. PET offers exciting potential in this area. As we have seen, it is well-suited to *in vivo* quantification and it is usually capable of scanning the whole body (MacLaren *et al.*, 2000; Hustinx *et al.*, 2000).

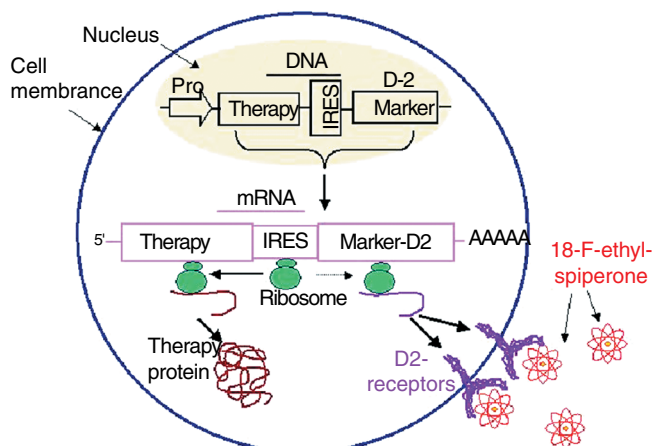


FIGURE 24 A marker gene is linked to a therapeutic gene and provides a marker of gene therapy success. A single piece of DNA contains both the therapeutic gene and a marker gene, separated by an internal ribosomal entry site (IRES). A single promoter (Pro) controls transcription of both genes. (Without the IRES, only the first gene would be reliably transcribed.) The marker gene in this case codes for a dopamine (D2) receptor, which becomes inserted into the cell membrane. Following injection of 18-F-ethylspiperone, a PET scan will quantify the number of dopamine receptors, which is proportional to the amount of therapy protein. (Adapted from Yu *et al.*, 2000.)

1. Monitoring Gene Expression—Two Methods

The first step in using PET to monitor gene therapy is to construct a piece of DNA that contains both the therapeutic gene and a second gene, called the marker gene (see Figure 24; note the term *reporter* is sometimes used instead of *marker*). The marker gene does not contribute to the therapy but instead encodes a protein that is capable of being measured *in vivo* by PET. The piece of DNA must be constructed in such a way that whenever the therapeutic gene is transcribed and translated into a protein molecule, so is the marker gene, so that the amounts of the therapy protein and the marker protein are the same or at least consistently proportional to one another. A PET scan would thus measure the amount of marker protein being expressed in the subject, from which it can be inferred how much of the therapy protein has been expressed. Constructing the requisite piece of DNA is not easy, but there has been considerable preliminary success (Tjuvajev *et al.*, 1998; MacLaren *et al.*, 1999). One of the DNA cassettes and its action is depicted in Figure 24.

The marker gene protein can function in one of two ways. It can be a cell surface receptor, such as a dopamine receptor (MacLaren *et al.*, 1999). This method is schematized in Figure 24. Cells that normally do not normally express dopamine receptors will do so if they have successfully taken up the DNA containing therapy and marker genes. The number of the resulting dopamine receptors can be quantified, as we have discussed at length earlier in this

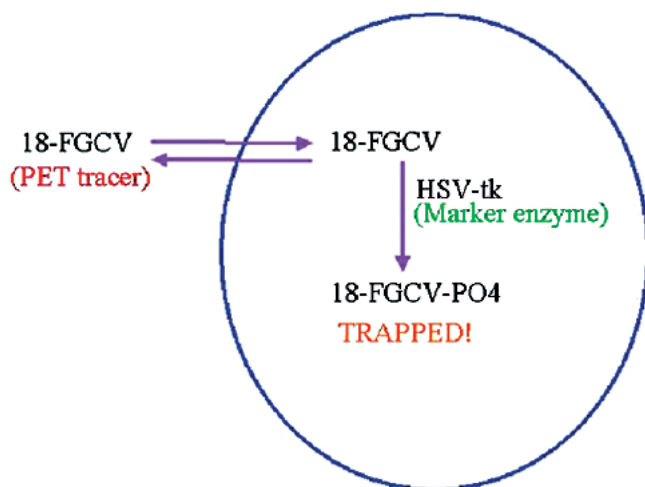


FIGURE 25 Marker gene codes for an enzyme. In this example, the marker gene codes for the viral enzyme thymidine kinase, abbreviated HSV-tk (herpes simplex virus thymidine kinase). When the PET radiotracer 18-F-GCV (fluoroganciclovir) is administered to the subject or tumor, it is taken up by a wide variety of cells. In normal cells, it quickly washes out of the cell. However, in cells that have received gene therapy and are producing viral thymidine kinase, GCV is phosphorylated and cannot leave the cell. A subsequent PET scan, therefore, will demonstrate the tissue location and magnitude of therapeutic gene expression.

chapter. A second type of marker protein is an intracellular enzyme that modifies (e.g., phosphorylates) a radioactive PET probe, rendering the probe impermeant to cell membranes (Tjuvajev *et al.*, 1998; Hustinx *et al.*, 1999; Bankiewicz *et al.*, 2000). (see Figure 25). The result is that cells that express the marker gene trap the PET probe, much the way that tumor cells and other cells trap 18-FDG (see Section III of this chapter). In the example shown, the marker protein is the viral enzyme HSV-tk, and the PET probe is 18-F-ganciclovir (18-F-GCV). It is worth noting that the ganciclovir–HSV-tk system is particularly attractive because the HSV-tk gene is both the therapeutic gene and the marker gene! Ganciclovir is a drug that after being phosphorylated by HSV-thymidine kinase becomes highly toxic. Therefore, ganciclovir can be administered intravenously to the subject and any tumor cells that have received and expressed the therapeutic gene will be killed. Prior to administering ganciclovir treatment, those same cells can be imaged with 18-F-GCV. This eliminates the potentially troublesome problem of deducing therapeutic gene expression from measurements of marker gene expression.

2. Quantification Issues

Many efforts are currently underway to monitor gene therapy with PET. To be useful, however, PET must not only visualize tissue that expresses the marker protein, but must also quantify the amount of protein present. Quantification will require kinetic modeling similar to the methods

described earlier. There may also be some unique problems that must be addressed by the modeler.

- When a cell that normally does not express dopamine receptors is stimulated to do so, what proportion of the produced receptors end up on the cell membrane? Does this vary from tissue to tissue?
- Does the number of receptors implanted into the cell membrane saturate? In other words, is the number of receptors in the membrane (to be measured by PET) linearly related to the number of receptors (and hence the therapeutic protein) produced by the cell?
- How does the number of available receptors in the tissue (B_{max}) vary over time? Suppose, for example, that PET imaging at 24 hours after introduction of the gene yields a good estimate of dopamine receptor production, but by 72 hours most of the receptors have been degraded or internalized. Imaging shortly after transfection would be required. On the other hand, early imaging after transfection may not allow enough time for all the expressed dopamine receptors to become positioned in the membrane where they will be accessible to a radioligand. In modeling terms, we have to assume B_{max} is constant even though, in gene therapy systems, it is actually a function of time. One must find a time after gene transfer at which B_{max} is relatively constant and is a reliable indicator of both marker and therapeutic gene expression. This issue is also relevant for the case of a marker gene that is an enzyme leading to trapping of the PET tracer.
- Consider the case of the marker gene as enzyme. Does the transport of the PET tracer into the cells occur at the same rate *in vivo* as it does *in vitro*, and is the transport in tumor cells the same as in normal cells? In other words, how can we estimate a value for k_1^* ? This is similar to the problem of calculating the lumped constant in FDG quantification.

We must keep in mind that the goal of this imaging exercise is to estimate the amount of expression of the therapeutic gene. As such, it will not be useful if one cannot establish a consistent relationship between marker gene expression and therapeutic gene expression. Expression of the marker gene must be detectable with PET. Establishing that these relationships are true and detectable is currently being explored in animal studies (see, for example, Yu *et al.*, 2000).

VIII. A GENERALIZED IMPLEMENTATION OF THE MODEL EQUATIONS

A. State Equation

The models and equations in the preceding sections may be generalized to consider the case of an arbitrary number

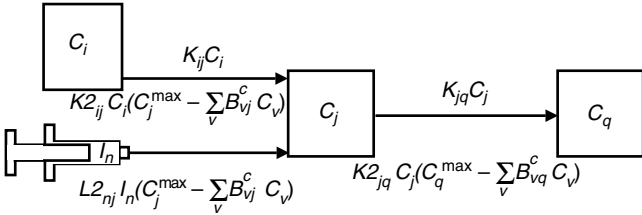


FIGURE 26 Building blocks used to define compartment models. Compartments are shown as rectangles. Arrows indicate unimolecular (labeled above arrow) and saturable bimolecular (labeled below arrows) fluxes. (Note: The graphical representation of a building block might appear on first glance to be equivalent to a compartmental model, but it is; a building block is the graphical depiction of a mass balance on a single compartment. Thus, the appropriate analogy is between a building block and an ordinary differential equation.) (Reprinted by permission of the Society of Nuclear Medicine from: Muzic R.F., et al. COMKAT: Compartment Model Kinetic Analysis Tool. *J Nucl Med* 2001; 42:636–645.)

of inputs and compartments. Consider a model as being constructed from a number of building blocks (Muzic and Cornelius, 2001). Specifically, in building block j , compartment j is the recipient of material from one or more inputs and one or more compartments, and compartment j also serves as the source for material for one or more compartments. This is depicted in Figure 26. Thus, a model with N compartments may be described using building blocks $j = 1, 2, \dots, N$.

The state equation describing fluxes into and out of compartment j may be written as follows. First, consider the flux from as many as n inputs. If an exchange is unimolecular, the flux is proportional to the concentration in the source inputs and its contribution to the state equation for compartment j is:

$$+\sum_n L_{nj} I_n \quad (53)$$

where L_{nj} denotes the apparent unimolecular rate constant from input n to compartment j , I_n is the molar concentration of input n , and the summation is over all inputs n . If the exchange is saturable as a result of a limited number of binding sites in compartment j , then the contribution is usually a bimolecular term and is given by:

$$+(C_j^{\max} - C_j) \sum_n L2_{nj} I_n \quad (54)$$

where $L2_{nj}$ denotes the apparent bimolecular rate constant from input n to compartment j , C_j^{\max} is the concentration of binding sites in compartment j , and C_j is the concentration in compartment j .¹² Normally compartment j

may be considered to be nonsaturable or saturable, but not both. When it is nonsaturable all values $L2_{nj}$ are zero, whereas when it is saturable all values L_{nj} are zero.

Material may enter compartment j from other compartments. The terms describing these contributions are analogous to those shown earlier in which inputs served as the source of material:

$$+\sum_i K_{ij} C_i \quad (55)$$

when compartment j is nonsaturable, and:

$$+(C_j^{\max} - C_j) \sum_i K2_{ij} C_i \quad (56)$$

when it is saturable. Here K_{ij} and $K2_{ij}$ denote, respectively, the apparent unimolecular and bimolecular rate constants from compartment i to compartment j , and $(C_j^{\max} - C_j)$ denotes the concentration of sites available for binding.

Compartment j may serve as the source of material to other compartments q . Because this corresponds to a loss of material from compartment j , these terms are written with negative signs. The terms are:

$$-C_j \sum_q K_{jq} \quad (57)$$

for nonsaturable recipient compartments q , and:

$$-C_j \sum_q K2_{jq} (C_q^{\max} - C_q) \quad (58)$$

for saturable recipient compartments q . Compartment q may be considered as either nonsaturable or saturable, but not both. When it is nonsaturable all values $K2_{jq}$ are zero, whereas when it is saturable all values K_{jq} are zero.

The state equation for compartment j is thus written as the sum of all contributions and losses already described:

$$\begin{aligned} \frac{dC_j}{dt} = & \sum_n L_{nj} I_n + (C_j^{\max} - C_j) \sum_n L2_{nj} I_n + \sum_i K_{ij} C_i \\ & +(C_j^{\max} - C_j) \sum_i K2_{ij} C_i - C_j \sum_q K_{jq} - C_j \sum_q K2_{jq} (C_q^{\max} - C_q) \end{aligned} \quad (59)$$

A set of such equations, one equation for each compartmental building block, defines the exchanges in a multi-compartment, multiinput model.

Using the preceding formulation, the model equations have been implemented in MATLAB (The MathWorks, Inc., Natick, MA) in a program called COMKAT: Compartment Model Kinetic Analysis Tool (Muzic and Cornelius, 2001), which is available for download at www.nuclear.uhrad.com/comkat. In this implementation it is convenient to maintain the compartment and input concentrations in vectors \mathbf{C} and \mathbf{I} , respectively, and the rate constants in matrices \mathbf{L} , $\mathbf{L2}$, \mathbf{K} , and $\mathbf{K2}$ with sizes given in Table 2, in which *Num. Inputs* is the number of inputs and

¹²An important point is that in this formulation the compartment concentrations are maintained as molar and not as radioactivity concentrations. This is because biochemical processes are dependent on molar concentration and not on radioactivity. Radioactivity is used only because it permits the measurements based on the external measurement of gamma rays.

TABLE 2 Matrix Dimensions in General Model Implementation

	Rows	Columns
I	Num. inputs	1
C	Num. Comptm'ts	1
K	Num. Comptm'ts	Num. Comptm'ts
K2	Num. Comptm'ts	Num. Comptm'ts
L	Num. inputs	Num. Comptm'ts
L2	Num. inputs	Num. Comptm'ts

Num. Comptm'ts is the number of compartments. The state equation for the set of compartments is then written as

$$\dot{\mathbf{C}} = F(\mathbf{C}) = \mathbf{L}'\mathbf{I} + (\mathbf{C}^{\max} - \mathbf{C}) \cdot (\mathbf{L2}'\mathbf{I}) + \mathbf{K}'\mathbf{C} + (\mathbf{C}^{\max} - \mathbf{C}) \cdot (\mathbf{K2}'\mathbf{C}) - \mathbf{C} \cdot \text{sum}(\mathbf{K}, 2) - \mathbf{C} \cdot (\mathbf{K2}(\mathbf{C}^{\max} - \mathbf{C})) \quad (60)$$

where $\dot{\mathbf{C}}$ denotes the time derivative of \mathbf{C} , F is a function that takes \mathbf{C} as input and returns $\dot{\mathbf{C}}$, and $'$ denotes matrix transpose. Moreover, following MATLAB notation, the \cdot * operator indicates element-by-element multiplication and $\text{sum}(\mathbf{K}, 2)$ indicates a column vector obtained by summing each row in \mathbf{K} .

In some cases it is desirable for a single saturable pool of binding sites to be represented by multiple compartments. Consider a study involving a particular receptor and more than one injection of ligand (as discussed previously). For each injection, the specific activity is different (Delforge *et al.*, 1990). For ligand that is bound to the receptor, one may assign separate compartments corresponding to each injection in order to differentiate between ligands from each injection. In this case, there is only one pool of binding sites, but the sites may be occupied by material from any injection. To accommodate this, our formulation is extended by introducing a coupling matrix \mathbf{B}^c (a square matrix with dimensions: Num. Comptm'ts) with elements B_{ij}^c that equal unity when compartments i and j correspond to a common pool of receptors and that equal zero otherwise. Thus, the number of available binding sites is calculated as $(\mathbf{C}^{\max} - \mathbf{B}^c \mathbf{C})$ and the state equation is revised to:

$$\dot{\mathbf{C}} = F(\mathbf{C}) = \mathbf{L}'\mathbf{I} + (\mathbf{C}^{\max} - \mathbf{B}^c \mathbf{C}) \cdot (\mathbf{L2}'\mathbf{I}) + \mathbf{K}'\mathbf{C} + (\mathbf{C}^{\max} - \mathbf{B}^c \mathbf{C}) \cdot (\mathbf{K2}'\mathbf{C}) - \mathbf{C} \cdot \text{sum}(\mathbf{K}, 2) - \mathbf{C} \cdot (\mathbf{K2}(\mathbf{C}^{\max} - \mathbf{B}^c \mathbf{C})) \quad (61)$$

B. Output Equation

The output equation relates compartment and input concentrations to the model output. Most typically, model output is defined to have a correspondence to measured data and is used in data fitting. In the case of nuclear medicine applications, the measured data are the externally detected

radioactivity. Thus, the output equation must relate radioactivity concentrations to the compartment concentrations that are maintained in terms of molar concentration. This is done by scaling the compartmental concentrations by the specific activity that expresses the radioactivity strength in terms of picomoles per microcurie ($\text{pmol}/\mu\text{Ci}$). Specific activity from material u at time t is calculated as:

$$A_u = A_u^0 \exp(-d_u t) \quad (62)$$

where A_u^0 is the specific activity at $t = 0$, and d_u ($= \ln(2)/\text{half-life}$) is the radioactivity decay constant. A_u^0 is measured in an aliquot of material that is not injected. Thus, the contribution of the compartments to output l is calculated as:

$$\sum_u W_{ul} A_u C_u \quad (63)$$

where W_{ul} is the weight that compartment u contributes to output l . For example, W_{ul} could be set to zero if there is no contribution. Alternatively, it could be set to a value indicating the tissue volume fraction that is represented by compartment u .

The contribution of the inputs to output l is calculated in an analogous fashion

$$\sum_u X_{ul} I_u \quad (64)$$

where X_{ul} is the weight that input u contributes to output l . For example, values of X_{ul} might be set to equal the tissue vascular space fraction so that the model output includes vascular radioactivity. Note, however, that there is no inclusion of the specific activity A_u in this expression. Separate inputs should be defined to account for input to compartments and for the vascular radioactivity. The values of X_{ul} corresponding to inputs to compartments are set to zero, whereas values of X_{ul} corresponding to vascular radioactivity are set to equal the vascular space fraction. This is appropriate because, most often, the inputs that serve as source for compartments are the plasma concentration of a substance, whereas for the intravascular radioactivity contribution blood concentration is required. Consequently, separate input functions are used to specify radioactivity concentration, and these should be expressed in terms of radioactivity concentration so that no multiplication by specific activity is needed.

The output equation is obtained by adding terms for the compartment and input contributions and integrating them over the scan interval, or frame, to compute the time-averaged value over the scan:

$$M_l(t_b, t_e) = \frac{1}{t_e - t_b} \int_{t_b}^{t_e} \left(\sum_u W_{ul} A_u C_u + \sum_u X_{ul} I_u \right) dt \quad (65)$$

where t_b and t_e are the beginning and ending time of the scan and M_l denotes output l .

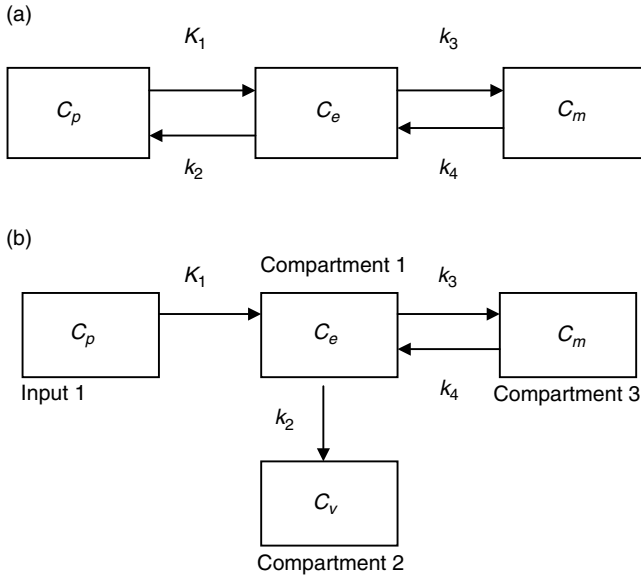


FIGURE 27 (a) Typical FDG model representation, reminiscent of Figure 6. (b) Mathematically, more precise presentation of FDG model in which the depiction is truer to the equations, which do not include a means of incrementing $C_p(t)$ based on efflux of tracer from compartment C_e .

C. Implementing an Arbitrary Model

To implement an arbitrary model within this framework is as easy as drawing compartments - as many as needed - and connecting them with arrows.

Consider for example, the fluorodeoxyglucose (FDG) metabolism model (Huang *et al.*, 1980; Phelps *et al.*, 1979) shown in its usual form in Figure 27a. As shown in this figure, normally the arrow labeled k_2 points from C_e back to the input C_p . Because an increased flux represented by this arrow does not cause C_p to increase in the model (recall that C_p is measured data), it is not correct to draw the arrow to point to C_p . Rather, this flux represents a loss of material to venous circulation, so the arrow should be drawn as a loss to a venous compartment. Thus, the model is more properly described as shown in Figure 27b. To implement this model in the framework described in the previous sections, number the compartments 1, 2, and 3, assigning the numbers as most convenient. For example, let $C_e = 1$, $C_v = 2$, and $C_m = 3$. Because the k_2 arrow is drawn from compartment 1 to compartment 2, the (1,2) element of \mathbf{K} should be set equal to the numerical value for k_2 . (The first index represents the source compartment, and the second represents the destination compartment.) Similarly, the k_3 arrow is drawn from compartment 1 to 3 so it corresponds to the (1,3) element of \mathbf{K} , whereas k_4 corresponds to the (3,1) element of \mathbf{K} . K_1 is a little different. The source is C_p , which is an input. These fluxes are represented in the \mathbf{L} matrix. Because there is only one input, it is considered input number 1 and the flux from input 1 to compartment 1 corresponds to the (1,1) element of

\mathbf{L} . For models that include saturable compartments, the bimolecular rate constants are represented in $\mathbf{K}2$ and $\mathbf{L}2$ in an analogous fashion to how the unimolecular rate constants are represented in \mathbf{K} and \mathbf{L} .

Continuing with the glucose metabolism model, the model typically has a single output, and it is calculated as $C_e + C_m$. To implement this while also accounting for temporal averaging over the scan duration, simply assign values of elements of \mathbf{W} to account for compartments 1 and 3 (C_e and C_m) contributing to output 1. Following the (source compartment, destination output) convention with \mathbf{W} as well, simply set the (1,1) and (3,1) elements to unity. Alternatively, we could calculate the output as $x C_e + y C_m$ by setting $W_{1,1} = x$ and $W_{3,1} = y$. In the case in which vascular radioactivity is to be included in the output as well, define another input, number it as input 2, corresponding to the blood (as opposed to plasma) radioactivity, and then set the (2,1) value of \mathbf{X} to equal the volume fraction attributed to vascular space.

Complex multiple-injection, receptor-saturation models (e.g., Delforge, *et al.*, 1990) may also be defined within this formulation. To do this entails defining separate inputs for each injection. For a discussion of how to describe multiple inputs mathematically for use with multiple-injection studies see Morris, Albert, *et al.*, (1996).

Acknowledgments

The authors acknowledge the gracious contributions of figures by Nat Alpert and Marc Berribee and the helpful correspondence of Hiroshi Watabe. The authors also thank Marc Normand for his proofreading assistance.

Appendix

To understand how we arrive at a convolution as a solution to Eq. (1), let us apply the method of Laplace transforms to solve it.

First, we take the transform of both sides:

$$L\left\{\frac{dC_t}{dt}\right\} = L\{K_1 C_A - k_2 C_t\}$$

In the transform domain, we have:

$$s\bar{C}_t - C_t(0) = K_1 \bar{C}_A - k_2 \bar{C}_t$$

where \bar{C}_t is the transform of C_t and $C_t(0)$ is the initial condition in the time domain.

Because the initial condition is zero, we can rearrange to solve for \bar{C}_t as follows:

$$\begin{aligned}\bar{C}_t &= \frac{K_1 C_A}{s + k_2} \\ &= K_1 C_A \frac{1}{s + k_2}\end{aligned}$$

Recall that a product in the transform domain corresponds to a convolution in the time domain. Hence,

$$C_i(t) = L^{-1}\{K_1 \bar{C}_A\} \otimes L^{-1}\{1/(s+k_2)\}$$

where L^{-1} designates the inverse transform operation. And we arrive at a solution of the form:

$$\begin{aligned} C_i(t) &= K_1 C_A \otimes e^{-k_2 t} \\ &= K_1 \int_0^t C_A(\tau) e^{-k_2(t-\tau)} d\tau \end{aligned}$$

References

- Abi-Dargham, A., Rodenhiser, J., Printz, D., Zea-Ponce, Y., Gil, R., Kegeles, L. S., Weiss, R., Cooper, T. B., Mann, J. J., Van Heertum, R. L., Gorman, J. M., and Laruelle, M. (2000). From the cover: Increased baseline occupancy of D2 receptors by dopamine in schizophrenia. *Proc. Natl. Acad. Sci. U.S.A.* **97**(14): 8104–8109.
- Albelda, S. M., Wiewrodt, R., and Zuckerman, J. B. (2000). Gene therapy for lung disease: Hype or hope? *Ann. Intern. Med.* **132**(8): 649–660.
- Alpert, N. M., Badgaiyan, R., and Fischman, A. J. (2002). Detection of neuromodulatory changes in specific systems: Experimental design and strategy. *NeuroImage* **16**(3): S53.
- Alpert, N. M., Bonab, A., and Fischman, A. J. (2000). The simplified reference region model for parametric imaging: The domain of validity. *J. Nucl. Med.* **41**(5 suppl.): 54P.
- Aston, J. A., Gunn, R. N., Worsley, K. J., Ma Y., Evans, A. C., and Dagher, A. (2000). A statistical method for the analysis of positron emission tomography neuroreceptor ligand data. *Neuroimage* **12**(3): 245–256.
- Bahn, M. M., Huang, S. C., Hawkins, R. A., Satyamurthy, N., Hoffman, J. M., Barrio, J. R., Mazziotta, J. C., and Phelps, M. E. (1989). Models for in vivo kinetic interactions of dopamine D2-neuroreceptors and 3-(2'-[18F]fluoroethyl)spiperone examined with positron emission tomography. *J. Cereb. Blood Flow Metab.* **9**: 840–849.
- Bankiewicz, K. S., Eberling, J. L., Kohutnicka, M., Jagust, W., Pivirotto, P., Bringas, J., Cunningham, J., Budinger, T. F., and Harvey-White J. (2000). Convection-enhanced delivery of AAV vector in parkinsonian monkeys: In vivo detection of gene expression and restoration of dopaminergic function using pro-drug approach. *Exp. Neurol.* **164**(1): 2–14.
- Berman, M., Grundy, S. M., and Howard, B. V. (1982). “Lipoprotein Kinetics and Modeling.” Academic Press, New York.
- Berridge, M. S., Adler, L. P., Nelson, A. D., Cassidy, E. H., Muzic, R. F., Bednarczyk, E. M., and Miraldi, F. (1991). Measurement of human cerebral blood flow with $[150]\text{I}$ butanol and positron emission tomography. *J. Cereb. Blood Flow Metab.* **11**: 707–715.
- Breier, A., Su, T-P., Saunders, R., Carson, R. E., Kolachana, B. S., de Bartolomeis, A., Weinberger, D. R., Weisenfeld, N., Malhotra, A. K., Eckelman, W. C., and Pickar, D. (1997). Schizophrenia is associated with elevated amphetamine-induced synaptic dopamine concentrations: Evidence from a novel positron emission tomography method. *Proc. Natl. Acad. Sci. U.S.A.* **94**: 2569–2574.
- Carlsson, A., and Lindqvist, M. (1963). Effect of chlorpromazine or haloperidol on formation of 3-methoxytyramine and normetanephrine in mouse brain. *Acta Pharmacol. Toxicol.* **20**: 140–144.
- Carson, E. R., Cobelli, C., and Finkelstein, L. (1983). “The Mathematical Modeling of Metabolic and Endocrine Systems”. John Wiley & Sons, New York.
- Carson, R. (1996). Mathematical modeling and compartmental analysis. In “Nuclear Medicine Diagnosis and Therapy” (J. C. Harbert, W. C. Eckelman, R. D. Neumann, eds.) Thieme Medical Publishers, New York.
- Carson, R. E., Breier, A., de Bartolomeis, A., Saunders, R. C., Su T. P., Schmall, B., Der, M. G., Pickar, D., and Eckelman, W. C. (1997). Quantification of amphetamine-induced changes in $[11\text{C}]$ -raclopride binding with continuous infusion. *J. Cereb. Blood Flow Metab.* **17**: 437–447.
- Carson, R. E., Channing, M. A., Blasberg, R. G., Dunn, B. B., Cohen, R. M., Rice, K. C., and Herscovitch, P. (1993). Comparison of bolus and infusion methods for receptor quantitation: application to $[18\text{F}]$ -cyclofoxy and positron emission tomography. *J. Cereb. Blood Flow Metab.* **13**: 24–42.
- Chase, T. N., Oh, J. D., and Blanchet, P. J. (1998). Neostratal mechanisms in Parkinson’s disease. *Neurology* **51**(suppl 2): S30–S35.
- Chen, C. H., Muzic, R. F., Jr., Nelson, A. D., and Adler, L. P. (1999). Simultaneous recovery of size and radioactivity concentration of small spheroids with PET data. *J. Nucl. Med.* **40**: 118–130.
- Christian, B. T., Narayanan, T. K., Shi, B., and Mukherjee, J. (2000). Quantitation of striatal and extrastratal D-2 dopamine receptors using PET imaging of $[18\text{F}]$ fallypride in nonhuman primates. *Synapse* **38**: 71–79.
- Cooper, J. R., Roth, R., and Bloom, F. E. (1996). “The Biochemical Basis of Neuropharmacology,” 7th ed. Oxford University Press, New York.
- Crone, C. (1964). Permeability of capillaries in various organs as determined by use of the indicator diffusion method. *Acta Physiol. Scand.* **58**: 292–305.
- Cunningham, V. J., Ashburner, J., Byrne, H., and Jones, T. (1993). Use of spectral analysis to obtain parametric images from dynamic PET studies. In “Quantification of Brain Function: Tracer Kinetics and Image Analysis in Brain PET” (K. Uemura, N. A. Lassen, T. Jones, and I. Kanno, eds.), pp. 101–108. Elsevier Science Publishers, Amsterdam.
- Cunningham, V. J., Hume, S. P., Price, G. R., Ahier, R. G., Cremer, J. E., and Jones, A. K. P. (1991). Compartmental analysis of diprenorphine binding to opiate receptors in the rat *in vivo* and its comparison with equilibrium data *in vitro*. *J. Cereb. Blood Flow Metab.* **11**: 1–9.
- Cunningham, V. J., and Jones, T. (1993). Spectral analysis of dynamic PET studies. *J. Cereb. Blood Flow Metab.* **13**: 15–23.
- Delforge, J., Bottlaender, M., Pappata, S., Loch, C., and Syrota, A. (2001). Absolute quantification by positron emission tomography of the endogenous ligand. *J. Cereb. Blood Flow Metab.* **21**(5): 613–630.
- Delforge, J., Syrota, A., and Bendriem, B. (1996). Concept of reaction volume in the *in vivo* ligand-receptor model. *J. Nucl. Med.* **37**: 118–125.
- Delforge, J., Syrota, A., and Mazoyer, B. M. (1989). Experimental design optimisation: Theory and application to estimation of receptor model parameters using dynamic positron emission tomography. *Phys. Med. Biol.* **34**: 419–435.
- Delforge, J., Syrota, A., and Mazoyer, B. M. (1990). Identifiability analysis and parameter identification of an *in vivo* ligand-receptor model from PET data. *IEEE Trans. Biomed. Eng.* **37**: 653–661.
- Dienel, G. A., Cruz, N. F., Mori, K., Holden, J., and Sokoloff, L. (1991). Direct measurement of the λ of the lumped constant of the deoxyglucose method in rat brain: Determination of λ and lumped constant from tissue glucose concentration or equilibrium tissue:plasma distribution ratio for methylglucose. *J. Cereb. Blood Flow Metab.* **11**: 25–34.
- Dienel, G. A., Nakanishi, H., Cruz, N. F., and Sokoloff, L. (1991). Determination of local brain glucose concentration from the brain:plasma methylglucose distribution ratio: Influence of glucose utilization rate. *J. Cereb. Blood Flow Metab.* **11**(suppl 2): S581.
- Endres, C. J., and Carson, R. E. (1998). Assessment of dynamic neurotransmitter changes with bolus or infusion delivery of neuroreceptor ligands. *J. Cereb. Blood Flow Metab.* **18**: 1196–1210.
- Endres, C. J., Kolachana, B. S., Saunders, R. C., Su, T., Weinberger, D., Breier, A., Eckelman, W. C., and Carson, R. E. (1997). Kinetic modeling fo $[11\text{C}]$ raclopride: Combined PET-microdialysis studies. *J. Cereb. Blood Flow Metab.* **17**: 932–942.

- Farde, L., Eriksson, L., Blomquist, G., and Halldin, C. (1989). Kinetic analysis of central [11C]raclopride binding to D2-dopamine receptors studied by PET: A comparison to the equilibrium analysis. *J. Cereb. Blood Flow Metab.* **9:** 696–708.
- Farde, L., Wiesel, F. A., Stone-Elander, S., Halldin, C., Nordstrom, A. L., Hall, H., and Sedvall, G. (1990). D2 dopamine receptors in neuroleptic-naïve schizophrenic patients: A positron emission tomography study with [11C]raclopride. *Arch. Gen. Psychiatry* **47**(3): 213–219.
- Feng, D., Li, X., and Huang, S. C. (1996). A new double modeling approach for dynamic cardiac PET studies using noise and spillover contaminated LV measurements. *IEEE Trans. Biomed. Eng.* **43:** 319–327.
- Fisher, R. E., Morris, E. D., Alpert, N. M., and Fischman, A. J. (1995). In vivo imaging of neuromodulatory synaptic transmission using PET: A review of the relevant neurophysiology. *Hum. Br. Map.* **3:** 24–34.
- Frey, K. A., Hichwa, R. D., Ehrenkaufer, R. L. E., and Agranoff, B. W. (1985). Quantitative *in vivo* receptor binding, III. Tracer kinetic modeling of muscarinic cholinergic receptor binding. *Proc. Natl. Acad. Sci. U.S.A.* **82:** 6711–6715.
- Friston, K. J., Malizia, A. L., Wilson, S., Cunningham, V. J., Jones, T., and Nutt, D. J. (1997). Analysis of dynamic radioligand displacement or “activation” studies. *J. Cereb. Blood Flow Metab.* **17:** 80–93.
- Frost, J. J., Douglass, K. H., Mayber, H. S., Dannals, R. F., Links, J. M., Wilson, A. A., Ravert, H. T., Crozier, W. C., and Wagner, H. N., Jr. (1989). Multicompartmental analysis of [11C]-carfentanil binding to opiate receptors in humans measured by positron emission tomography. *J. Cereb. Blood Flow Metab.* **9:** 398–409.
- Gjedde, A., Wienhard, K., Heiss, W.-D., Kloster, G., Diemer, N. H., Herholz, K., and Pawlik, G. (1985). Comparative regional analysis of 2-fluorodeoxyglucose and methylglucose uptake in brain of four stroke patients. With special reference to the regional estimation of the lumped constant. *J. Cereb. Blood Flow Metab.* **5:** 163–178.
- Gunn, R. N., Lammertsma, A. A., Hume, S. P., and Cunningham, V. J. (1997). Parametric imaging of ligand-receptor binding in PET using a simplified reference region model. *Neuroimage* **6:** 279–287.
- Hearon, J. Z. (1963). Theorems on linear systems. *Ann. N.Y. Acad. Sci.* **108:** 36–68.
- Herrero, P., Markham, J., and Bergmann, S. R. (1989). Quantitation of myocardial blood flow with H₂ 15O and positron emission tomography: Assessment and error analysis of a mathematical approach. *J. Comput. Assist. Tomogr.* **13:** 862–873.
- Herscovitch, P., Markham, J., and Raichle, M. E. (1983). Brain blood flow measured with intravenous H₂¹⁵O, I. Theory and error analysis. *J. Nucl. Med.* **24:** 782–789.
- Hoekstra, C. J., Paglianiti, I., Hoekstra, O. S., Smit, E. F., Postmus, P. E., Teule, G. J., and Lammertsma, A. A. (1999). Monitoring response to therapy in cancer using [¹⁸F]-2-fluoro-2-deoxyglucose and positron emission tomography: An overview of different analytical methods. *Eur. J. Nucl. Med.* **27**(6): 731–743.
- Hoffman, E. J., Huang, S. C., and Phelps, M. E. (1979). Quantitation in positron emission computed tomography, 1. Effect of object size. *J. Comput. Assist. Tomogr.* **3:** 299–308.
- Hsu, H., Alpert, N. M., Christian, B. T., Bonab, A. A., Morris, E., and Fischman, A. J. (1997). Noise properties of a graphical assay of receptor binding. *J. Nucl. Med.* **38:** 204P.
- Huang, S. C., Bahn, M. M., Barrio, J. R., Hoffman, J. M., Satyamurthy, N., Hawkins, R. A., Mazziotta, J. C., and Phelps, M. E. (1989). A double-injection technique for the *in vivo* measurement of dopamine D2-receptor density in monkeys with 3-(2'-[18F]fluoroethyl)spiperone and dynamic positron emission tomography. *J. Cereb. Blood Flow Metab.* **9:** 850–858.
- Huang, S. C., Carson, R. E., Hoffman, E. J., Carson, J., MacDonald, N., Barrio, J. R., and Phelps, M. E. (1983). Quantitative measurement of local cerebral blood flow in humans by positron computed tomography and ¹⁵O-water. *J. Cereb. Blood Flow Metab.* **3:** 141–153.
- Huang, S. C., Dan-chu, Y., Barrio, J. R., Grafton, S., Melega, W. P., Hoffman, J. M., Satyamurthy, N., Mazziotta, J. C., and Phelps, M. E. (1991). Kinetics and modeling of L-6-[18F]Fluoro-DOPA in human positron emission tomographic studies. *J. Cereb. Blood Flow Metab.* **11:** 898–913.
- Huang, S. C., Mahoney, D. K., and Phelps, M. E. (1986). Quantitation in positron emission tomography, 8. Effects of nonlinear parameter estimation on functional images. *J. Cereb. Blood Flow Metab.* **6:** 515–521.
- Huang, S. C., and Phelps, M. E. (1986). Principles of tracer kinetic modeling in positron emission tomography and autoradiography. In “Positron Emission Tomography and Autoradiography: Principles and Applications for the Brain and Heart”. (M.E. Phelps, J. Mazziotta, and H. Schelbert, eds.) pp. 287–346. Raven Press, New York.
- Huang, S. C., Phelps, M. E., Hoffman, E. J., Sideris, K., Selin, C. J., and Kuhl, D. E. (1980). Noninvasive determination of local cerebral metabolic rate of glucose in man. *Am. J. Physiol.* **238:** E69–E82.
- Hume, S. P., Myers, R., Bloomfield, P. M., Opacka-Juffry, J., Cremer J. E., Ahier, R. G., Luthra, S. K., Brooks, D. J., and Lammertsma, A. A. (1992). Quantitation of carbon-11 labeled raclopride in rat striatum using positron emission tomography. *Synapse* **12:** 47–54.
- Hustinx, R., Eck, S. L., and Alavi, A. J. (1999). Potential applications of PET imaging in developing novel cancer therapies. *J. Nucl. Med.* **40:** 995–1002.
- Hustinx, R., Eck, S. L., and Alavi, A. J. (1999). Potential applications of PET imaging in developing novel cancer therapies. *J. Nucl. Med.* **40**(6): 995–1002.
- Ichise, M., Ballinger, J. R., Golani, H., Vines, D., Luong, A., Tsai, S., and Kung, H. F. (1996). Noninvasive quantification of dopamine D2 receptors with iodine-123-IBF SPECT. *J. Nucl. Med.* **37**(3): 513–20.
- Ichise, M., Meyer, J. H., and Yonekura, Y. (2001). An introduction to PET and SPECT neuroreceptor quantification models. *J. Nucl. Med.* **42**(5): 755–763.
- Iida, H., Kanno, I., Miura, S., Murakami, M., Takahashi, K., and Uemura, K. (1986). Error analysis of a quantitative cerebral blood flow measurement using H₂¹⁵O autoradiography and positron emission tomography. *J. Cereb. Blood Flow Metab.* **6:** 536–545.
- Iida, H., Kanno, I., Miura, S., Murakami, M., Takahashi, K., and Uemura, K. (1989). A determination of the regional brain/blood partition coefficient of water using dynamic positron emission tomography. *J. Cereb. Blood Flow Metab.* **9:** 874–885.
- Iida, H., Law, I., Pakkenberg, B., Krarup-Hansen, A., Eberl, S., Holm, S., Hansen, A. K., Gunderson, H. J. G., Thomsen, C., Svarer, C., Ring, P., Friberg, L., and Paulson, O. B. (2000). Quantitation of regional cerebral blood flow corrected for partial volume effect using O-15 water and PET, I. Theory, error analysis, and stereological comparison. *J. Cereb. Blood Flow Metab.* **20:** 1237–1251.
- Inoue, O., Kobayashi, K., and Gee, A. (1999). Changes in apparent rates of receptor binding in the intact brain in relation to the heterogeneity of reaction environments. *Crit. Rev. Neurobiol.* **13**(2): 199–225.
- Jacquez, J. A. (1985). “Compartmental Analysis in Biology and Medicine,” 2nd ed. University of Michigan Press, Ann Arbor.
- Kaplan, H. I., and Sadock, B. J. (1998). “Synopsis of Psychiatry,” 8th ed. Lippincott Williams and Wilkins, Baltimore.
- Kawai, R., Carson, R. E., Dunn, B., Newman, A. H., Rice, K. C., and Blasberg, R. G. (1991). Regional brain measurement of Bmax and KD with the opiate antagonist cyclofoxy: Equilibrium studies in the conscious rat. *J. Cereb. Blood Flow Metab.* **11**(4): 529–544.
- Koeppe, M. J., Gunn, R. N., Lawrence, A. D., Cunningham, V. J., Dagher, A., Jones, T., Brooks, D. J., Bench, C. J., and Grasby, P. M. (1998). Evidence for striatal dopamine release during a video game. *Nature* **393:** 266–268.
- Koeppe, R. A., Frey, K. A., Mulholland, G. K., Kilbourn, M. R., Buck, A., Lee, K. S., and Kuhl, D. E. (1994). [11C]tropomy benzilate-binding to muscarinic cholinergic receptors: Methodology and kinetic modeling alternatives. *J. Cereb. Blood Flow Metab.* **14:** 85–99.
- Koeppe, R. A., Holden, J. E., and Ip, W. R. (1985). Performance comparison of parameter estimation techniques for the quantitation of

- local cerebral blood flow by dynamic positron computed tomography. *J. Cereb. Blood Flow Metab.* **5**: 224–234.
- Koeppe, R. A., Holthoff, V. A., Frey, K. A., Kilbourn, M. R., and Kuhl, D. E. (1991). Compartmental analysis of [¹¹C]flumazenil kinetics for the estimation of ligand transport rate and receptor distribution using positron emission tomography. *J. Cereb. Blood. Flow Metab.* **11**: 735–744.
- Kuwabara, H., Evans, A. C., and Gjedde, A. (1990). Michaelis-Menten constraints improved cerebral glucose metabolism and regional lumped constant measurements with [¹⁸F]fluorodeoxyglucose. *J. Cereb. Blood Flow Metab.* **10**: 180–189.
- Lammertsma, A. A., Bench, C. J., Hume, S. P., Osman, S., Gunn, K., Brooks, D. J., and Frackowiak, R. J. (1996). Comparison of methods for analysis of clinical [¹¹C]raclopride studies. *J. Cereb. Blood Flow Metab.* **16**: 42–52.
- Larisch, R., Schommartz, B., Vosberg, H., and Muller-Gartner, H. W. (1999). Influence of motor activity on striatal dopamine release: A study using iodobenzamide and SPECT. *Neuroimage* **10**: 261–268.
- Laruelle, M. (2000). Imaging synaptic neurotransmission with *in vivo* binding competition techniques: A critical review. *J. Cereb. Blood Flow Metab.* **20**(3): 423–451.
- Laruelle, M., Abi-Dargham, A., van Dyck, C. H., Gil, R., D'Souza, C. D., Erdos, J., McCance, E., Rosenblatt, W., Fingado, C., Zoghbi, S. S., Baldwin, R. M., Seibyl, J. P., Krystal, J. H., Charney, D. S., and Innis, R. B. (1996). Single photon emission computerized tomography imaging of amphetamine-induced dopamine release in drug-free schizophrenic subjects. *Proc. Natl. Acad. Sci. U.S.A.* **93**(17): 9235–9240.
- Laruelle, M., Iyer, R. N., Al-Tikriti, M. S., Zea-Ponce, Y., Malison, R., Zoghbi, S. S., Baldwin, R. M., Kung, H. F., Charney, D. S., Hoffer, P. B., Innis, R. B., and Bradberry, C. W. (1997). Microdialysis and SPECT measurements of amphetamine-induced release in nonhuman primates. *Synapse* **25**: 1–14.
- Laruelle, M., Wallace, E., Seibyl, P., Baldwin, R. M., Zea-Ponce, Y., Zoghbi, S. S., Neumeyer, J. L., Charney, D. S., Hoffer, P. B., and Innis, R. B. (1994). Graphical, kinetic, and equilibrium analyses of *in vivo* [¹²³I] β -CIT binding to dopamine transporters in healthy human subjects. *J. Cereb. Blood Flow Metab.* **14**: 982–994.
- Law, I., Iida, H., Holm, S., Nour, S., Rostrup, E., Svarer, C., and Paulson, O. B. (2000). Quantitation of regional cerebral blood flow corrected for partial volume effect using O-15 water and PET, II. Normal values and gray matter blood flow response to visual activation. *J. Cereb. Blood Flow Metab.* **20**: 1252–1263.
- Logan, J. (2000). Graphical analysis of PET data applied to reversible and irreversible tracers. *Nucl. Med. Biol.* **27**: 661–670.
- Logan, J., Dewey, S. L., Wolf, A. P., Fowler, J. S., Brodie, J. D., Angrist, B., Volkow, N. D., and Gatley, S. J. (1991). Effects of endogenous dopamine on measures of [¹⁸F]-methylspiroperidol binding in the basal ganglia: Comparison of simulations and experimental results from PET studies in baboons. *Synapse* **9**: 195–207.
- Logan, J., Fowler, J. S., Volkow, N. D., Ding, Y. S., Wang, G. J., and Alexoff, D. L. (2001). A strategy for removing the bias in the graphical analysis method. *J. Cereb. Blood Flow Metab.* **21**(3): 307–320.
- Logan, J., Fowler, J. S., Volkow, N. D., Wang, G. J., Dewey, S. L., MacGregor, R. R., Schlyer, D. J., Gatley, S. J., Pappas, N., King, P., Hitzemann, R., and Vitkun, S. (1994). Effects of blood flow on [¹¹C]-raclopride binding in the brain: model simulations and kinetic analysis of PET data. *J. Cereb. Blood Flow Metab.* **14**: 995–1010.
- Logan, J., Fowler, J. S., Volkow, N. D., Wang, G. J., Ding, Y. S., and Alexoff, D. L. (1996). Distribution volume ratios without blood sampling from graphical analysis of PET data. *J. Cereb. Blood Flow Metab.* **16**: 834–840.
- Logan, J., Fowler, J. S., Volkow, N. D., Wolf, A. P., Dewey, S. L., Schlyer, D. J., MacGregor, R. R., Hitzemann, R., Bendriem, B., Gatley, S. J., and Christman, D. R. (1990). Graphical analysis of reversible radioligand binding from time-activity measurements applied to [¹¹C-methyl]-(-)-cocaine PET studies in human subjects. *J. Cereb. Blood Flow Metab.* **10**: 740–747.
- Lucignani, G., Schmidt, K., Moresco, R. M., Stirano, G., Colombo F., Sokoloff, L., and Fazio, F. (1993). Measurement of regional cerebral glucose utilization with [¹⁸F]FDG and PET in heterogeneous tissues: theoretical considerations and practical procedure. *J. Nucl. Med.* **34**: 360–369.
- MacLaren, D. C., Gambhir, S. S., Satyamurthy, N., Barrio, J. R., Sharfstein, S., Toyokuni, T., Wu, L., Berk, A. J., Cherry, S. R., Phelps, M. E., and Herschman, H. R. (1999). Repetitive, non-invasive imaging of the dopamine D₂ receptor as a reporter gene in living animals. *Gene Ther.* **6**(5): 785–791.
- MacLaren, D. C., Toyokuni, T., Cherry, S. R., Barrio, J. R., Phelps, M. E., Herschman, H. R., and Gambhir, S. S. (2000). PET imaging of transgene expression. *Biol. Psych.* **48**: 337–348.
- Martin, C. C., Jerabek, P. A., Nickerson, L. D. H., and Fox, P. T. (1999). Effect of partition coefficient, permeability surface product, and radioisotope on the signal-to-noise ratio in PET functional brain mapping: A computer simulation. *Hum. Br. Map.* **7**(3): 151–160.
- Meltzer, C. C., Leal, J. P., Mayberg, H. S., Wagner, H. N., and Frost, J. J. (1990). Correction of PET data for partial volume effects in human cerebral cortex by MR imaging. *J. Comput. Assist. Tomogr.* **14**: 561–570.
- Meltzer, C. C., Zubietka, J. K., Links, J. M., Brakeman, P., Stumpf, M. J., and Frost, J. J. (1996). MR-based correction of brain PET measurements for heterogeneous gray matter radioactivity distribution. *J. Cereb. Blood Flow Metab.* **16**: 650–658.
- Meyer, E. (1989). Simultaneous correction for tracer arrival delay and dispersion in CBF measurements by the H₂O₁₅ autoradiographic method and dynamic PET. *J. Nucl. Med.* **30**: 1069–1078.
- Mintun, M. A., Raichle, M. E., Kilbourn, M. R., Wooten, G. F., and Welch, M. J. (1984). A quantitative model for the *in vivo* assessment of drug binding sites with positron emission tomography. *Ann. Neurol.* **15**: 217–227.
- Morris, E. D., Alpert, N. M., and Fischman, A. J. (1996). Comparison of two compartmental models for describing receptor ligand kinetics and receptor availability in multiple injection PET studies. *J. Cereb. Blood Flow Metab.* **16**: 841–853.
- Morris, E. D., Babich, J. W., Alpert, N. M., Bonab, A. A., Livni, E., Weise, S., Hsu, H., Christian, B. T., Madras, B. K., and Fischman, A. J. (1996). Quantification of dopamine transporter density in monkeys by dynamic PET imaging of multiple injections of [¹¹C]-CFT. *Synapse* **24**: 262–272.
- Morris, E. D., Bonab, A. A., Alpert, N. M., Fischman, A. J., Madras, B. K., and Christian, B. T. (1999). Concentration of dopamine transporters: To Bmax or not to Bmax? *Synapse* **32**(2): 136–140.
- Morris, E. D., Chefer, S. I., Lane, M. A., Muzic, R. F., Jr., Wong, D. F., Dannals, R. F., Matochik, J. A., Bonab, A. A., Villemagne, V. L., Ingram, D. K., Roth, G. S., and London, E. D. (1999). Decline of D₂ receptor binding with age, in rhesus monkeys: Importance of correction for simultaneous decline in striatal size. *J. Cereb. Blood Flow Metab.* **19**: 218–229.
- Morris, E. D., Fisher, R. E., Alpert, N. M., Rauch, S. L., and Fischman, A. J. (1995). In vivo imaging of neuromodulation using positron emission tomography: Optimal ligand characteristics and task length for detection of activation. *Hum. Br. Map.* **3**: 35–55.
- Muller-Gartner, H. W., Links, J. M., Prince, J. L., Bryan, R. N., McVeigh, E., Leal, J. P., Davatzikos, C., and Frost, J. J. (1992). Measurement of radiotracer concentration in brain gray matter using positron emission tomography: MRI-based correction for partial volume effects. *J. Cereb. Blood Flow Metab.* **12**: 571–583.
- Muzic, R. F., Jr., Chen, C. H., and Nelson, A. D. (1998). Method to account for scatter, spillover and partial volume effects in region of interest analysis in PET. *IEEE Trans. Med. Imag.* **17**: 202–213.

- Muzic, R. F., Jr., and Cornelius, S. (2001). COMKAT: Compartment model kinetic analysis tool. *J. Nucl. Med.* **42**: 636–645.
- Muzic, R. F., Jr., Nelson, A. D., and Miraldi, F. (1990). Mathematical simplification of a PET blood flow model. *IEEE Trans. Med. Imag.* **9**: 172–176.
- Muzic, R. F., Jr., Nelson, A. D., and Miraldi, F. (1993). Temporal alignment of tissue and arterial data and selection of integration start times for the $H_2^{15}O$ autoradiographic CBF model in PET. *IEEE Trans. Med. Imag.* **12**: 393–398.
- Nelson, A. D., Muzic, R. F., Jr., Miraldi, F., Muswick, G. J., Leisure, G. P., and Voelker, W. (1990). Continuous arterial positron monitor for quantitation in PET imaging. *Am. J. Physiol. Imag.* **5**: 84–88.
- Nicoll, R. A., and Malenka, R. C. (1999). Expression mechanisms underlying NMDA receptor-dependent long-term potentiation. *Ann. N.Y. Acad. Sci.* **30**(868): 515–525.
- Ohta, S., Meyer, E., Fujita, H., Reutens, D. C., Evans, A., and Gjedde, A. (1996). Cerebral [^{15}O]water clearance in humans determined by PET, I. Theory and normal values. *J. Cereb. Blood Flow Metab.* **16**: 765–780.
- Pajevic, S., Daube-Witherspoon, M. E., Bacharach, S. L., and Carson, R. E. (1998). Noise characteristics of 3-D and 2-D PET images. *IEEE Trans. Med. Imag.* **17**: 9–23.
- Pappata, J., Dehaene, S., Poline, J. B., Gregoire, M. C., Jobert, A., Delforge, J., Frouin, V., Bottlaender, M., Dolle, F., Di Giamberardino, L., and Syrota, A. (2002). In vivo detection of striatal dopamine release during reward: A PET study with [^{11}C]Raclopride and a single dynamic scan approach. *NeuroImage* **16**: 1015–1027.
- Patlak, C., and Blasberg, R. (1985). Graphical evaluation of blood-to-brain transfer constants from multiple-time uptake data: Generalizations. *J. Cereb. Blood Flow Metab.* **5**: 584–590.
- Patlak, C., Blasberg, R., and Fenstermacher, J. (1983). Graphical evaluation of blood-to-brain transfer constants from multiple-time uptake data. *J. Cereb. Blood Flow Metab.* **3**: 1–7.
- Phelps, M. E., Huang, S. C., Hoffman, E. J., Selin, C. J., Sokoloff, L., and Kuhl, D. E. (1979). Tomographic measurement of local cerebral glucose metabolic rate in humans with [^{18}F]2-fluoro-2-deoxy-D-glucose: Validation of method. *Ann. Neurol.* **6**: 371–388.
- Raichle, M. E., Martin, W. R. W., Herscovitch, P., Mintun, M. A., and Markham, J. (1983). Brain blood flow measured with intravenous H_2O^{15} , II. Implementation and validation. *J. Nucl. Med.* **24**: 790–798.
- Reivich, M., Alavi, A., Wolf, A., Fowler, J., Russell, J., Arnett, C., MacGregor, R. R., Shiue, C. Y., Atkins, H., Anand, A., Dann, R., and Greenberg, J. H. (1985). Glucose metabolic rate kinetic model parameter determination in humans: The lumped constants and rate constants for [^{18}F]fluorodeoxyglucose and [^{11}C]deoxyglucose. *J. Cereb. Blood Flow Metab.* **5**: 179–192.
- Reivich, M., Kuhl, D., Wolf, A., Greenberg, J., Phelps, M., Ido, T., Casella, V., Fowler, J., Hoffman, E., Alavi, A., Som, P., and Sokoloff, L. (1979). The [^{18}F]fluorodeoxyglucose method for the measurement of local cerebral glucose utilization in man. *Circ. Res.* **44**: 127–137.
- Renkin, E. M. (1959). Transport of potassium-42 from blood to tissue in isolated mammalian skeletal muscles. *Am. J. Physiol.* **197**: 1205–1210.
- Rousset, O. G., Ma, Y., and Evans, A. C. (1998). Correction for partial volume effects in PET: Principle and validation. *J. Nucl. Med.* **39**: 904–911.
- Schmidt, K. (1999). Which linear compartmental systems can be analyzed by spectral analysis of PET output data summed over all compartments? *J. Cereb. Blood Flow Metab.* **19**: 560–569.
- Schmidt, K., Lucignani, G., Moresco, R. M., Rizzo, G., Gilardi, M. C., Messa, C., Colombo, F., Fazio, F., and Sokoloff, L. (1992). Errors introduced by tissue heterogeneity in estimation of local cerebral glucose utilization with current kinetic models of the [^{18}F]fluorodeoxyglucose method. *J. Cereb. Blood Flow Metab.* **12**: 823–834.
- Schmidt, K., Mies, G., and Sokoloff, L. (1991). Model of kinetic behavior of deoxyglucose in heterogeneous tissues in brain: a reinterpretation of the significance of parameters fitted to homogeneous tissue models. *J. Cereb. Blood Flow Metab.* **11**: 10–24.
- Schmidt, K., and Sokoloff, L. (2001). A computationally efficient algorithm for determining regional cerebral blood flow in heterogeneous tissues by positron emission tomography, *IEEE Trans. Med. Imag.* **20**(7): 618–632.
- Schmidt, K., Sokoloff, L., and Kety, S. S. (1989). Effects of tissue heterogeneity on estimates of regional cerebral blood flow. *J. Cereb. Blood Flow Metab.* **9**(suppl. 1): S242.
- Schommartz, B., Larisch, R., Vosberg, H., and Muller-Gartner, H. W. (2000). Striatal dopamine release in reading and writing measured with [^{123}I]iodobenzamide and single photon emission computed tomography in right handed human subjects. *Neurosci. Lett.* **292**(1): 37–40.
- Schuier, F., Orzi, F., Suda, S., Lucignani, G., Kennedy, C., and Sokoloff, L. (1990). Influence of plasma glucose concentration on lumped constant of the deoxyglucose method: Effects of hyperglycemia in the rat. *J. Cereb. Blood Flow Metab.* **10**: 765–773.
- Schultz, W. (1997). Dopamine neurons and their role in reward mechanisms. *Curr. Opin. Neurobiol.* **7**: 191–197.
- Shepherd, G. M. (1998). "The Synaptic Organization of the Brain," 4th ed. Oxford University Press, New York.
- Slifstein, M., and Laruelle, M. (2000). Effects of statistical noise on graphic analysis of PET neuroreceptor studies. *J. Nucl. Med.* **41**(12): 2083–2088.
- Soares, J. C., and Innis, R. B. (1999). Neurochemical brain imaging investigations of schizophrenia. *Biol. Psych.* **46**: 600–615.
- Sokoloff, L. (1977). Relation between physiological function and energy metabolism in the central nervous system. *J. Neurochem.* **29**: 13–26.
- Sokoloff, L., Reivich, M., Kennedy, C., DesRosier, M. H., Patlak, C. S., Pettigrew, K. D., Sakurada, O., and Shinohara, M. (1977). The [^{14}C]deoxyglucose method for the measurement of local cerebral glucose utilization: theory, procedure, and normal values in the conscious and anesthetized albino rat. *J. Neurochem.* **28**: 897–916.
- Sorenson, J. A., and Phelps, M. E. (1987). "Physics in Nuclear Medicine," 2nd ed. Grune and Stratton, Orlando, FL.
- Squire, L. R., and Kandel, E. R. (1999). "Memory: From Mind to Molecules." Scientific American Library, New York.
- Strul, D., and Bendriem, B. (1999). Robustness of anatomically guided pixel-by-pixel algorithms for partial volume effect correction in positron emission tomography. *J. Cereb. Blood Flow Metab.* **19**: 547–559.
- Suda, S., Shinohara, M., Miyaoka, M., Lucignani, G., Kennedy, C., and Sokoloff, L. (1990). The lumped constant of the deoxyglucose method in hypoglycemia: Effects of moderate hypoglycemia on local cerebral glucose utilization in the rat. *J. Cereb. Blood Flow Metab.* **10**: 499–509.
- Tjuvajev, J. G., Avril, N., Oku, T., Sasajima, T., Miyagawa, T., Joshi, R., Safer, M., Beattie, B., DiResta, G., Daghlian, F., Augensen, F., Koutcher, J., Zweit, J., Humm, J., Larson, S. M., Finn, R., and Blasberg, R. (1998). Imaging herpes virus thymidine kinase gene transfer and expression by positron emission tomography. *Cancer Res.* **58**: 4333–4341.
- Tsukada, H., Nishiyama, S., Kakiuchi, T., Ohba, H., Sato, K., and Harada, N. (1999). Is synaptic dopamine concentration the exclusive factor which alters the in vivo binding of [^{11}C]raclopride? PET studies combined with microdialysis in conscious monkeys. *Br. Res.* **841**(1–2): 160–169.
- Turkheimer, F., Moresco, R. M., Lucignani, G., Sokoloff, L., Fazio, F., and Schmidt, K. (1994). The use of spectral analysis to determine regional cerebral glucose utilization with positron emission tomography and [^{18}F]Fluorodeoxyglucose: Theory, implementation and optimization procedures. *J. Cereb. Blood Flow Metab.* **14**: 406–422.
- Turkheimer, F., Sokoloff, L., Bertoldo, A., Lucignani, G., Reivich, M., Jaggi, J. L., and Schmidt, K. (1998). Estimation of component and parameter distributions in spectral analysis. *J. Cereb. Blood Flow Metab.* **18**: 1211–1222.

- Videen, T. O., Perlmuter, J. S., Mintun, M. A., and Raichle, M. E. (1988). Regional correction of positron emission tomography data for the effects of cerebral atrophy. *J. Cereb. Blood Flow Metab.* **8**: 662–670.
- Watabe, H., Endres, C. J., Breier, A., Schmall, B., Eckelman, W. C., and Carson, R. E. (2000). Measurement of dopamine release with continuous infusion of [¹¹C]raclopride: optimization and signal-to-noise consideration. *J. Nucl. Med.* **41**(3): 522–530.
- Watabe, H., Itoh, M., Cunningham, V., Lammertsma, A. A., Bloomfield, P., Mejia, M., Fujiwara, T., Jones, A. K., Jones, T., and Nakamura, T. (1996). Noninvasive quantification of rCBF using positron emission tomography. *J. Cereb. Blood Flow Metab.* **16**(2): 311–319.
- Wong, D. F., Wagner, H. N. J., Tune, L. E., Dannals, R. F., Pearson, G. D., Links, J. M., Tamminga, C. A., Broussolle, E. P., Ravert, H. T., Wilson, A. A., et al. (1986). Positron emission tomography reveals elevated D₂ dopamine receptors in drug-naïve schizophrenics. *Science* **234**: 1558–1563.
- Yu, Y., Annala, A. J., Barrio, J. R., Toyokuni, T., Satyamurthy, N., Namavari, M., Cherry, S. R., Phelps, M. E., Herschman, H. R., and Gambhir, S. S. (2000). Quantification of target gene expression by imaging reporter gene expression in living animals. *Nature Med.* **6**: 933–937.
- Zhou, Q., Xiao, M. Y., and Nicoll, R. A. (2001). Contribution of cytoskeleton to the internalization of AMPA receptors. *Proc. Natl. Acad. Sci. U.S.A.* **98**(3): 1261–1266.
- Zubieta, J.-K., Koeppe, R. A., Mulholland, G. K., Kuhl, D. E., and Frey, K. A. (1998). Quantification of muscarinic cholinergic receptors with [¹¹C]NMPB and positron emission tomography: Method development and differentiation of tracer delivery from receptor binding. *J. Cereb. Blood Flow Metab.* **18**: 619–631.